Quantifying the deep: The importance of diagenetic reactions to marine geochemical cycles

Richard David Berg

A dissertation

submitted in partial fulfillment of the

requirements for the degree of

Doctor of Philosophy

University of Washington

2018

Reading Committee:

Evan A. Solomon, Chair

Curtis A. Deutsch

Richard G. Keil

Program Authorized to Offer Degree:

School of Oceanography

University of Washington

Abstract

Quantifying the deep: The importance of diagenetic reactions to marine geochemical cycles

Richard David Berg

Chair of the Supervisory Committee:
Professor Evan A. Solomon
Oceanography

Marine sediments play a fundamental role in long-term element cycles on Earth and host an expansive microbial ecosystem known as the “oceanic deep biosphere”. The biogeochemical and inorganic reactions that occur in the sediments as they are buried alter both their physical and chemical properties, as well as control the chemistry of the surrounding pore waters. While the alteration of sediments can affect subduction zone dynamics and mantle geochemistry, chemical alteration of pore waters affects ocean chemistry through the diffusional and advective communication between pore waters and the overlying ocean. The alteration of pore waters also provides a sensitive indicator of the chemical reactions taking place in marine sediments. However, the same mobility of solutes in pore water that results in marine sediments’ influence on ocean chemistry also results in challenges in quantifying and characterizing these reactions. Reactive-transport modeling is an effective approach employed to characterize the reactions

taking place in marine sediments that accounts for the mobility of solutes and pore waters. Data collected and archived during the past ~50 years of scientific ocean drilling provides the necessary information to parameterize and apply reactive-transport modeling to study marine sedimentary reactions on local, regional, and global scales. The research detailed in this dissertation utilizes reactive-transport modeling of ocean drilling data, supplemented with new measurements, to evaluate the influence of dehalogenation reactions on the deep biosphere, and the role of authigenic mineral formation reactions in global geochemical cycles.

Reactive-transport modeling is complementary to measurements that characterize microbial communities in the deep biosphere. Genomics, metagenomics, metabolomics, and other methods provide information about the composition and function of microbes in marine sediments, but geochemically-derived reaction rates are needed to understand the magnitudes of the *in situ* activity in these communities. The research described in Chapter 2 supplements reactive-transport modeling of pore water bromide with new measurements of solid-phase organobromine content to constrain the maximum rates of microbial organobromine respiration and to investigate the depth distribution of debromination activity in continental margin sediments. The reactive-transport modeling results and organobromine profiles indicate that debromination is most active in the upper sediment column, and is largely limited by substrate availability. Maximum depth-integrated rates of debromination on the order of 10^1 to 10^3 μmol m^{-2} y^{-1} indicate that the amount of energy that is provided through organobromine respiration is low relative to other metabolic pathways such as sulfate reduction and methanogenesis, but may still serve an important niche in the microbial community. In addition, a close connection between debromination and ammonium production is apparent in the pore water profiles, suggesting a relationship between debromination and degradation of the amino acid fraction of

organic matter, which may allow debromination to be a useful tracer for degradation of this labile pool of carbon and nitrogen.

Ocean drilling data supplemented with new measurements are also effective for investigating oceanic geochemical cycles on a global scale, such as the oceanic magnesium cycle. The oceanic magnesium cycle is intimately connected to long-term climate on Earth through its relationship to continental weathering and formation of aluminosilicate and carbonate minerals. Uncertainties in the oceanic magnesium cycle propagate into other chemical budgets such as carbon and calcium, and into interpretations of paleo-oceanographic reconstructions of seawater δ^{26}Mg and Mg/Ca ratios. In Chapter 3, dissolved magnesium fluxes at 269 ocean drilling sites are calculated to create a detailed global map of the diffusive and burial flux of dissolved magnesium across the sediment-water interface using a machine learning regression with several globally-gridded environmental parameters. In addition, the isotopic fractionations associated with those fluxes are calculated using data from a variety of ocean drilling locations and extrapolated globally using a lithologically-binned regression. These analyses show that the magnesium flux into marine sediments accounts for about 15 – 20% of the magnesium sink from the ocean, with a flux-weighted fractionation factor of approximately 0.9997 acting to increase the magnesium isotopic ratio in the ocean. This analysis of global magnesium fluxes and isotopic fractionation provides the best constraints to date on the sources and sinks that define the oceanic magnesium cycle, including new constraints on the loss of magnesium during low-temperature ridge flank hydrothermal circulation.

The in situ reactions influencing the magnesium flux into marine sediments are also important for other oceanic geochemical cycles, such as the oceanic alkalinity, ^{13}C, and $H_2{}^{18}O$ cycles, as well as mineral-bound water delivery to subduction zones. A new multicomponent

reactive transport model is applied to nine ocean drilling cores, including sites characterized by pelagic and hemipelagic sedimentation. The model results indicate that authigenic clay formation in the deep subsurface (>1 meter below seafloor) is a widespread process that accounts for up to 5 wt% of the bulk sediment. The rate of authigenic clay formation in the deep subsurface could amount to the equivalent of a few percent of the total sediment input into the ocean from rivers, and up to 5% of the structural water content of subducting sediment. This geochemical sink of ^{18}O-enriched structural water may account for the imbalance calculated in the 10^8-year oxygen isotope budget of the ocean. The model indicates that the rates of authigenic carbonate formation in the upper sediment column are underestimated by a factor of at least 1.5 to 2 by models that solely utilize the calcium concentration profiles, suggesting authigenic carbonate formation has a greater role in the ^{13}C cycle of the ocean than previously estimated. The results from this study add further support to evidence for the importance of authigenic mineral formation reactions in global geochemical cycles.

TABLE OF CONTENTS

LIST OF FIGURES

LIST OF TABLES

ACKNOWLEDGEMENTS

This work would not have been possible without the support of my advisor, Evan Solomon. His guidance and patience have allowed me to pursue many great opportunities in research, fieldwork, teaching, and professional development. His dedication to rigorous science and focus on important and interesting questions has been inspirational to both my research and professional pursuits.

The guidance and insights of the other members of my supervisory committee are greatly appreciated and have helped to further improve the quality and focus of my work. Deb Kelley, Steve Emerson, Curtis Deutsch, Bob Morris, and Rick Keil have each individually and as a group been formative in my development as a scientist and as a professional. In addition, I'm grateful to Fang-Zhen Teng for facilitating magnesium isotope measurements in his Isotope Lab at the UW, and contributing his expertise to this work.

I also thank the other members of the Solomon Lab for their support in the lab, field, and office: Theresa Whorley, Brendan Philip, Daniel Culling, and Paige Farrell. Special thanks to Theresa Whorley, who has been a great officemate and essential for discussing ideas in depth and whiteboarding problems, and Brendan Philip, who's talent at exploring wide-ranging ideas and new directions has also been invaluable. I'd also like to thank the students in the lab that I have helped train and mentor, Marisa Borreggine, Garrett Raehild, Jaime Fields, Lauren Kowalski, and Kyler Kruger, all of whom have taught me a great deal in return.

I am also grateful for the assistance, advice, and guidance that I've received from a range of others in every aspect of this work. I thank Miriam Kastner, for always being available for

valuable discussion and advice about my research, and providing archived fluid samples for Mg isotopic analysis. The mentorship of Marta Torres at sea, and her facilitation of lab time and fluid samples for analysis, are appreciated and improved the quality of this work. Additionally, I thank Yan Emma Hu, Shui-Jiong Wang, and Aaron Brewer for help in the UW Isotope Laboratory, and Don Sims and Sean Toczko for assistance navigating the various ocean drilling databases.

Finally, I'd like to thank my family for their unwavering support and encouragement.

Chapter 1. INTRODUCTION

1.1 CONSERVATIVE ELEMENT CYCLING IN THE OCEAN

Element concentrations in the ocean are controlled by exchange with the lithosphere and atmosphere through a variety of physical, chemical, and biological processes on a range of timescales (Berner and Berner, 2012). Conservative elements are those whose concentration changes on timescales much longer than the mixing time of the ocean. The concentrations of the conservative elements in the ocean are a function of salinity, with very little spatial variability due to other factors (Millero et al., 2008). The conservative element composition of the ocean is determined by the magnitudes of the sources into the ocean and sinks from the ocean, operating on timescales of $10^5 – 10^8$ years (Mackenzie and Garrels, 1966). Rivers and groundwater are sources of elements, bringing continental weathering products into the ocean in dissolved and particulate form. Other processes can be either sources or sinks for different elements. For example, alteration of the basaltic oceanic crust during hydrothermal circulation is a sink for many elements, such as magnesium and sulfur, but a source for others, such as calcium and lithium (Elderfield and Schultz, 1996; Seyfried and Bischoff, 1979).

Understanding the magnitudes of the sources and sinks for any given conservative element provides constraints on its residence time in the ocean and insight into the timescale over which its concentration can vary in response to changes in those sources and sinks. Perhaps more importantly, paleo-oceanographic records of the variability of conservative element concentrations and isotope ratios in the ocean provide insight into the temporal variability of the geologic and biological processes that regulate the sources and sinks (Broecker and Yu, 2011; Gothmann et al., 2017; Higgins and Schrag, 2015; Misra and Froelich, 2012). This aspect of

conservative element cycling in the ocean is important because some of these processes are fundamental to several major element cycles simultaneously, including carbon (Lasaga et al., 1985). Conservative-element-based interpretations of long-term changes in processes such as weathering of continental crust, carbon burial in marine sediments, biological productivity, and hydrothermal circulation connect these conservative element cycles to long-term changes in paleo-environmental conditions on Earth.

1.2 CHEMICAL REACTIONS IN MARINE SEDIMENTS AS CONTROLS ON OCEANIC GEOCHEMICAL CYCLES

Marine sediments are important for a number of elemental cycles in the ocean due to diagenetic reactions that occur as sediment is deposited and buried on the seafloor (Berner and Berner, 2012). Diagenesis refers to all of the physical, chemical, and biochemical changes that occur to sediment after deposition, but prior to metamorphic alteration at temperatures above ~150 ℃ (Berner, 1980). Several types of chemical reactions occur in marine sediments, including biogeochemical reactions driven by the microbially-mediated degradation of organic matter, inorganic water-rock reactions, and cation exchange reactions. Through these diagenetic reactions, the alteration of sediments results in a change in the pore water solute concentrations and isotopic ratios over time.

The difference in composition between the pore water and the overlying seawater creates a diffusional gradient, driving a flux of solutes either into or out of sediments. Exchange between the ocean and sediments can also occur by advection of chemically-distinct pore waters in certain environments. For example, near mid-ocean ridges with a thin veneer of sediment, hydrothermally-driven advection can occur, with advection rates dependent on the thickness and

permeability of the sediment cover e.g. (Anderson et al., 2014; Anderson et al., 1977). Advection can also occur at convergent margins, where tectonic compaction can drive fluid flow to the surface through diffuse upward flow or in focused flow along fault networks or permeable horizons such as sandy turbidite deposits e.g. (Davis et al., 1990; Kastner et al., 2014; Saffer and Bekins, 1998).

1.2.1 *Biogeochemical reactions and the deep subseafloor biosphere*

Biogeochemical reactions are driven by the microbially-mediated degradation of organic matter that fuels one of Earth's largest ecosystems, the subseafloor deep biosphere (Edwards et al., 2012; Parkes et al., 2005). Defined as the microbial ecosystem that exists in the sediment, rock, and pore water environment deeper than about 1 meter below seafloor, the deep biosphere spans the entire area of the seafloor, to depths of up to several kilometers (Edwards et al., 2012; Jørgensen and Boetius, 2007; Kallmeyer et al., 2012). These biogeochemical reactions can change the chemical composition of pore waters, including alkalinity, pH, and oxidation-reduction potential, which then drive further reactions between the pore water and the sediments.

The biogeochemical reactions that take place within the deep biosphere include the redox reactions that form the "redox ladder" in marine sediments, as well as other catabolic reactions such as fermentation and organohalide respiration. The redox ladder is the thermodynamic sequence of electron acceptors that microbes utilize to metabolize organic matter in marine sediments (Claypool and Kaplan, 1974; Froelich et al., 1979; Hoehler et al., 1998; Stumm and Morgan, 2012). Oxygen respiration typically persists at shallow subseafloor depths closest to the sediment-water interface, followed by reduction of nitrate, manganese oxides, iron oxyhydroxides, and sulfate with increasing depth (Figure 1.1). Below the depth of sulfate

reduction, methanogenesis is typically the dominant microbially-mediated redox process. Between the sulfate reduction zone and the methanogenic zone, is a centimeter- to meter-scale depth interval called the sulfate-methane transition zone (SMTZ). At the SMTZ, a consortium of archaea and bacteria metabolize sulfate and methane in a process known as anaerobic oxidation of methane (AOM) (Boetius et al., 2000; Hoehler et al., 1994).

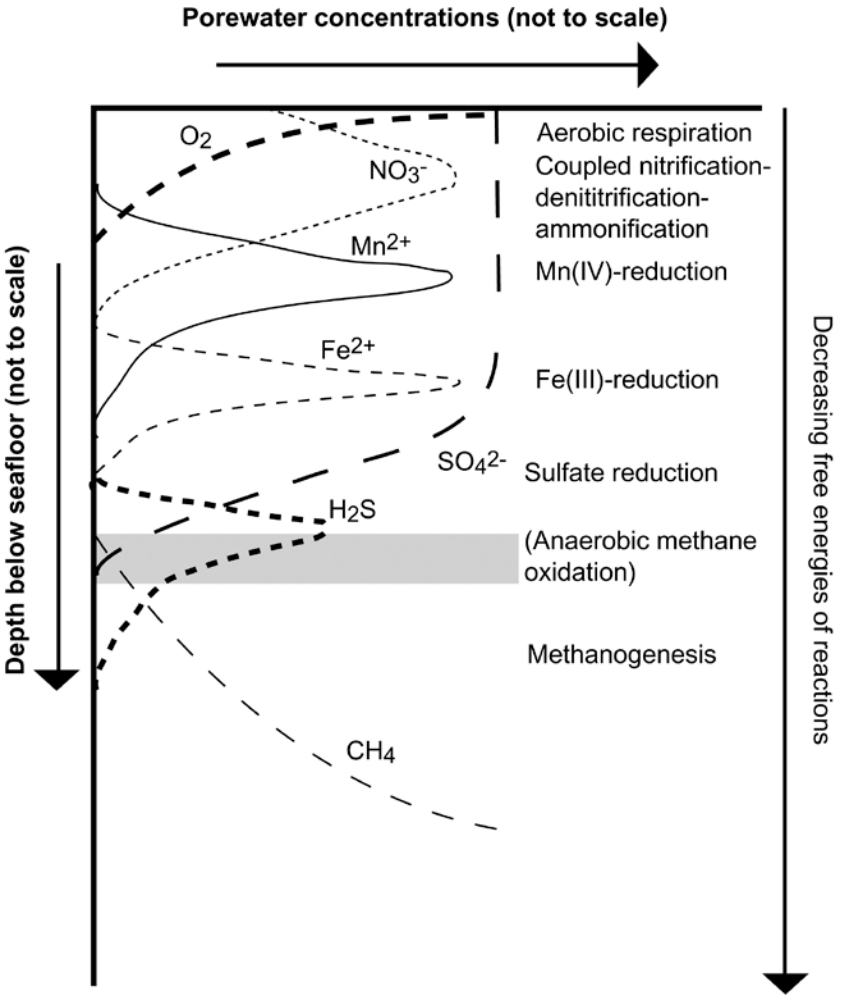

Figure 1.1. The “redox ladder” in marine sediments. Figure modified from Froelich et al., 1979.

Fermentation is an anaerobic metabolic pathway that acts through the disproportionation of organic molecules, in which organic molecules are split into smaller molecules, with one product being oxidized and the other product reduced (Nealson, 1997). Many forms of fermentation occur at all depths in marine sediments, producing end-products such as H_2, CO_2, acetate, and lactate that are metabolized by other anaerobic microbes (Nealson, 1997).

Organohalide respiration is the utilization of halogenated organic molecules as electron acceptors in microbial metabolic redox processes (Orcutt et al., 2011). Being an energy-rich metabolic pathway, organohalide respiration has a wide geographic and depth distribution in marine sediments (Dolfing, 2003; Fetzner, 1998; Mohn and Tiedje, 1992). Depth-integrated rates of organohalide respiration are much lower than other metabolic pathways such as sulfate reduction or methanogenesis, but the process may be important in the cycling of bromine, and provides energy to dehalogenating bacteria (Berg and Solomon, 2016).

1.2.2 *Water-rock reactions*

Water-rock reactions involve the *in situ* dissolution, precipitation, or recrystallization of inorganic solids. Dissolution, or weathering, of inorganic solids can releases elements that may be equal or unequal to the molar proportion originally found in the solid, known as congruent or incongruent dissolution, respectively. For example, the dissolution of $CaCO_3$ to Ca^{2+} and CO_3^{2-} is congruent since the ions are released to solution in the same molar proportion as in the solid mineral. Incongruent dissolution is the selective release of elements from the solid, often associated with a concurrent uptake of other elements from the pore water, which results in a new residual mineral. Incongruent dissolution is common with aluminosilicates during early diagenesis in the marine environment, such as the weathering of plagioclase to smectite clay

(Kastner, 1981). Both congruent and incongruent weathering can help drive the dissolution of sedimentary minerals with the production of acidic metabolic byproducts, such as CO_2 or organic acids, which can ultimately influence biogeochemical cycles e.g. (Solomon et al., 2014; Wallmann et al., 2008).

Precipitation of inorganic solids, including carbonates and silicates, is also a common process in marine sediments during early diagenesis. For example, in regions with high organic carbon burial, biogeochemically-driven increases in pore water alkalinity and pH can lead to the precipitation of authigenic carbonates. More carbonates precipitate with increasing carbonate saturation state and CO_3^{2-} concentrations, which are a function of alkalinity and pH (Morse and Mackenzie, 1990). Changing pore water conditions can also drive the precipitation of silicates in marine sediments, as silicon, aluminum, and other cations are dissolved from other minerals and precipitated as more stable minerals in the sediment pore spaces (Gieskes and Lawrence, 1981; Kastner, 1981).

1.2.3 *Equilibrium Cation Exchange*

Exchange of cations between pore water and charged surfaces of sediment particles, such as clays, occurs as an equilibrium adsorption/desorption process (Berner, 1980). Particle surfaces are charged for a variety of reasons, including isomorphous substitution, incomplete occupation of the positions available for metal ions and release of protons from surface hydroxides (Weaver and Pollard, 2011). At the pH ranges typically found in marine sediments, the surfaces of clay minerals have a net negative charge due to the release of the hydrogen from outer hydroxide groups of the Al-OH or Si-OH layers, with greater negative charge in more basic solutions

(Weaver and Pollard, 2011). Different clay types have varying degrees of cation exchange capacity (CEC), with clays of higher surface area having higher CECs.

As particles in marine sediments are buried deeper, other diagenetic reactions alter the surrounding pore water chemistry, leading to re-equilibration of the adsorbed cations. For example, as organic matter is buried and degraded in anoxic sediments, ammonium concentrations in pore water increase, causing adsorption of ammonium with concurrent desorption of other cations (Mackin and Aller, 1984). This effect can be clearly observed in pore water chemistry profiles from the Peru margin, where ammonium concentrations reach concentrations of up to 63 mM, with associated desorption of magnesium contributing to pore water concentrations of magnesium of over 100 mM (Suess and von Huene, 1988). In this way, equilibrium cation exchange can be a significant source or sink of cations within the sediment column, and can act as a buffer to changes in pore water concentrations of a given solute that are driven by other reactions.

1.3 QUANTIFYING REACTIONS IN MARINE SEDIMENTS

Although chemical reactions in marine sediments are ubiquitous, the changes that solid-phase sediments undergo during early diagenesis can be difficult to measure. This is due to the small magnitude of the diagenetic changes relative to the natural variability in the bulk composition of the sediment that is deposited over time. However, pore water chemistry-depth profiles provide a much more sensitive approach to characterizing and quantifying the reactions that are taking place in the sediment column. For example, in a sediment with 20% $CaCO_3$ at 60% porosity, precipitation of 0.5 kg of $CaCO_3$ per m^3 would increase the $CaCO_3$ content by about 0.25%, over an order of magnitude less than the typical ~3% analytical precision for bulk $CaCO_3$ content.

However, precipitation of that same 0.5 kg of $CaCO_3$ would deplete the pore water concentration of calcium by over 8 mM, over two orders of magnitude greater than the analytical precision for pore water calcium concentrations.

The challenge with using pore water concentrations and isotopic ratios to quantify *in situ* chemical reactions is that solutes are mobile in the dissolved phase through diffusion and pore water advection, and that the pore water values represent the net effect of all diagenetic reactions occurring in the sediments (Berner, 1980). To constrain the effects of these processes and characterize the reactions occurring using pore water chemistry-depth profiles, the reactions and transport mechanisms occurring in the system must be modeled (Boudreau, 1997). Several forms of reactive-transport models exist, and are useful for investigating a range of processes in the marine environment including geochemical reaction rates and distribution, fluid flow, element transfer between the ocean and lithosphere, and the dynamics of geochemical exchange and storage. For investigating reaction rates and distributions, the models minimize the issue of the high mobility of solutes by parameterizing the processes of diffusion, externally-driven advection, sedimentation, and bioturbation. To investigate rates of reaction and distribution of elements using reactive-transport models, data are required that provide the geochemical and geophysical constraints necessary for model parameterization and error analysis.

The suite of geochemical and geophysical data collected during scientific ocean drilling expeditions is particularly well-suited to investigating early diagenetic processes using inverse reactive-transport modeling. The length scale of ocean drilling data is on the order of meters to kilometers. Depth profiles of sediment porosity, age, temperature, and pore water composition at this length scale provide the necessary information for parameterizing diffusion, advection, and sedimentation. Over 1500 unique sites have been sampled as part of Deep Sea Drilling Project,

Ocean Drilling Program, Integrated Ocean Drilling Program, and International Ocean Drilling Program expeditions from a wide variety of ocean environments from 1968 to today. Data and reports from all of these scientific ocean drilling expeditions are archived and available from their respective repositories. This ongoing scientific endeavor provides a rich dataset which can be used in full to evaluate processes on a global scale, or can be supplemented with new measurements to investigate diagenetic processes in more detail in select environments.

1.4 Dissertation Summary

In Chapter 2, new measurements of solid-phase organobromine concentrations are combined with reactive-transport modeling of pore water bromide concentrations from continental margin ocean drilling locations to better understand the dynamics of dehalogenation in the deep biosphere. In Chapter 3, the full scientific ocean drilling dataset is combined with new measurements of pore water magnesium isotope ratios and utilized to estimate the global flux of magnesium across the sediment-water interface and to make the first estimate of the isotopic fractionation associated with the global magnesium flux. In Chapter 4, a new multicomponent reactive-transport model is applied to scientific ocean drilling datasets from nine locations, and combined with the down-core measurements of magnesium isotopic ratios, to investigate the magnitudes of authigenic mineral precipitation and recrystallization reactions that affect global geochemical cycles.

Chapter 2. GEOCHEMICAL CONSTRAINTS ON THE DISTRIBUTION AND RATES OF DEBROMINATION IN THE DEEP SUBSEAFLOOR BIOSPHERE

ABSTRACT

Organic matter in marine sediments is degraded through a range of diverse metabolic pathways which are dependent on substrate availability, environmental conditions, and microbial ecology. The rates and systematics of these metabolic reactions affect long-term global geochemical cycles and the degradation of organic matter in the subsurface marine environment. Organohalide respiration is one of these pathways that has been hypothesized to be widely active in the deep biosphere, with carbon-halogen bonds being broken through microbially-mediated redox reactions. Besides directly providing energy to microbes in marine sediments and allowing bromine to cycle back into the overlying ocean, organobromine respiration may also be closely linked to nitrogen and carbon cycling in anoxic marine sediments. Here we investigate the distribution and rates of debromination by tracking the production of dissolved bromide (Br^-) with depth in pore water sampled at several continental margins. Pore water profiles of Br^- and ammonium (NH_4^+) concentrations from the Krishna-Godavari (K-G) basin on the southeastern margin of India indicate a common distribution of rates of debromination and NH_4^+ production in continental margin sediments, and suggest that the pools of bioavailable nitrogen and organobromine compounds are likely geochemically associated at these sites. Dissolved Br^- and total solid-phase bromine concentration profiles from the K-G basin and Costa Rica margin indicate the most rapid debromination occurs in the upper 10 – 20 m of the sediment column. The rates of debromination in the sediment column from the Costa Rica, Cascadia, and Nankai

margins are estimated using numerical reaction-transport modeling of pore water Br^- concentration profiles to constrain the maximum amount of metabolic energy that could be provided to the microbial communities through organobromine respiration. Because other debromination processes may also be responsible for an unknown fraction of these geochemically-derived rates, the modeled rates of debromination provide an upper limit to organobromine respiration activity. Modeled rates of debromination on the order of 10^1 to 10^3 μmol m^{-2} y^{-1} indicate that the maximum amount of energy that is potentially provided through organobromine respiration is low relative to other metabolic pathways such as sulfate reduction and methanogenesis. However, organobromine respiration may still serve an important niche in the microbial community and debromination is an important part of the oceanic bromine cycle.

2.1 INTRODUCTION

Understanding the mechanisms of organic matter degradation in marine sediments is important for understanding long-term global biogeochemical cycles and microbial metabolic processes in the deep biosphere. Bromine is present in both terrestrial and marine organic matter as organobromine compounds, and a direct correlation between bromine content and organic carbon content of marine sediments has been demonstrated by several authors (Lange, 1970; Leri et al., 2010; Martin et al., 1993; Pedersen and Price, 1980; Price and Calvert, 1977; Price et al., 1970; Ziegler et al., 2008). During organic matter degradation in marine sediments, bromine can be removed from organobromine compounds through microbial metabolic or abiotic debromination processes. One metabolic pathway in the degradation of organic material that has been shown to be potentially widespread throughout the marine sedimentary environment is organohalide respiration (Orcutt et al., 2011). During organohalide respiration, bacteria in anoxic environments utilize reductive dehalogenases to break the carbon-halogen bond of organohalide compounds, with the organohalide functioning as the electron acceptor and the bromine being replaced by a hydrogen atom (Dolfing, 2003; Fetzner, 1998; Mohn and Tiedje, 1992). Microbial genomic studies in deeply-buried methanogenic sediments from ocean drilling expeditions have identified putative organohalide-respiring bacteria as abundant groups (Biddle et al., 2008; Martino et al., 2013), and identified an array of genes coding for reductive dehalogenases (Futagami et al., 2009; Futagami et al., 2013). Organohalide respiration has been widely studied in cultures and incubation experiments as well, and shown to be a viable respiration pathway for several strains of bacteria utilizing various organohalogens (Fetzner, 1998; Mohn and Tiedje, 1992; Yang et al., 2015). In addition, organohalide respiration can occur within syntrophic communities of fermenters and methanogens in some environments, connecting dehalogenation

with the carbon and nitrogen cycles (Mohn and Tiedje, 1992). Less is known about organohalide fermentation, but it has been shown to be another potentially energy-producing pathway for microbes in the deep biosphere (Dolfing; Justicia-Leon et al., 2012; Lee et al., 2012).

Though the various forms of microbially-mediated dehalogenation are likely fueling some metabolism in the deep biosphere, the amount of energy provided to the microbes through these pathways remains unknown (Lever, 2013; Orcutt et al., 2011; Valentine, 2011). Bacterial groups that may have the potential to use organohalide respiration as a metabolic pathway have been found to be abundant in deep subsurface marine sediments, both geographically and with depth (Biddle et al., 2008; Futagami et al., 2013; Inagaki et al., 2006; Martino et al., 2013; Orcutt et al., 2011). Due to the abundance of these putative dehalogenators, it has been hypothesized that this metabolic pathway may be an important energy source for microbial communities in the deep biosphere (Futagami et al., 2013; Lever, 2013). The energy yield of organohalide respiration in the natural environment can be several times greater, on a per mole basis, than other metabolic pathways such as sulfate reduction and methanogenesis (Dolfing, 2003). However, the amount of halogenated substrate is much lower than the bulk organic substrate fueling sulfate reduction and methanogenesis, and may result in much lower total energy yields through time.

Coarse-resolution solid-phase bromine profiles from the Peru margin have demonstrated that with increasing bromide concentrations in the pore water, there is a corresponding decrease in the total solid-phase bromine concentrations in deeply-buried marine sediments (Martin et al., 1993; von Breymann et al., 1990b). Further, a decrease in the bromine to organic carbon ratio (Br:OC) with depth in sedimentary organics has also been measured, indicating that bromine is preferentially released from bulk organic matter during degradation (Martin et al., 1993; Upstill-

Goddard and Elderfield, 1988; von Breymann et al., 1990b). However, variable initial solid-phase bromine concentrations, due to variations in the organic matter source and supply rate, makes solid-phase bromine an unreliable tracer for debromination rates in marine sediments. In contrast, pore water bromide concentration profiles can be used to detect and quantitatively characterize debromination in marine sediments. During diagenesis of organic matter in the marine sedimentary environment, bromine is released from organic matter as the bromide ion, resulting in an increase in pore water bromide concentrations with depth (Mahn and Gieskes, 2001; Martin et al., 1993; Mun and Bazilevich, 1962; von Breymann et al., 1990b). Once bromide is released into anoxic pore waters, no significant chemical uptake processes are known to act as a sink for the bromide, and dissolved bromide can be used as a conservative tracer of debromination of sedimentary organic matter (Mayer et al., 1981; Upstill-Goddard and Elderfield, 1988; von Breymann et al., 1990b).

Using pore water bromide as a conservative tracer for debromination in marine sediments, rates of bromide production (debromination) can be calculated from bromide concentration-depth profiles using reactive-transport modeling. With this approach, modeled rates reflect total rates of bromide release to the pore water from all debromination pathways. These pathways may include organohalide respiration, fermentation, fortuitous dehalogenation through co-metabolic processes or direct cofactor catalysis, or abiotic dehalogenation (Dolfing, 2003; Mohn and Tiedje, 1992). While the modeled rates derived from the geochemical data cannot discriminate between the various possible dehalogenation pathways, they can be used to constrain the maximum potential rates of organobromine respiration in the marine sediment column. The rates of debromination from several margins presented in this study offer a first-

order comparison between maximum *in situ* organobromine respiration rates and other known redox pathways in deep marine sediments.

2.2 METHODS

2.2.1 *Study Sites*

The primary datasets for this study were collected using the D/V JOIDES Resolution during the Indian National Gas Hydrate Program (NGHP) Expedition 01 (Collett et al., 2008; Solomon et al., 2014), and Integrated Ocean Drilling Program (IODP) Expeditions 334 and 344 (Figure 2.1a and b) (Harris et al., 2013; Vannucchi et al., 2010). NGHP Expedition 01 Sites 5 (16°01.722’ N, 82°02.677’ E), 14 (16°03.5577’ N, 82°05.6218’ E), 15 (16º 05.6983’ N, 82º09.7467’ E), and 20 (15°48.5671’ N, 81°50.5760’ E) are in the Krishna-Godavari (K-G) basin, a passive continental margin offshore southeast India. These sites are characterized by hemipelagic sedimentation influenced by the high sediment loads from the Krishna and Godavari rivers. Long-term sedimentation rates in the K-G basin are not well constrained, however recent estimates of sedimentation rates in the upper 8 – 25 meters of the sediment column are very high, in the range of hundreds to thousands of cm/ky (Hong et al., 2014; Mazumdar et al., 2007; Ramprasad et al., 2011). IODP Expeditions 334 and 344 Sites U1378 and U1412 are located on the southern Costa Rica convergent margin offshore the Osa Peninsula. Site U1378, located at 8°35.5414’ N, 84°4.6306’ W, is a mid-slope site, and is characterized by hemipelagic sedimentation with sedimentation rates of 24 – 52 cm/ky (Vannucchi et al., 2012b). Site U1412, located at 8°29.3294’ N, 84°7.6686’ W, on the prism toe, is also characterized by hemipelagic sedimentation, with long-term average sedimentation rates of 5 – 10 cm/ky (Harris et al., 2013).

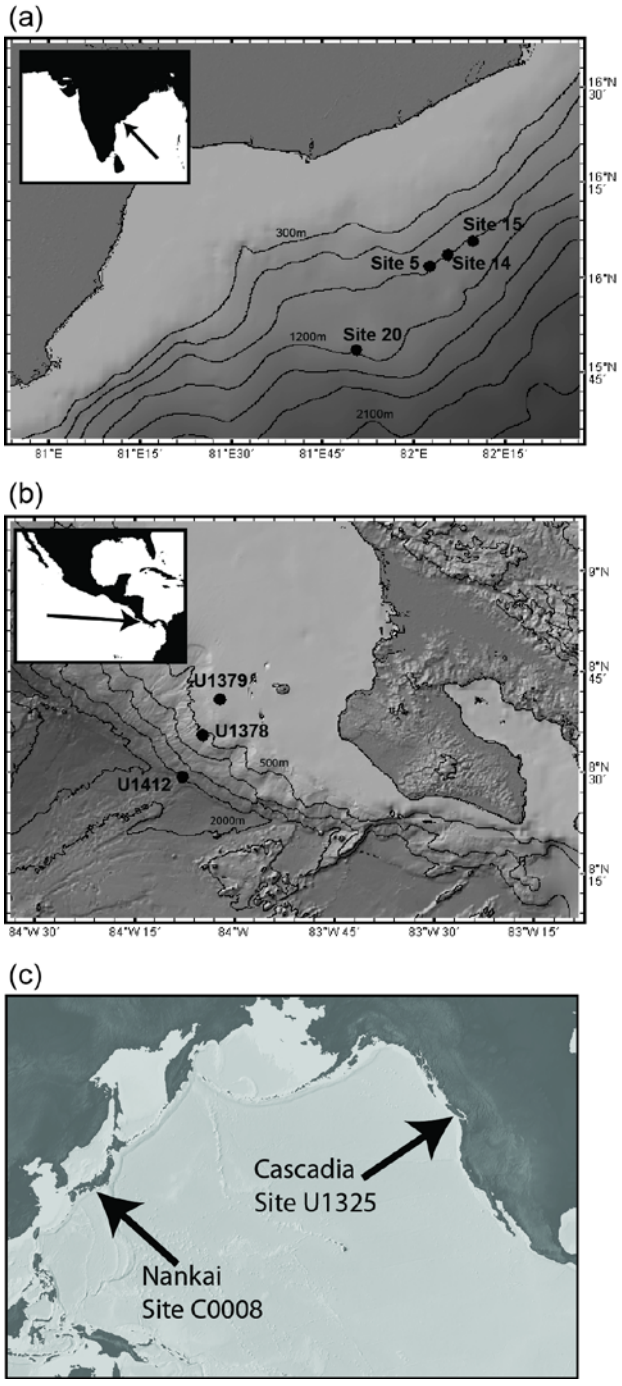

Figure 2.1. A) Bathymetric map showing the Krishna Godavari basin on the southeastern Indian margin and the location of National Gas Hydrate Program Expedition 01 Sites 5, 14, 15, and 20. B) Bathymetric map showing the Costa Rica convergent margin off of the Osa Pennisula and the location of Integrated Ocean Drilling Program Site U1412 from Expedition 344 and Sites U1378 and U1379 from Expedition 334. C) Map showing the locations of Site U1325 on the Cascadia margin and Site C0008 on the Nankai margin.

Additional data presented in this paper were collected from the Cascadia margin offshore Vancouver Island and the Nankai margin offshore southern Japan (Figure 2.1c) (Fehn et al., 2006; Kinoshita et al., 2009b). Site U1325 at the Cascadia margin was sampled during IODP Expedition 311 and Site C0008 at the Nankai margin was sampled during IODP Expedition 316. Site U1325 is located at 48°38.691' N, 126°58.991' W, in the first slope basin east of the deformation front, and is characterized by hemipelagic sedimentation with interlayered turbiditic sand layers, and sedimentation rates of 20 – 80 cm/ky (Fehn et al., 2006). Site C0008 is located at 33°12.8229' N, 136°43.5997' E, in a mid-slope basin, and is characterized by hemipelagic sedimentation with interbedded sands and gravels in the upper ~270 m, with deeper thick sand-rich turbidite layers, and sedimentation rates of 5 – 20 cm/ky (Kinoshita et al., 2009b).

2.2.2 *Sample collection and pore water analyses*

Cores were collected, processed, and analyzed as described in Harris et al. (2013), Collett et al. (2008), Solomon et al. (2014), and Vannucchi et al. (2012b). Whole-round core sections for pore water geochemical analyses were extruded from the core liner, cleaned of potential contamination, and placed in titanium squeezers in a hydraulic press for pore water extraction (Manheim and Sayles, 1974). Extracted pore water was filtered (Millipore 0.45 μm), and the dissolved bromide and sulfate concentrations were immediately measured shipboard on a Metrohm 861 Advanced Compact Ion Chromatograph during NGHP Expedition 01 and IODP Expedition 344 with 1 – 2% relative standard deviation (Collett et al., 2008; Harris et al., 2013). Bromide and sulfate concentrations in filtered pore water from IODP Expedition 334 Site U1378 were measured at the University of Washington using a Metrohm 882 Compact IC Plus Ion

Chromatograph, with <1% relative standard deviation (Tables A5 and A6). Pore water ammonium concentrations from all sites were analyzed spectrophotometrically, with <2% relative standard deviation (Collett et al., 2008; Harris et al., 2013; Schrum et al., 2009; Vannucchi et al., 2012b).

2.2.3 *Total dissolved bromine analysis*

Significant pore water concentrations of dissolved organobromine compounds in relation to bromide ion concentrations would indicate slower rates of dehalogenation than rates of hydrolysis of solid-phase organics, and could imply suppression of the dehalogenation process. In addition, diffusion of dissolved organohalides away from the original solid-phase source would affect modeled rates of *in situ* debromination of solid-phase organic matter. To test for significant concentrations of bromine bound to dissolved organic molecules in pore waters, a subset of 21 pore water samples from IODP Expedition 344 Site U1412A were diluted 201 times with ultra-purified water and placed in 10 cc fused quartz test tubes (Technical Glass Products, 1.5 mm wall thickness), plugged with silicone stoppers, and treated for 6 hours using an ultraviolet (UV) irradiation unit (La Jolla Scientific Co, model #PO-14) to oxidize the organobromine compounds, similar to the method discussed in Pandiyan et al. (2002). The UV treatment releases bromine as bromide in solution. The samples were then analyzed for bromide concentration using a Metrohm 882 Compact IC Plus ion chromatograph at the University of Washington, with <1% relative standard deviation. Solutions of 0.87 mM 4-bromophenol and 0.43 mM dibromoacetic acid (Sigma Aldrich analytical standards), also diluted 201 times with ultra-purified water were used as representative organohalide test standards to verify the effectiveness of the method. Bromide ion concentrations in the test standard solutions were

measured before treatment with UV, after four hours of treatment, and after 6 hours of treatment to find the treatment time needed for full debromination.

2.2.4 *Solid-phase bromine analyses*

Solid-phase bromine concentrations were measured in a total of 27 samples from K-G basin Site 14, 27 samples from K-G basin Site 20, and 35 samples from Costa Rica Site U1412 (Tables A1 – A3). Prior to analysis, dry whole-round squeezed sediment cakes were subsampled and ground by hand in an agate mortar for sample homogenization. Homogenized samples were then placed in 14 mL centrifuge tubes and put through four cycles of rinsing, which consisted of filling the test tubes with ultra-purified water, centrifuging until the supernatant was clear, and decanting to remove residual salts from pore water evaporation. After rinsing, the samples were dried and analyzed at the Oregon State University Radiation Center via instrumental neutron activation analysis (INAA). Concentrations were determined using the direct comparison method, relative to mean activities generated in three replicates of the NIST standard 1632a (bituminous coal). Replicates of the NIST standards composed of spinach (NIST1570 and NIST1570a) were included in each batch as check standards (Table A4). The average standard deviation of the bromine analyses is ±0.65 ppm.

2.2.5 *Reactive-transport modeling of debromination rates*

To estimate the rates of debromination in the sediment column at Costa Rica Sites U1412 and U1378, Cascadia Site U1325, and Nankai margin Site C0008, a numerical modeling method based on the measured pore water bromide concentration profiles was used. The numerical

modeling method was created specifically to quantify net metabolic reaction rates in marine sediments (Wang et al., 2008). The model uses a Matlab-based centered finite-difference method to calculate average net rates of chemical reaction within discrete, statistically significant zones in the sediment column. The model explicitly considers molecular diffusion in the sediment pore space, pore water advection, pore water burial rate, and chemical reaction, with the assumption of steady-state. Because the K-G basin sites are known to be out of steady state due to recent mass-transport deposits (Hong et al., 2014), the debromination rates at those sites were not quantified. Inputs to the model include sedimentation rate, diffusion coefficient, pore water advection rate, and depth profiles of porosity, formation factor, temperature, and analyte concentration. A diffusion coefficient for bromide of 5.56×10^{-2} m^2 y^{-1} at 18°C (Li and Gregory, 1974) was used, and varied with depth based on the measured temperature gradients at each site. The model was modified to use porosity to estimate the tortuosity of the sediment by the relationship $\theta^2=1-\ln(\varphi^2)$ (Boudreau, 1996). Model parameters are given in Table 2.1. A Monte Carlo method was used to estimate the 1σ uncertainty of the calculated rates. This numerical method has been used previously to successfully quantify net chemical reaction rates in marine sediments (Wang et al., 2008).

Table 2.1 Parameters used in the reactive-transport modeling of debromination rates.

	IODP 311 Site U1325	IODP 316 Site C0008	IODP 334 Site U1378	IODP 344 Site U1412
Surface sedimentation rate range (m/y)	0.00039 - 0.0016	0.000088 - 0.00035	0.00047 - 0.00085	0.000091 - 0.00018
Measurement precision (%)	2	2	2	2
Temp gradient (°C/m)	0.06	0.051	0.0514	0.114
Bottom water temp (°C)	3	2	8.15	2.25
Porosity at depth	0.45	0.47	0.45	0.58
Pore water advection (m/y)	0	0	0	0

2.3 RESULTS

The pore water bromide concentrations at all of the sites increase with depth, but with a decreasing gradient in the lower sediment column (Figure 2.2). However in contrast to the bromide profiles from other margins, bromide profiles from the K-G basin exhibit distinct zones within the sediment column. Bromide concentrations at K-G basin Sites 5, 14, 15 and 20 increase very little with depth in the upper 10 – 20 meters below seafloor (mbsf), then exhibit a relatively rapid increase with depth until reaching a sharp decrease in gradient between 30 – 90 mbsf (Figure 2.2). The small bromide concentration gradients observed within the upper 10 – 20 mbsf are likely due to recent mass transport deposits in the upper 8 – 18 meters in the K-G basin, resulting in non-steady-state solute profiles in the upper sediment column at these sites (Hong et al., 2014).

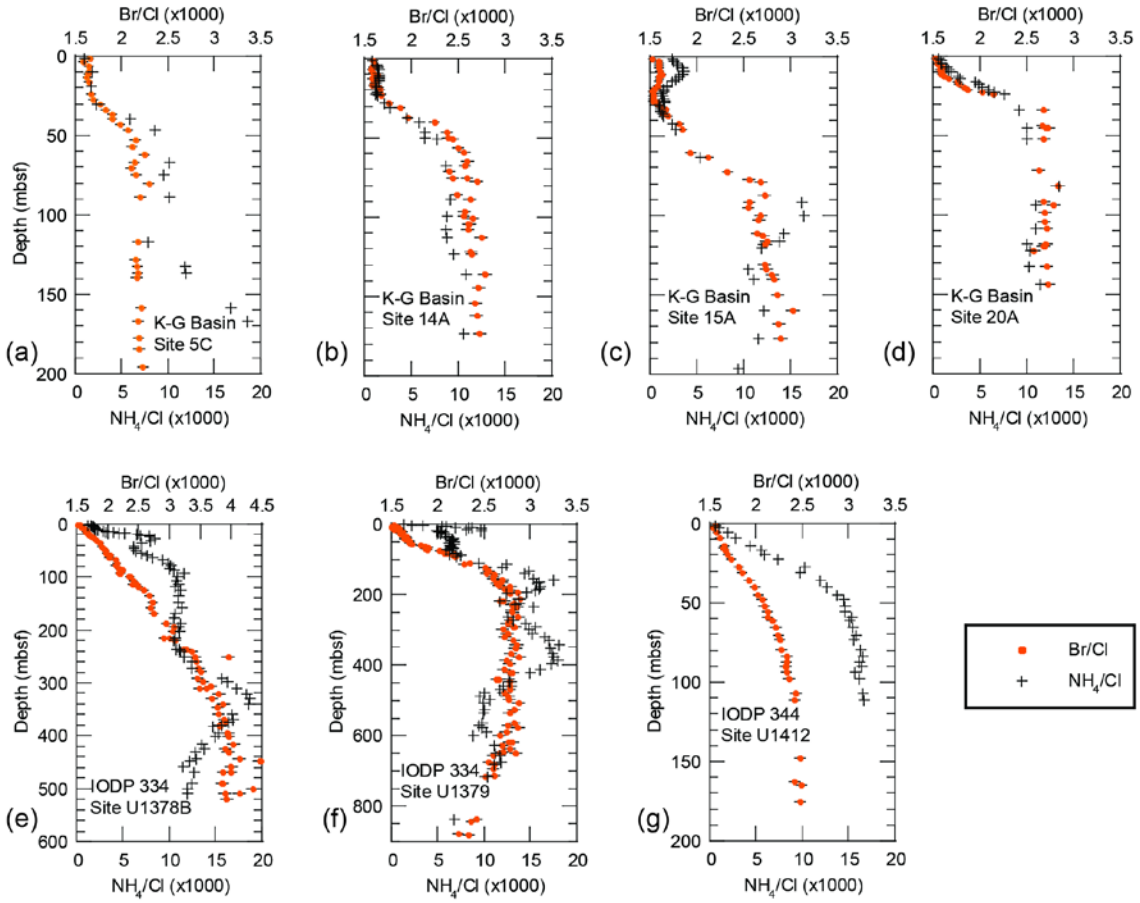

Figure 2.2. Pore water molar ratios of bromide/chloride and ammonium/chloride from K-G basin Sites 5C, 14A, 15A, and 20A, and Costa Rica margin (IODP 334 and 344) Sites U1378B, U1379C, and U1412A. Bromide is normalized to chloride to correct for potential dilution effects caused by dissociation of gas hydrates. 2% error bars are shown for bromide measurements; ammonium error bars are smaller than symbols.

Though ammonium is not conserved in marine sediments due to sorption reactions with clay minerals and organic matter, anabolic uptake by microbes, and other potential redox reactions (Krüger et al., 2008; Mackin and Aller, 1984; Schrum et al., 2009), a distinct correlation exists between the shape of the bromide and ammonium profiles at the K-G basin sites (Figure 2.2). The depths at which sharp gradient changes are present in the pore water profiles of bromide are also seen in ammonium profiles. The shallow bromide and ammonium gradient increase at the K-G Basin sites is due to the recent mass transport deposits (Hong et al.,

2014). A deeper gradient decrease is present in the ammonium and bromide concentration profiles from the K-G basin and Costa Rica Sites U1379C and U1412A. The bromide profiles at Site U1378B and U1379C are not well-correlated with the ammonium profiles, likely due to sorption or metabolic reactions affecting the ammonium concentrations in the sediment column, and fluid advection in deeper sediments (Solomon et al., 2011; Torres et al., 2013). The common sharp gradient changes in the bromide and ammonium profiles observed at all of the K-G basin sites indicate that release of bromide and ammonium are strongly correlated and may be indicative of a relationship between the processes controlling debromination and ammonium production at these sites.

The six-hour UV photo-oxidation treatment was successful in complete dehalogenation of the 4-bromophenol and dibromoacetic acid standards, with 101.4% and 102.6% recovery as bromide ion in solution, respectively. This experiment demonstrates that the method is effective for release of bromide from dissolved organobromine compounds (Figure 2.3). The total dissolved bromine concentrations of pore water from Costa Rica margin Site U1412A obtained via the UV oxidation treatment process are compared to pore water bromide concentrations measured prior to UV treatment (Figure 2.4). This comparison is to detect any significant concentrations of dissolved organobromine compounds that could indicate any zones of suppression of the dehalogenation process, affecting the interpretation of the pore water profiles. Concentrations of total dissolved bromine are not significantly different from bromide concentrations in Costa Rica margin Site U1412A pore waters. These shorebased results are also compared with shipboard bromide measurements to verify that no significant dehalogenation of dissolved organohalides occurred during sample storage. The shore-based bromide data show a slight negative offset from the shipboard bromide data, likely from differences in instrument

calibrations. These data indicate that the concentrations of any dissolved organobromines are within the analytical error (<20 μM Br) throughout the sediment column and thus do not significantly affect the shape of the total dissolved bromine concentration profile at this scale, and do not indicate any zones where the rate of hydrolysis of solid-phase organics is greater than the rate of debromination. These results are consistent with incubation experiments that have measured microbially-mediated debromination rates in anoxic sediment slurries spiked with polybrominated diphenyl ethers (Tokarz et al., 2008; Zhu et al., 2014). In these experiments, the half-lives of free and adsorbed organobromine concentrations were a few months to a few decades. These timescales for debromination are very short compared with rates of natural organic matter fermentation in anoxic deep marine sediments.

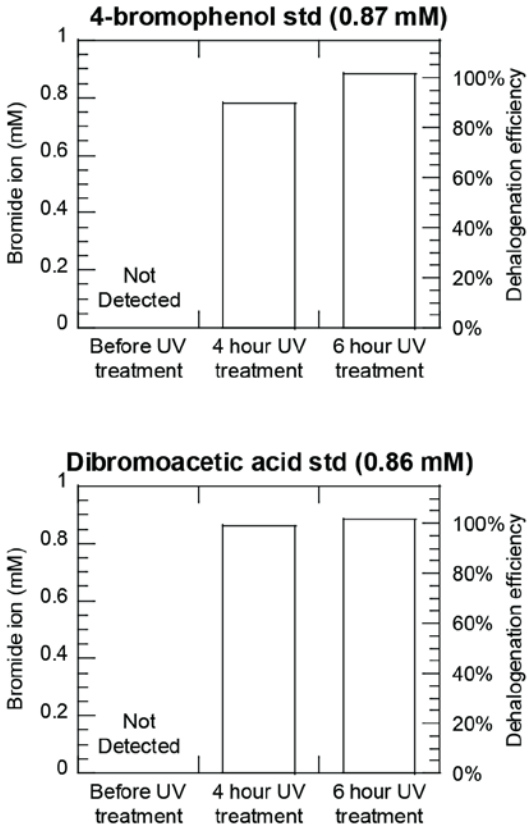

Figure 2.3. Results from measurements of bromide ion concentration in standard solutions of 4-bromophenol and dibromoacetic acid before laboratory ultraviolet treatment, after 4 hours of treatment, and after 6 hours of treatment. Average bromide yields after 6 hours of treatment are 101.4% for the dibromoacetic acid solution and 102.6% for the 4-bromophenol solution. Relative standard deviations of Br^- concentrations from multiple runs range between 0.3% and 0.5%.

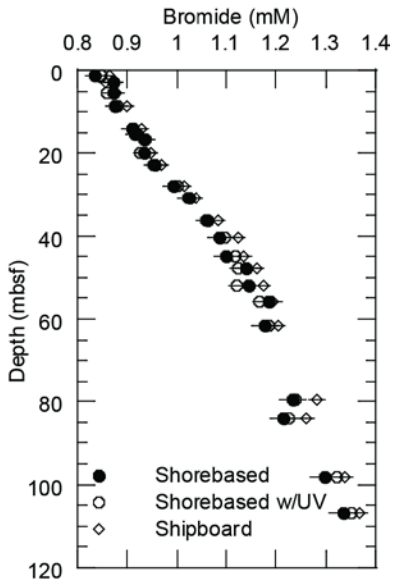

Figure 2.4. Results of UV oxidation experiments on Costa Rica margin Site U1412A pore water samples. Pore water concentration profiles of bromide from shipboard analyses, shore-based analysis prior to UV treatment, and after UV treatment are shown. A slight offset from shipboard and shore-based bromide data is likely due to differences in instrument calibration. Error bars of 2% are shown for shipboard measurements, and 1% for shore-based measurements.

Solid-phase bromine profiles from IODP Expedition 344 Site U1412A, and K-G basin Sites 14A and 20A suggest relatively rapid debromination in the upper sediment column, followed by more gradual loss of bromine in the lower sediments (Figure 2.5). Scatter and peaks in the profiles indicate that the burial and degradation rates of organobromines are not constant through time at these sites. At K-G basin Sites 14A and 20A, the solid-phase bromine concentrations that are within the recent mass transport deposits in the upper sections of the sediment column exhibit high variation. The maximum Br:OC molar ratios in the upper sections of K-G basin Sites 14A and 20A, and Costa Rica Site 1412A are listed in Table 2.2. The average Br:OC molar ratio in marine-sourced organic matter is $9x10^{-4}$ to $1.8x10^{-3}$, and the average Br:OC molar ratio in terrestrial organic matter is $6x10^{-5}$ to $3x10^{-4}$ (Leri et al., 2010; Mayer et al., 1981; Mayer et al., 2007; Mun and Bazilevich, 1962; Price and Calvert, 1977; Price et al., 1970). The Br:OC molar ratios of the most recently deposited material are consistent with hemipelagic

sedimentation, with organic matter from a combination of marine and terrestrial sources. The Br:OC molar ratios from the K-G basin Sites 14A and 20A are smaller than those found at Costa Rica Site U1412A, reflecting the dominantly terrestrial source of organic matter to the K-G basin, while the greater Br:OC molar ratios from Costa Rica Site U1412A suggests a greater fraction of sedimentary organic matter is contributed from marine sources.

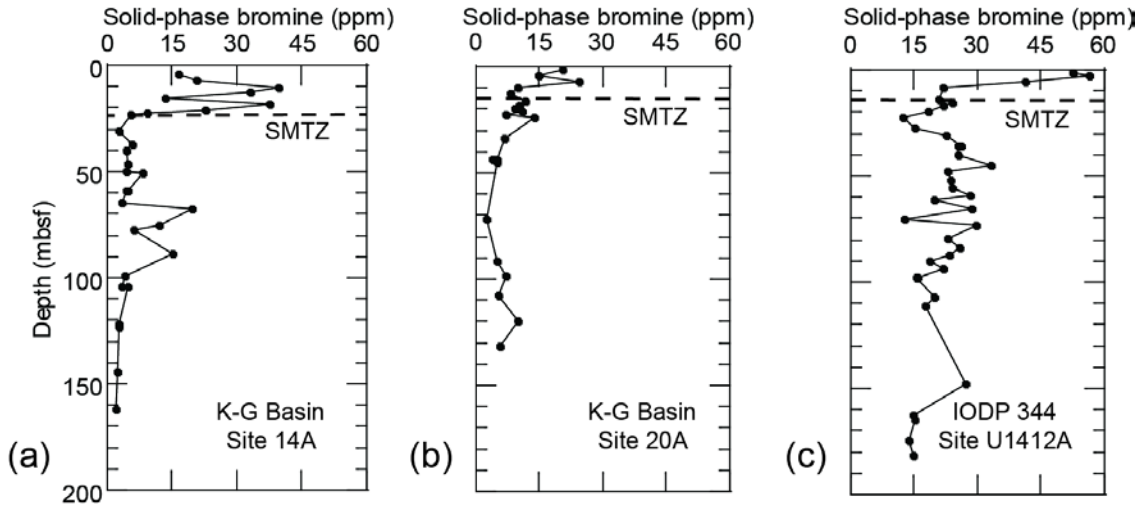

Figure 2.5. Solid-phase bromine concentration profiles at A) K-G basin Site 14A, B) K-G basin Site 20A, and C) Costa Rica Site U1412A. The dashed lines mark the depth of the sulfate-methane transition zone (SMTZ) at each site (Harris et al., 2013).

Table 2.2. Maximum bromine concentrations near the top of the sediment column at each site, representing the most recently deposited organic material, and the corresponding Br:OC molar ratios based on the nearest total organic carbon measurements.

Site	Maximum bromine concentration (ppm)	Total organic carbon (wt%)	Maximum approximate Br:OC molar ratio
U1412A	56.3 @ 2.9 mbsf	1.8 @ 2.8 mbsf	4.7×10^{-4}
14A	39.8 @ 10.4 mbsf	1.9 @ 8.1 mbsf	3.1×10^{-4}
20A	24.2 @ 7 mbsf	1.3 @ 10.7 mbsf	2.8×10^{-4}

The model results for the steady-state sites that are not significantly affected by recent mass transport deposits, from Costa Rica Site U1412A and U1378B, Cascadia Site U1325B/C, and Nankai Site C0008A are presented in Figure 2.6. The K-G basin sites, affected by recent

mass transport deposits, were omitted from the reaction rate modeling due to the non-steady-state bromide profiles in those sections (Hong et al., 2014). Debromination rates decrease downward, eventually decreasing to values nearly indistinguishable from zero, within the 1σ uncertainty envelope, in the lower sediment column at depths ranging between 50 and 350 mbsf. The very low debromination rates in the lower sections of the rate profiles suggest that depths considered in this study are representative of the bulk of debromination activity in the sediment column during early diagenesis.

The modeled rates of debromination are consistent with the observed decrease in solid-phase bromine with depth at Costa Rica Site U1412A. Variable rates of organobromine burial and sedimentation through time will cause deviations between modeled debromination rates and measured solid-phase bromine concentration profiles. At Costa Rica Site U1412, the long-term average sedimentation rate is estimated to be 5 – 10 cm/ky, with large variations over the past ~2 My (Harris et al., 2013). However, these long-term sedimentation rates are not well constrained, which adds additional uncertainty to calculated rates of debromination. The magnitude of reaction rates calculated using any model are highly dependent on sedimentation rate history, with sedimentation rate being a primary control on pore water burial rate and loss of reaction products to overlying bottom water. For these reasons, ranges of integrated reaction rates are shown in Table 2.3, with the ranges corresponding to the rates derived using the ranges in sedimentation rate estimates from each site. The reaction rate profiles in Figure 2.6 are calculated using a mid-range value of the estimated sedimentation rates.

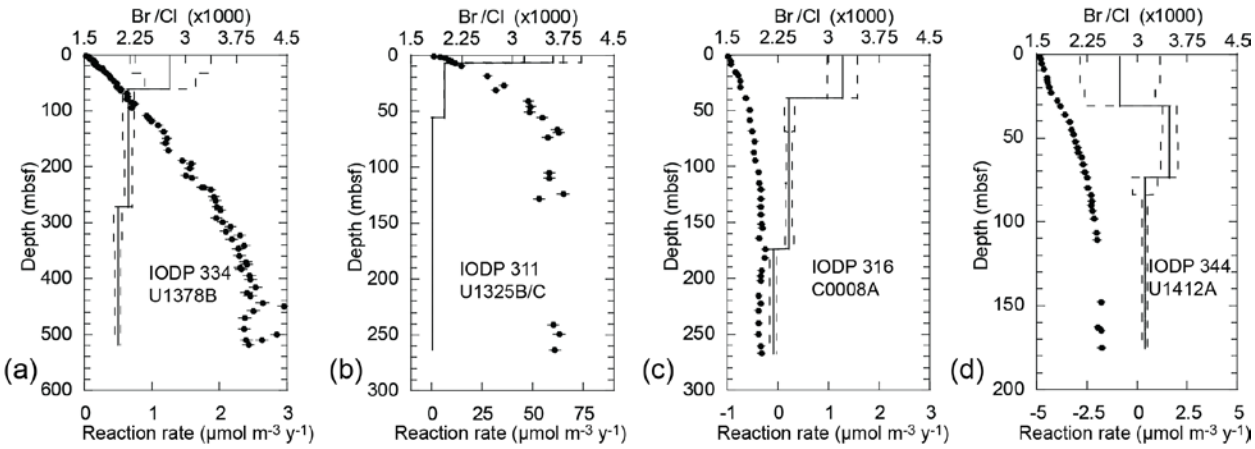

Figure 2.6. Pore water profiles of bromide/chloride molar ratios and modeled debromination rates for A) Costa Rica Site U1378B, B) Cascadia Site U1325B/C, C) Nankai Site C0008A, and D) Costa Rica margin Site U1412A. In the reaction rate profiles, solid lines show dissolved bromide production/consumption rates and dashed lines are the 1σ uncertainty envelope. Cascadia and Nankai data from (Fehn et al., 2006; Kinoshita et al., 2009b). Note the change in scale for the depths and reaction rates at each site.

Table 2.3. Ranges of integrated bromide fluxes from IODP Site U1325, IODP 316 Site C0008, and IODP 334 Site U1412. Integrated bromide fluxes are calculated as the depth-integrated average net bromine production rates for the entire sampling depth range. Ranges are based on the ranges in estimated sedimentation rates at each site.

Site	Integrated Flux (μmol m^{-2} y^{-1})	Sedimentation rate range (cm ky^{-1})
U1325B/C (Cascadia)	600 – 910	20 – 80
C0008A (Nankai)	63 – 78	5 – 20
U1412A (Costa Rica)	77 – 93	5 – 10
U1378B (Costa Rica)	270 – 450	24 – 52

2.4 DISCUSSION

The small bromide concentration gradients within the sulfate reduction zone at the K-G basin sites with a larger gradient below would imply either upward flux of bromide into a geochemical sink within the upper sediments, or non-steady-state pore water burial. Recent sedimentation rate estimates based on kinetic modeling of the pore water sulfate and ammonium concentration

profiles in the K-G basin indicate that the top 8 – 25 meters of the sediment was deposited in the past 300 – 1600 years (Hong et al., 2014). The recent, abrupt emplacement of mass transport deposits has not allowed enough time for accumulation of bromide in the pore waters within this zone, or for diffusion of bromide to bring the pore water profiles back to steady-state (Hong et al., 2014; Mazumdar et al., 2009; Mazumdar et al., 2012; Ramprasad et al., 2011; Solomon et al., 2014). In addition, no significant geochemical sinks for bromide in anoxic sediments are known. Studies have shown that bromide is not removed from solution during authigenic carbonate precipitation in amounts great enough to affect our pore water concentration measurements (Okumura et al., 1986), and pore water bromide concentrations do not decrease below seawater concentrations at any of the sites studied. Hence, much of the bromine that is released from organic matter by debromination is eventually transported through diffusion and/or advection back into the overlying ocean. Our total dissolved bromide measurements (Figure 2.4) indicate that bromine does not accumulate in solution as dissolved organobromine compounds at concentrations that would affect our modeled rates of debromination and does not indicate any zones where the rate of hydrolysis of solid-phase organics is greater than the rate of debromination of dissolved organobromines.

Between 30 and 80 mbsf at the K-G basin sites the pore water bromide concentration gradient abruptly decreases, with a much slower increase in bromide concentration with depth (Figure 2.3a – d). Pore water ammonium concentration profiles exhibit a similar abrupt decrease in gradient at the same depths. The distinct decrease in the concentration gradient of pore water bromide and ammonium within the methanogenic zone of the K-G basin profiles are not explained by known sedimentary processes or physical properties at those sites. Several qualitative factors were investigated as potential controlling influences on the gradient change in

the bromide and ammonium profiles, including temperature, pressure, age of sediments, potential fracture zones, and changes in lithology or sediment physical properties. No correlations were found between these factors and the location of the gradient change within the sediment column. In addition, organohalogen respiration has a much lower hydrogen concentration threshold than methanogenesis, suggesting that the supply of electron donors is not a limiting factor for the process within the methanogenic zone (Löffler et al., 1999; Luijten et al., 2004). However, measurements of total solid-phase bromine concentration from K-G basin Sites 14A and 20A, and Costa Rica margin Site U1412A indicate that the very low bromide production rates below the bromide and ammonium concentration gradient change is likely due in part to a depleted pool of organobromine substrate. These high-resolution data from K-G basin Sites 14A and 20A, and Costa Rica margin Site U1412A are consistent with previous results from the Peru margin, which showed decreasing total solid-phase bromine concentrations with depth at that margin (Martin et al., 1993). With depletion of the pool of brominated organic molecules, less substrate remains to be dehalogenated in addition to the pool becoming more refractory and less bioavailable. However, solid-phase bromine concentrations remain above 2 ppm at Sites 14A and 20A, and above 12 ppm at Site U1412A, and zones of higher solid-phase bromine abundance are present at various depths at all three measured sites. These results indicate that depletion of the organobromine substrate is not the only limiting factor for rates of debromination. Other potential factors include alteration of the organohalide pool into more refractory, less bioavailable organic molecules, and changes in microbial activity and dynamics in the sediment column.

Though previous studies have shown that pore water concentrations of bromide and ammonium typically increase with depth as organic matter degradation proceeds, the data from

K-G basin Sites 5, 14, 15, and 20 demonstrate a much closer relationship between the distribution of debromination and ammonium production activity than has been previously recognized. This suggests that the processes of debromination and ammonium production are likely closely linked at least within the methanogenic zone. Although over 1600 naturally-occurring organobromines have been identified to date, the structures and identities of the compounds that are associated with the organobromine pool in deep marine sediments have not been well characterized (Gribble, 1999). However, in estuary sediments and marine infauna, natural organobromine compounds have been shown to be commonly associated with the amino acid fraction of organic matter (Bowen, 1966; Fielman et al., 1999; Harvey, 1980; Upstill-Goddard and Elderfield, 1988). This same association may also be present in deep marine sediments, which would explain the correlation between debromination and ammonium production at these sites, and suggests that the debromination is related to degradation of the bioavailable nitrogen pool. Once the pool of bioavailable nitrogen and associated organobromines is depleted, ammonium production and dehalogenation decrease significantly or cease altogether.

With the wide variation in bromine and nitrogen concentrations between terrestrially-sourced and marine-sourced organic matter, the forms of bioavailable organobromine and nitrogen compounds may vary by source as well. The sediment and associated organic matter supplied to the K-G basin is largely terrestrially-sourced and pre-aged from the Krishna and Godavari Rivers. The close correlation between the bromide and ammonium profiles from the K-G basin may be associated with the terrestrially-sourced organic matter at these sites, with different pools of bioavailable organobromines and nitrogen compounds in marine-sourced organics altering this relationship at other sites. An association between ammonium production

and debromination in terrestrially-derived organics would provide a useful tracer for the degradation rates of a large proportion of the bioavailable pool of nitrogen-rich organics in the sediment column at margins with high terrestrial input such as the K-G basin. Similar bromide and ammonium profiles observed at other margin locations suggest it would be more widely applicable.

Though the specific compounds being debrominated in the sediments are not known, the change in Gibb's free energy (ΔG^0) values for reductive debromination of common organobromines have been calculated to range from between -150 to -190 kJ/mol, approximately 2 – 3 times higher than sulfate reduction or methanogenesis (Dolfing, 2003). However, even with high per-mole energy yields, the low concentrations and correspondingly low debromination rates of organobromines in the sediment column limit the maximum metabolic energy that could be provided by this process. Maximum rates of debromination, integrated over the entire measured sediment column, are on the order of 10^1 to 10^3 μmol m^{-2} y^{-1} (Table 2.3), approximately 2 orders of magnitude lower than sulfate reduction, which is closer to 10^4 - 10^5 μmol m^{-2} y^{-1} in continental margin environments (Bowles et al., 2014; D'Hondt et al., 2004; D'Hondt et al., 2002), and several orders of magnitude lower than depth-integrated methanogenesis rates, which have been estimated between 10^4 – 10^8 μmol m^{-2} y^{-1} (Colwell et al., 2004; Colwell et al., 2008). The rates of debromination presented in Figure 2.6 and Table 2.3 provide an upper estimate for the rates of organobromine respiration at these locations. Though putative dehalogenating bacteria are found to be abundant groups at several continental margin locations (Biddle et al., 2008; Futagami et al., 2013; Inagaki et al., 2006; Martino et al., 2013), these results demonstrate that the maximum total amount of energy produced through

organobromine respiration is small in comparison to other metabolic pathways occurring throughout the sediment column in the continental margin environment.

Additional halogenated substrate is available in continental margin sediments in the form of naturally chlorinated and iodinated organic matter. The ΔG^0 for reductive dehalogenation of chlorinated and iodinated organic compounds are similar to those for brominated organics (Dolfing, 2003). Thus, dehalogenation of organochlorines and organoiodines could provide additional energy to dehalogenating bacteria in the deep biosphere. Natural abundances of organochlorines in marine organic matter have been measured in sediment trap samples from the Arabian Sea, and were found to be approximately 1.7×10^{-3} to 2.7×10^{-3} mol Cl/mol C (Leri et al., 2015). This abundance is slightly greater than the typical molar ratios of organobromine in marine organic matter of 0.9×10^{-3} to 1.8×10^{-3} mol Br/mol C (Leri et al.; Mayer et al., 1981; Price and Calvert, 1977; Price et al., 1970), and so the total magnitude of dechlorination would be expected to be higher than, though on the same order as, debromination. The increases of 1 – 2 mM in pore water Br^- concentrations are easily measured, because they translate to a ~120 – 240% increase in pore water Br^-. However, a 1 – 2 mM increase in Cl^- translates to just a 0.2 – 0.4% increase in pore water Cl^-, which is within the ~0.2 – 0.5% error of pore water Cl^- measurements. In addition, variations in pore water chloride concentrations from the Costa Rica, Nankai, Cascadia, and Indian margins are greater than the 1 – 2 mM increase that would be expected from dechlorination of the organic matter (Collett et al., 2008; Fehn et al., 2006; Harris et al., 2013; Kinoshita et al., 2009b; Solomon et al., 2014; Vannucchi et al., 2010). These greater variations indicate that pore water chloride concentrations are dominated by other processes, such as hydrous mineral formation, gas hydrate formation and dissociation, and burial of seawater through glacial/interglacial cycles. Due to the overprinting of these additional

processes, the rates of dechlorination are difficult to evaluate through pore water analysis at these locations. Though the concentration of iodinated organic compounds is controlled by redox processes in the upper centimeters of continental margin sediments, pore water iodide concentrations measured in continental margin sites typically increase by approximately the same order of magnitude as pore water bromide (Fehn et al., 2006; Harvey, 1980; You et al., 1993). The similar increase in iodide concentrations suggests similar integrated rates of dehalogenation of organoiodines as organobromines.

The solid-phase bromine profiles and model results based on pore water bromide profiles indicate that the highest rates of debromination occur in the upper sediment column, primarily within the sulfate reduction zone. If the observed debromination at the margin sites in our study is microbially-mediated, the most active zone of microbial debromination is in the upper sediment column within the sulfate reduction zone. This activity would indicate that the debromination pathway in these zones is not limited by inhibition by sulfur oxyanions, or competition with sulfate reduction or other redox processes as has been previously observed in laboratory experiments (Aulenta et al., 2008; Colberg, 1990; Townsend and Suflita, 1997). However, the geochemical approach used in this paper quantifies the total rate of debromination in the sediments, and cannot distinguish organobromine respiration from other potential debromination pathways such as cometabolic processes or abiotic reactions.

Genomic and metagenomics analyses of microbial communities at Costa Rica and other margins have identified abundant putative dehalogenating microbes and reductive dehalogenase genes throughout the sediment column (Biddle et al., 2008; Futagami et al., 2013; Inagaki et al., 2006; Martino et al., 2013). The low rates of debromination in the lower sediment column at these sites, indistinguishable from zero within the 1σ uncertainty envelope of the model, are

consistent with recent genomic sequencing of bacteria from the phylum Chloroflexi, which has shown that these bacteria may have a wide range of metabolic pathways and are not dependent on organohalide respiration for energy (Kaster et al., 2014; Wasmund et al., 2013).

2.5 CONCLUSIONS

Organohalide respiration has been hypothesized to be widely active in the deep biosphere. We provide an upper limit constraint on the rates of organobromine respiration by numerically modeling the total production rate of dissolved bromide with depth in pore water sampled at several continental margins. Pore water concentrations of bromide typically increase with depth in the upper sections of the sediment column, with a slower rate of increase with depth where solid-phase bromine concentrations are lower. As a result, the modeled bromide production rates indicate that the rates of bromide production decrease with depth, decreasing to near zero where solid phase bromine concentrations reach a minimum. This modeling approach quantifies the total rate of debromination from all potential pathways, including organobromine respiration, fermentation, fortuitous debromination through co-metabolic processes or direct cofactor catalysis, and abiotic reaction, thus providing an upper limit to any of these pathways. Our results indicate that the maximum integrated rates of organobromine respiration in the sediment column are at least an order of magnitude lower than sulfate reduction and several orders of magnitude lower than methanogenesis. These results are consistent with a wide distribution of organohalide respiration activity in continental margin sediments geographically and with depth, and the low integrated rates do not rule out debromination as a viable metabolic pathway for microbes in the deep biosphere. Rates of dehalogenation of chlorinated and iodinated organic

compounds were not quantified in this study, but these pathways may provide additional energy to dehalogenating microbes in the deep biosphere.

Pore water concentration profiles of bromide and ammonium from the Krishna-Godavari basin on the southeastern margin of India exhibit the best example to date of the correlation between debromination and ammonium production in continental margin sediments. With additional research into the nature of sedimentary organobromines and the association between these and bulk sedimentary organic matter, modeled rates of debromination may potentially be used as a conservative tracer to track the degradation of a significant portion of the organic carbon and nitrogen pools in continental margin sediments.

Chapter 3. THE ROLE OF MARINE SEDIMENTS IN THE MODERN OCEANIC MAGNESIUM CYCLE

ABSTRACT

Major element cycles in the ocean are driven by physical and biological processes acting over geologic timescales. The oceanic magnesium cycle has been of interest for its connection to continental weathering and formation of aluminosilicate and carbonate minerals, which are intimately linked to the long-term climate on Earth. Uncertainties in the oceanic magnesium cycle propagate into other chemical budgets such as carbon and calcium, and into interpretations of paleo-oceanographic reconstructions of seawater δ^{26}Mg and Mg/Ca ratios. Here, we produce a detailed global map of the diffusive and burial flux of dissolved magnesium across the sediment-water interface, quantify the global flux of magnesium from the ocean into marine sediments, and model the isotopic fractionation associated with those fluxes using data from a variety of ocean drilling locations. We find that the magnesium flux into marine sediments accounts for about 15 – 20% of the magnesium sink from the ocean, with a flux-weighted fractionation factor of approximately 0.9997 acting to increase the magnesium isotopic ratio in the ocean. Our analysis of global magnesium fluxes and isotopic fractionation provides the best constraints to date on the sources and sinks that define the oceanic magnesium cycle, including new constraints on the loss of magnesium during low-temperature ridge flank hydrothermal circulation.

3.1 INTRODUCTION

The oceanic magnesium cycle is primarily a balance between weathering on land, high- and low-temperature hydrothermal alteration of the basaltic oceanic lithosphere, and formation of

sedimentary carbonates and aluminosilicates (Broecker and Clark, 2009; Drever et al., 1988; Dzhamalov and Safronova, 2002; Gothmann et al., 2017; Higgins and Schrag, 2012; Immenhauser et al., 2010; Liu et al., 2017; Milliman, 1993; Mottl and Wheat, 1994; Pogge von Strandmann, 2008; Pogge von Strandmann et al., 2014; Snow and Dick, 1995; Tipper et al., 2006; Wilkinson and Algeo, 1989; Wimpenny et al., 2014; Wombacher et al., 2011). Because these processes are also major drivers of long-term carbon dynamics and affect many other element cycles in the ocean, paleo-oceanographic reconstructions of the magnesium cycle can provide information about long-term climate and element cycling in the ocean. Fluctuations in Mg/Ca ratios of sedimentary carbonates reflect oscillations between "hot-house" and "ice-house" conditions, and the evolution of magnesium isotope ratios in the ocean have been interpreted as recording changes in silicate weathering on land and in the oceanic crust (Gothmann et al., 2017; Higgins and Schrag, 2015; Lea, 2003; Pogge von Strandmann et al., 2014). Models that use paleo-oceanographic reconstructions of proxies such as Mg/Ca or δ^{26}Mg rely on knowledge of the modern-day magnesium cycle to use as a benchmark for quantification of the changes in the past. However, large uncertainties in the modern-day magnitudes propagate uncertainty into interpretations of past changes. By better defining the magnitude of the current sources and sinks of magnesium in the modern ocean, the changes in those sources and sinks through geologic time can be more accurately included in models that explore the dynamics of the Mg/Ca ratio and δ^{26}Mg in the ocean.

Magnesium interacts with major geochemical cycles such as the carbon and calcium cycles during the formation of authigenic carbonates and aluminosilicates (Drever et al., 1988). Authigenic carbonates, which form *in situ* within marine sediments during burial and diagenesis, typically have high magnesium contents due to the high Mg/Ca ratio and often low inhibitory

sulfate concentrations in pore water (Baker and Kastner, 1981; Loyd and Berelson, 2016; Matter et al., 1975; Mavromatis et al., 2014; Snyder et al., 2007). Authigenic carbonate precipitation tends to occur to a greater extent near continental margins, where burial of organic matter is greatest, and rates of alkalinity production are higher from organic matter degradation, sulfate reduction, and anaerobic oxidation of methane. In addition to precipitation of primary authigenic carbonate, magnesium may be depleted in pore waters during the recrystallization of low-magnesium biogenic carbonate to higher-magnesium authigenic calcite or dolomite (Chanda and Fantle, 2017; Fantle and Higgins, 2014; Higgins and Schrag, 2012; Matter et al., 1975). Authigenic aluminosilicate formation is also a potentially important sink for magnesium in marine sediments, where it can be incorporated into the authigenic phase in a greater stoichiometric ratio than in the original primary silicate from which it formed, resulting in the release of calcium and other cations to pore waters (Gieskes and Lawrence, 1981). Many authigenic aluminosilicate formation reactions occur in marine sediments, but in all of these reactions, the products are primarily cation-rich clays with high surface areas and high cation exchange capacities (Gieskes and Lawrence, 1981; Kastner, 1981; Michalopoulos and Aller, 1995; Solomon et al., 2014; Wallmann et al., 2008). Formation of these minerals typically results in the net uptake of magnesium from pore waters, with the magnitude of uptake dependent on the specific mineral or glass compositions involved in the reaction. Because these mineral formation and alteration reactions involve carbon and other major elements, variations in the amount of authigenic carbonate and aluminosilicate formation through time affect the long-term carbon cycle and other element cycles.

The global flux of magnesium into marine sediments has been demonstrated to be a potentially important part of the oceanic magnesium cycle (Anderson et al., 2014; Sayles, 1979;

Sun et al., 2016). In addition, measured fractionations of magnesium isotopes in marine pore waters are large enough to significantly affect the oceanic magnesium isotope ratio over time periods of millions of years through exchange with the overlying ocean (Gothmann et al., 2017; Higgins and Schrag, 2010, 2012). The flux into marine sediments from the overlying ocean is typically driven by molecular diffusion that occurs as pore water magnesium is depleted during authigenic mineral formation, as well as direct pore water burial that results from sediment accumulation on the seafloor. Depletion of magnesium in marine pore waters is nearly ubiquitously observed in pore water concentration profiles from scientific ocean drilling, exhibiting a clear sedimentary sink for magnesium, particularly in continental margin environments. Depletion in the pore waters is accompanied by variations in the isotopic ratio of $^{26}Mg/^{24}Mg$. These isotopic variations reflect the balance between formation of isotopically-light carbonates and isotopically-heavy aluminosilicates in the sediment column. Pore water concentration profiles from most environments exhibit no net release of magnesium at greater depths, indicating a stable sedimentary sink for magnesium. However, in some localized regions of the ocean, other processes may cause magnesium to flux from pore waters into the overlying ocean, such as high-magnesium mineral dissolution or diffusion from relict brine and evaporite deposits (Wallmann et al., 2008; Warren, 2010).

Here, we calculate the magnitude and distribution of magnesium fluxes into marine sediments from the overlying ocean using available scientific ocean drilling data from 1968 – 2015. Fluxes are calculated considering both pore water burial and molecular diffusion at 269 ocean drilling sites from a wide-variety of margin and abyssal environments (Figure 3.1a). The magnesium flux associated with pore water burial is a significant component of the total magnesium flux at most locations (Figure 3.1c). Fluxes at the 269 sites range from -0.03 to 33.8

mmol m^{-2} y^{-1}, with a median value of 2.6 mmol m^{-2} y^{-1} (See Table B2). Positive values represent a flux from the ocean into the seafloor. Monte Carlo simulation is conducted to estimate the total uncertainty of the flux at each site, with a median uncertainty of 0.9 mmol m^{-2} y^{-1}.

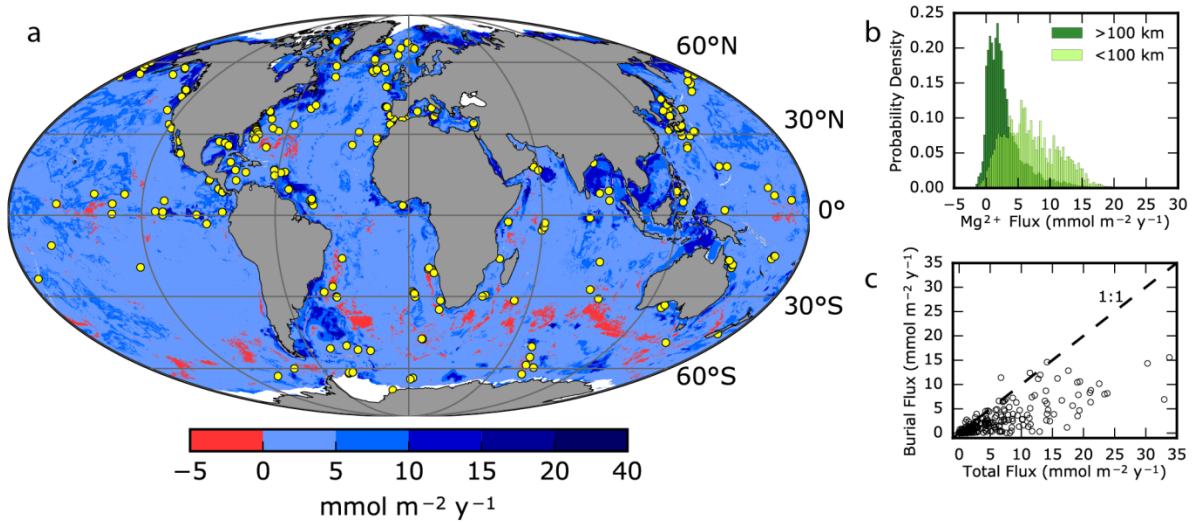

Figure 3.1. Global magnesium fluxes into marine sediments. a) Global distribution of net magnesium fluxes into marine sediments (millimoles per square meter per year); positive values are from the ocean into the seafloor; dots are the individual ocean drilling sites with measured fluxes. b) Histogram showing the distribution of net magnesium fluxes near (<100 km) and farther away (>100 km) from the continental margins. c) Comparison of the magnitude of the net magnesium fluxes at each location versus the flux associated with pore water burial.

3.2 METHODS

3.2.1 *Data Sources*

Fluxes of magnesium across the sediment-water interface were calculated using available data from the National Geophysical Data Center (https://www.ngdc.noaa.gov/mgg/geology/dsdp), Janus (http://www-odp.tamu.edu/database), LIMS (http://web.iodp.tamu.edu/LORE), and J-CORES (http://sio7.jamstec.go.jp) databases that house drilling data from the Deep Sea Drilling Project (DSDP), ODP, and IODP. Additional data were compiled from the Indian National Gas Hydrate Program (NGHP) Expedition 01 (Collett et al., 2008). This compiled dataset includes

data collected with both the JOIDES Resolution and D/V CHIKYU. Only sites with high-quality data were used, limiting the sites to those with at least three pore fluid magnesium concentration measurements in the upper sediment column that form a gradient to the ocean bottom-water concentration at the sediment-water interface, and are not affected by unquantified advection of pore water or sample collection artifacts due to gas hydrate dissociation.

3.2.2 *Solute Flux Calculations*

Fluxes at individual sites are calculated accounting for molecular diffusion and pore water burial using the 1-dimensional advection diffusion equation in porous media:

$$J = -\varphi_0 D_s \frac{dC}{dz} + b_0 C_0$$

where J is the flux across the sediment-water interface. φ_0 is the porosity of the surface sediment found using the best fit of Athy's Law to the measured porosity profile. dC/dz is the concentration gradient (mol m^{-4}) at the sediment-water interface found using an exponential fit to the uppermost four or more measurements. C_0 is the magnesium concentration (mol m^{-3}) at the sediment-water interface.

D_s is the effective sedimentary diffusion coefficient (m^2 y^{-1}), accounting for sediment tortuosity with the relationship (Boudreau, 1996): $D_s = D_{sw}/(1-\ln(\varphi^2))$, where D_{sw} is the molecular diffusion coefficient in sea water corrected for bottom water temperatures from the World Ocean Atlas using the Stokes-Einstein equation (Locarnini et al., 2013).

The term b_0 is the volumetric pore water burial flux (m^3 y^{-1}) accounting for sediment compaction using the relationship:

$$b_0 = \frac{\varphi_L(1-\varphi_0)}{(1-\varphi_L)} s$$

where φ_L is the sediment porosity at depth where compaction of the sediment column becomes negligible, and s is the sedimentation rate found using a piecewise linear regression of the biostratigraphic data for each site. Monte Carlo simulation was used to estimate the standard deviations of each net magnesium flux based on the known uncertainty in the concentrations, porosities, and pore water burial rates.

3.2.3 *Regression Model*

Net magnesium fluxes at individual sites were used as a training dataset to predict the global distribution of magnesium fluxes across the sediment-water interface using the gradient-boosting regression technique in the scikit-learn Python package (Pedregosa et al., 2011). The supervised machine learning algorithm fits a decision tree model to the training data, and then sequentially fits a new decision tree to the residuals from the prior model fit for a specified number of iterations. The branching of the decision tree is based on the splits in other environmental parameters, or features, that effect the greatest reduction in variance in the training data associated with each branch. The models are then combined to find the best possible multidimensional fit of the training data to the other environmental parameters. Globally-gridded datasets of those environmental parameters are then used to predict the global distribution of magnesium fluxes.

The globally-gridded features used in the regression models are listed in Table 3.1. The data are all resampled to 5-minute cell-registered grids using the Rasterio Python package. For sedimentation rate, long-term average sedimentation rate is calculated, as in Burwitcz and Wallmann, (2011), where sediment thickness in each grid cell is divided by the underlying

crustal age. For sediment thicknesses, the Whittaker (2013) dataset is used where available, with the Laske and Masters, (1997) dataset being used where needed.

Table 3.1. Globally-gridded predictor datasets used in magnesium flux regression models

Dataset	Reference	Source	Original grid resolution
Global relief (water depth)	(Amante and Eakins, 2009)	https://www.ngdc.noaa.gov/mgg/global/global.html	1 min
Surface sediment porosity	(Martin et al., 2015)	http://onlinelibrary.wiley.com.offcampus.lib.washington.edu/doi/10.1002/2015GL065279/abstract	5 min
Surface productivity	(Martin et al., 2015)	http://onlinelibrary.wiley.com.offcampus.lib.washington.edu/doi/10.1002/2015GL065279/abstract	5 min
Sedimentation rate	(Whittaker et al., 2013) (Burwicz et al., 2011; Laske, 1997; Müller et al., 2008)	Calculated from sediment thickness and crustal ages	5 min
Bottom water temperature	(Locarnini et al., 2013)	https://www.nodc.noaa.gov/OC5/woa13/	0.25 deg

3.2.4 *Regression model parameters and cross-validation results*

Cross-validation is used to evaluate the accuracy of the regression, and to compare it to other potential methods. See Tables 3.2 – 3.4 for the model parameters and Figures 3.2 – 3.4 for the cross-validation analyses. Three regression methods were compared using Leave-One-Out cross-validation to determine which method was best suited to the ocean drilling dataset. While the gradient-boosting regressor and random forest techniques provide similar predictive power, the gradient-boosting regression technique provides both the best predictive power, and is the most robust option to avoid over-fitting the model to training data, as indicated by the greater number of samples per leaf. The best-fit parameters for each method are listed below, along with the results of the cross-validation analysis. For gradient-boosting regression and random forest, the feature importances are listed, which are a measure of how much each feature reduces the variance of the model fit. For the multiple linear regression technique, the linear coefficients are listed.

Table 3.2. Gradient boosting regression parameters and results

Model parameters	
Loss function	least squares regression
Boosting stages	200
Learning rate	0.1
Minimum samples per leaf	9
Quality of split criterion	Friedman mean-squared error
Feature importances	
Sedimentation rate	0.286
Surface sediment porosity	0.260
Bottom water temperature	0.172
Water depth	0.148
Surface ocean productivity	0.135
Results	
Coefficient of determination	0.535
Global Mg flux (Tmol y^{-1})	1.07

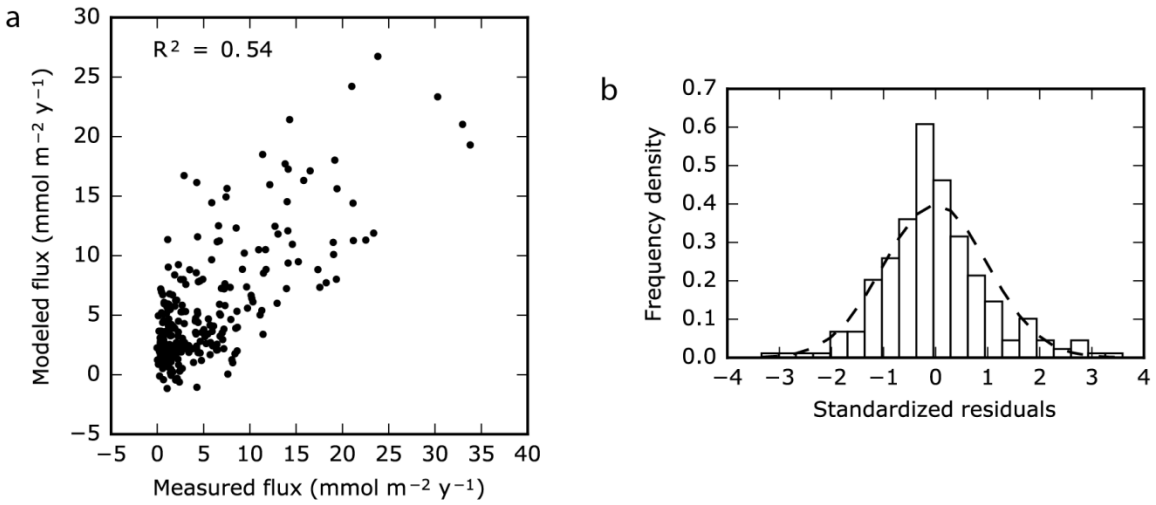

Figure 3.2. A) Measured magnesium flux values vs. model results via leave-one-out cross-validation, using the gradient boosting regression technique with the parameters listed in Table 3.2. B) Histogram of standardized residuals of the cross-validation, with the dashed line showing an idealized normal distribution.

Table 3.3. Random forest regression parameters and results

Model parameters	
Number of trees	200
Minimum samples per leaf	3
Quality of split criterion	Friedman mean-squared error
Feature importances	
Sedimentation rate	0.488
Water depth	0.163
Surface ocean productivity	0.123
Bottom water temperature	0.119
Surface sediment porosity	0.107
Results	
Coefficient of determination	0.512
Global Mg flux (Tmol y^{-1})	1.08

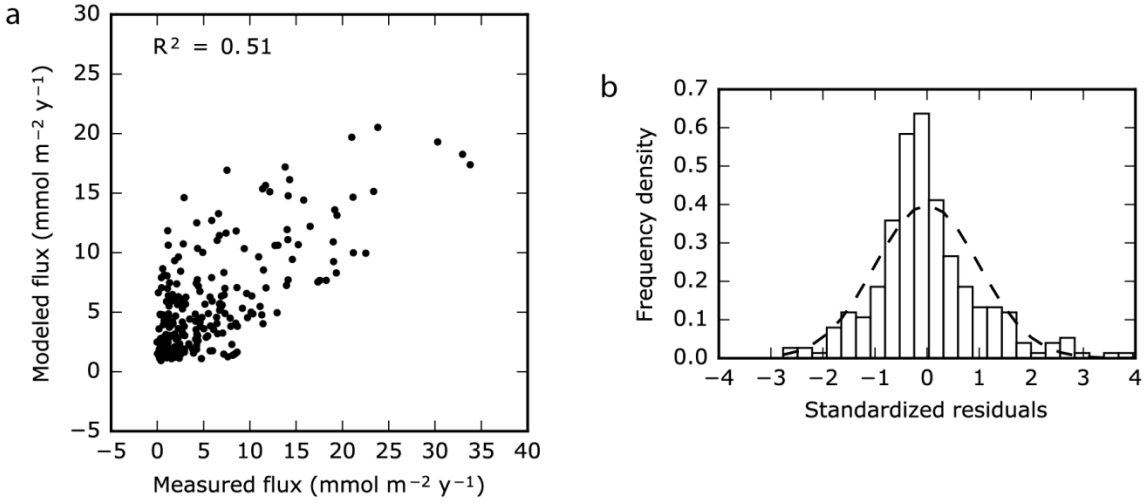

Figure 3.3 A) Measured magnesium flux values vs. model results via leave-one-out cross-validation, using the random forest regression technique with the parameters listed in Table 3.3. B) Histogram of standardized residuals of the cross-validation, with the dashed line showing an idealized normal distribution.

Table 3.4. Multiple linear regression parameters and results

Model parameters	
Data normalized	yes
Intercept used	yes
Feature importances	
Sedimentation rate	5.524E+01
Surface sediment porosity	-1.728E-04
Bottom water temperature	6.162E-05
Water depth	5.814E-08
Surface ocean productivity	2.607E-09
Results	
Coefficient of determination	0.186
Global Mg flux (Tmol y^{-1})	1.27

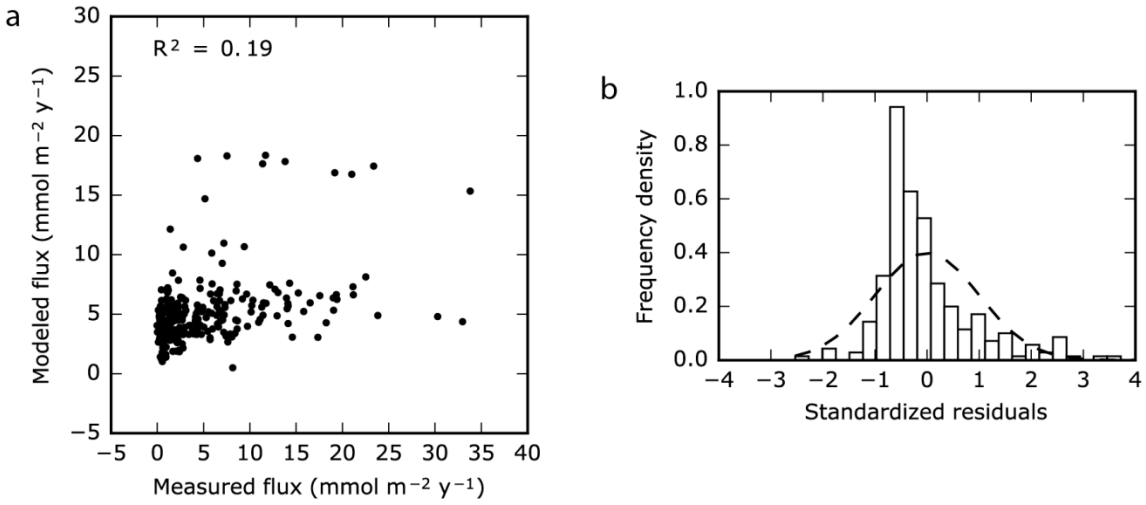

Figure 3.4 A) Measured magnesium flux values vs. model results via leave-one-out cross-validation, using the multiple linear regression technique with the parameters listed in Table 3.4. B) Histogram of standardized residuals of the cross-validation, with the dashed line showing an idealized normal distribution.

3.2.5 *Pore water magnesium isotope measurements*

Pore water magnesium isotopes from ODP Site 1039, IODP Sites U1378/U1380, U1414, and C0002, and NGHP Site 18 were measured via multi-collector inductively-coupled plasma mass spectrometry (MC-ICPMS) in the Isotope Laboratory at the University of Washington. Sample preparation and column chemistry were conducted in a clean lab, and the procedures followed those of previous studies (Liu et al., 2017; Teng et al., 2015). The pore water samples were dried, and then re-dissolved in 1N HNO_3 before chromatographic separation. Cation exchange chromatography, using Bio-Rad AG50W-X8 (200 –400 mesh) resin in 1 N HNO_3, was performed twice on each sample to chemically separate the magnesium from other ions in the samples. Magnesium isotopic compositions were analyzed using the sample-standard bracketing method on a Nu Plasma II MC-ICPMS (Teng and Yang, 2014). A seawater standard at variable concentrations was also analyzed with each batch of samples to monitor accuracy and reproducibility (Ling et al., 2011). Magnesium isotopic data are reported in delta (δ) notation in per mil relative to DSM3 standard (Galy et al., 2003). Repeated analyses indicate data reproducibility is ±0.06‰ (2σ) or better for δ^{26}Mg, far below the natural variations observed in the pore water profiles. Hydrothermal fluids from IODP Site 1253 CORK observatory samples were measured using the same procedures as the pore water samples (Solomon et al., 2009). All measured magnesium isotope analytical data are provided in the Table B1. Pore water magnesium isotope values from ODP Sites 925, 984, 1012, 1082, 1086, 1171, and 1219 were obtained from literature (Chanda and Fantle, 2017; Higgins and Schrag, 2010).

Fractionation factors associated with the fluxes of magnesium into the seafloor were calculated by calculating the concentration profiles of each isotope of magnesium individually from the bulk concentration and isotopic ratio measurements, then modeling the fluxes of each

isotope individually using the same model as for the bulk magnesium fluxes. The fractionation factor was then calculated:

$$\alpha = \frac{J_{26}/J_{24}}{(^{26}Mg/^{24}Mg)_O}$$

where J_{26} and J_{24} are the fluxes of ^{26}Mg and ^{24}Mg into the seafloor, respectively, and $(^{26}Mg/^{24}Mg)_O$ is the isotopic ratio in the ocean (0.13967) (Ling et al., 2011). Monte Carlo simulation was used to estimate the standard deviations of each fractionation factor based on the known uncertainty in the isotopic ratios, porosities, and pore water burial rates.

3.2.6 *Ocean-to-sediment magnesium isotope fractionation calculations and results*

To calculate concentrations of individual magnesium isotopes in pore waters, the absolute isotopic ratios are first calculated by:

$$\frac{^{26}Mg}{^{24}Mg}_{samp} = \left(\frac{\delta^{26}Mg}{1000} + 1\right) \times \frac{^{26}Mg}{^{24}Mg}_{DSM3}$$

$$\frac{^{25}Mg}{^{24}Mg}_{samp} = \left(\frac{\delta^{25}Mg}{1000} + 1\right) \times \frac{^{25}Mg}{^{24}Mg}_{DSM3}$$

where $^{26}Mg/^{24}Mg_{DSM3}$ = 0.13979, and $^{25}Mg/^{24}Mg_{DSM3}$ = 0.12685 (Young and Galy, 2004). Concentrations of individual magnesium isotopes (^{26}Mg and ^{24}Mg) in pore waters are calculated by:

$$\left[^{24}Mg\right] = \frac{[Mg]}{\frac{^{26}Mg}{^{24}Mg} + \frac{^{25}Mg}{^{24}Mg} + 1}$$

$$\left[^{26}Mg\right] = \left[^{24}Mg\right] \times \frac{^{26}Mg}{^{24}Mg}$$

Values of $\delta^{25}Mg$ are calculated using the mass-dependent relationship $\delta^{25}Mg = 0.516 \times \delta^{26}Mg$ for sites 925, 984, 1012, 1082, 1086, and 1219, for which $\delta^{25}Mg$ values were not published (Galy et al., 2000; Young and Galy, 2004). The absolute pore water isotope concentrations are then used to calculate fluxes (J) for each isotope individually, and used to calculate the ocean-to-sediment-column fractionation factor (α) by:

$$\alpha = \left(\frac{\frac{J_{26}}{J_{24}}}{\frac{^{26}Mg}{^{24}Mg}_{ocean}} \right)$$

3.2.7 *IODP Site 1253 magnesium isotope data and Rayleigh fractionation calculation*

The fractionation factor (α) associated with the transfer of magnesium from the Site 1253 hydrothermal fluid to the altered basalt are calculated as a Rayleigh fractionation:

$$\frac{R}{R_0} = \left(\frac{X}{X_0}\right)^{\alpha-1}$$

where R is the $^{26}Mg/^{24}Mg_{sample}$, R_0 is the $^{26}Mg/^{24}Mg_{ocean}$, X is the magnesium concentration in the sample (basaltic basement fluid), and X_0 is the magnesium concentration in the ocean. Epsilon (ε) values are calculated from α by the relationship:

$$\varepsilon = (\alpha - 1) \times 1000$$

Table 3.5. Magnesium isotope values of IODP Site 1253 basaltic basement fluid.

Expedition	Site	Sample	δ^{26}Mg (‰)	δ^{26}Mg 2σ (‰)	δ^{25}Mg (‰)	δ^{25}Mg 2σ (‰)
301T	1253	MKG150	-1.22	0.04	-0.63	0.04
301T	1253	MKG140	-1.25	0.04	-0.63	0.04
301T	1253	MKG130	-1.28	0.05	-0.65	0.05
301T	1253	MKG120	-1.27	0.05	-0.65	0.05

Table 3.6. Values used in the calculation of fractionation factor associated with basalt alteration, from IODP Site 1253 CORK samples (Solomon et al., 2009).

Sample	R	R_0	X (mM)	X_0 (mM)	α	ε (‰)
MKG150	0.139620	0.139674	25.0	54.0	1.000502	0.50
MKG140	0.139615	0.139674	24.1	54.0	1.000521	0.52
MKG130	0.139611	0.139674	25.4	54.0	1.000599	0.60
MKG120	0.139612	0.139674	25.3	54.0	1.000587	0.59

3.2.8 *Global extrapolation of ocean-to-sediment magnesium fractionation*

The flux-weighted average ocean-sediment magnesium fractionation is calculated as:

$$\varepsilon_{global} = \frac{\sum_{i=1}^{n} J_i \times \varepsilon_i}{J_{global}}$$

where J is the magnesium flux and ε is the ocean-sediment epsilon value, calculated at all n gridspaces. The ε value at each location is calculated separately for carbonate-dominated sediments and silicate-dominated sediments correlated to the total organic carbon (TOC) content of the top-most sediments at each location by the following equations:

For carbonate lithologies: $\varepsilon = -1.49 \times TOC - 0.11$

For silicate lithologies: $\varepsilon = -0.93 \times TOC + 1.03$

The lithology dataset of Dutkiewitcz et al., 2015 was used to globally determine the areas dominated by either carbonate or silicate sediments (Dutkiewicz et al., 2015). The silicate lithologies were defined as gravel and coarser, sand, silt, clay, radiolarian ooze, diatom ooze, sponge spicules, ash and volcanic sand/gravel, and siliceous mud. The carbonate lithologies were defined as calcareous ooze, mixed calcareous/siliceous ooze, shells and coral fragments, and fine-grained calcareous sediment. The global dataset of Lee and Wood, 2018 was used to determine total organic carbon contents of the surface sediments (Lee and Wood, 2018).

Table 3.7. Ocean-sediment magnesium fractionation model parameters and results.

Leg/ Expedition	Site	Holes	Number of datapoints used for gradients	Fit type	Epsilon (‰)	Standard deviation	Pore water d26Mg data source	Total organic carbon in upper sediment column (wt%)	Dominant lithology in upper sediment column
170	1039	BC	4	linear	0.18	0.09	This study	1.5	siliceous ooze
315	C0002	BD	3	linear	-0.77	0.19	This study	0.5*	lithogenic clay
344	U1414	A	3	linear	-0.33	0.30	This study	1.9	lithogenic clay
334	U1378	B	3	linear	-0.57	0.12	This study	2	lithogenic clay
NGHP01	18	A	3	linear	0.03	0.36	This study	1.1*	lithogenic clay
189	1171	ACD	6	linear	-0.64	0.41	(Chanda and Fantle, 2017)	0.5	calcareous ooze
162	984	ABCD	3	linear	0.41	0.77	(Higgins and Schrag, 2010)	0.3	lithogenic clay
167	1012	A	3	linear	-1.6	0.97	(Higgins and Schrag, 2010)	3.1	lithogenic clay
154	925	ABE	3	linear	-0.10	1.3	(Higgins and Schrag, 2010)	0.01	calcareous ooze
175	1082	A	4	linear	-1.0	0.42	(Higgins and Schrag, 2010)	3.5	lithogenic clay
175	1086	A	4	linear	-1.1	0.96	(Higgins and Schrag, 2010)	0.9	calcareous ooze
199	1219	AB	3	linear	0.17	0.25	(Higgins and Schrag, 2010)	0.1	siliceous ooze

*Total organic carbon concentrations in the upper sediment column at IODP Site C0002 and NGHP01 Site 18 were estimated based on the concentrations at nearby IODP Site C0001 and NGHP01 Site 19, respectively. NGHP01 refers to the Indian National Gas Hydrate Program Expedition 01.

The global distribution of fractionation factors associated with the fluxes of magnesium into the seafloor was determined by linear regression of the fractionation factors with total organic carbon in the uppermost sediment column at each site. Regressions were done separately for sites dominated by silicate and carbonate lithologies in their uppermost sediment columns. The global distribution was then calculated by applying the regression relationships to globally-gridded datasets of surface sediment lithology and organic carbon content (Dutkiewicz et al., 2015; Lee and Wood, 2018).

3.2.9 *Oceanic magnesium budget ranges and mass-balance calculations*

The sources of magnesium to the oceans include rivers (4.8-7.1 Tmol y^{-1}) (Wilkinson and Algeo, 1989), submarine groundwater input (~1.8 Tmol y^{-1}) (Dzhamalov and Safronova, 2002), and weathering of seafloor peridotites (0.0000018 – 4.1 Tmol y^{-1}) (Snow and Dick, 1995). The isotopic value for the groundwater source is assumed to be equivalent to the value of the river source, as has been observed for magnesium isotopes near Bunker Cave in Germany and near Florida Bay for calcium isotopes (Holmden et al., 2012; Immenhauser et al., 2010). All other isotopic values for the sources are from the literature (Liu et al., 2017; Tipper et al., 2006).

The sinks of magnesium from the ocean include the flux into the seafloor (0.6 – 1.7 Tmol y^{-1}, this study), high- temperature hydrothermal circulation (Mottl and Wheat, 1994), low-temperature hydrothermal circulation, biogenic carbonate precipitation (Milliman, 1974), and ion adsorption onto detrital clays (Drever et al., 1988). The flux into the seafloor and associated isotopic composition are from this study. The isotopic composition of the high-temperature sink is implied to be the same as seawater because it is fully depleted in high-temperature hydrothermal fluid. The low-temperature hydrothermal circulation flux and isotopic composition

are calculated as described by the mass-balance equations below. The biogenic carbonate isotopic composition is estimated based on 50% of the flux due to formation of coccoliths, with isotopic values ranging from -1 to -3‰, and the other 50% of the flux going to formation of foraminifera tests, with isotopic values ranging from -4.2 to -5.5‰ (Broecker and Clark, 2009; Gothmann et al., 2017; Higgins and Schrag, 2015; Pogge von Strandmann, 2008; Wombacher et al., 2011). Ion adsorption onto clays has been observed to occur with no measureable fractionation relative to the seawater with which it is in equilibrium (Wimpenny et al., 2014).

The low-temperature hydrothermal circulation sink for magnesium is calculated using the other quantified fluxes steady-state oceanic magnesium cycle, assuming steady-state:

$$J_{lthc} = J_r + J_{gw} + J_{spw} - J_{ms} - J_{hthc} - J_{bc} - J_{ia}$$

where J_r is the river flux, J_{gw} is the groundwater flux, J_{spw} is the seafloor peridotite weathering flux, J_{ms} is the marine sediment flux, J_{hthc} is the high-temperature hydrothermal circulation flux, J_{bc} is the biogenic carbonate flux, and J_{ia} is the ion adsorption flux.

To calculate the isotopic composition of the of the low-temperature hydrothermal circulation sink, the following mass-balance is used:

$$\delta_{lthc} = \frac{\delta_r J_r + \delta_{gw} J_{gw} + \delta_{spw} J_{spw} - \delta_{ms} J_{ms} - \delta_{hthc} J_{hthc} - \delta_{bc} J_{bc} - \delta_{ia} J_{ia}}{J_{lthc}}$$

where δ_r is the river δ^{26}Mg value, δ_{gw} is the groundwater δ^{26}Mg value, δ_{spw} is the seafloor peridotite weathering δ^{26}Mg value, δ_{ms} is the marine sediment δ^{26}Mg value, δ_{hthc} is the high-temperature hydrothermal circulation δ^{26}Mg value, δ_{bc} is the biogenic carbonate δ^{26}Mg value, and δ_{ia} is the ion adsorption δ^{26}Mg value.

3.3 Results and Discussion

Due to the sparse spatial coverage of ocean drilling sites in relation to the variability of magnesium fluxes into the seafloor, interpolation procedures are not able to consistently capture commonly-observed variations such as the higher magnitude fluxes closer to the continental margins. However, the ocean drilling dataset does represent a wide variety of environments, including abyssal ocean basins, convergent and divergent margins, and back-arc basins. More importantly, the dataset represents a wide range of areas with differing sedimentation rates, organic carbon sources, temperature regimes, and lithologies. For this reason, the 269 magnesium fluxes are used as a training dataset for modeling the global distribution of fluxes using gradient-boosting regression (GBR), a supervised machine learning technique. The characteristic diversity of the dataset lends itself well to prediction of fluxes in the global ocean from globally-gridded datasets of other parameters such as sediment accumulation rate, surface sediment porosity, surface ocean productivity, bottom water temperature, and water depth (Table 3.1). Similar methods have previously been used to estimate the global distribution of sulfate reduction rates, as well as gas hydrate occurrence and surface sediment porosity (Bowles et al., 2014; Martin et al., 2015; Wood et al., 2014). Because localized processes, such as seafloor seeps and diffusion from relict brines, are not reflected in available globally-gridded datasets, the regression technique does not account for their effect on the distribution of fluxes. However, these areas are much more limited in extent and magnitude than the biogeochemically-driven fluxes of magnesium into marine sediments (Wallmann et al., 2008; Warren, 2010).

The GBR results indicate that fluxes are generally higher near the continental margins and lower in the abyssal ocean basins (Figure 3.1a and 3.1b). The higher fluxes of magnesium into sediments near continental margins are consistent with what is expected in areas with higher

organic carbon burial rates, alkalinity production, and authigenic carbonate precipitation. The total flux of magnesium from the ocean into marine sediments calculated using the GBR method is 1.1 $\pm$ 0.5 Tmol y^{-1} (1 Tmol = 10^{12} mol), a similar magnitude as the high-temperature hydrothermal flux (Mottl and Wheat, 1994). We also calculate the total flux using random forest regression and multiple linear regression, for comparison. The flux calculated with the GBR method is the same as that calculated using random forest regression (1.1 Tmol y^{-1}), and similar to the multiple linear regression result (1.3 Tmol y^{-1}), with the GBR method having the greatest accuracy of the three methods (Figures 3.2 – 3.4). This value is also within the 0.9 – 1.8 Tmol y^{-1} range of the global diffusive flux of magnesium estimated using an interpolation procedure (Sun and Turchyn, 2014).

In addition to the global flux distribution, we calculate the net fractionation associated with the magnesium flux into the seafloor at twelve ocean drilling locations (Figure 3.5). The twelve locations include sites from continental margins and abyssal ocean basins, with a range of lithologies and organic carbon burial rates. Authigenic mineral formation reactions occurring in the sediment column change the isotopic ratios of the pore water magnesium, creating an isotopic gradient between the overlying ocean water and the pore waters. This isotopic gradient results in a fractionation associated with the diffusional transport of magnesium from the ocean into the pore waters of the sediments. In contrast, the burial of seawater during sedimentation occurs without isotopic fractionation. So, while pore water burial increases the total flux of magnesium into the seafloor, it acts to dampen the magnitude of the net fractionation factor associated with that flux of magnesium.

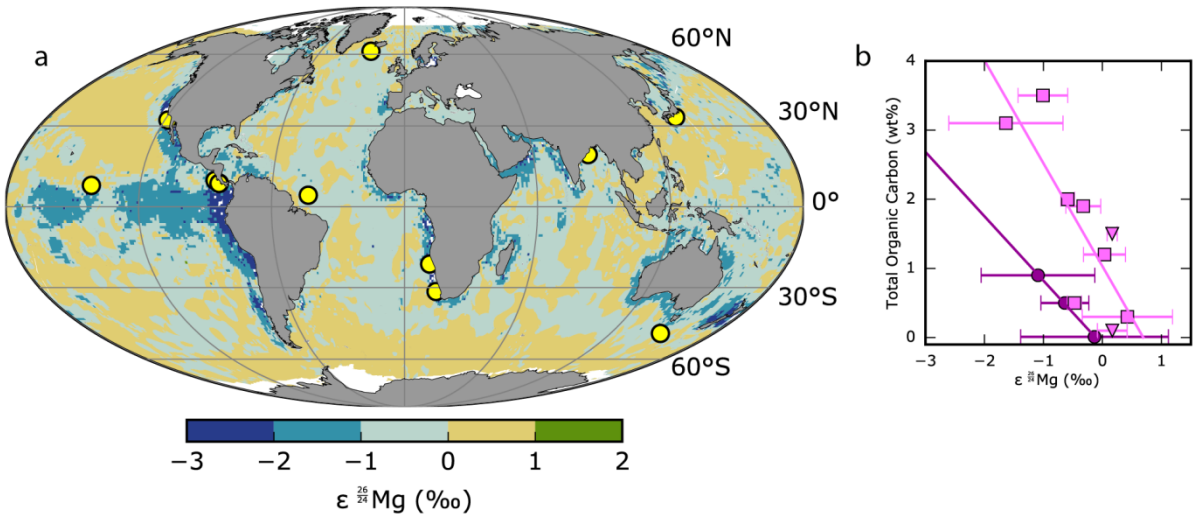

Figure 3.5 Fractionation of magnesium isotopes into marine sediments. a) Global distribution of the isotopic fractionation of magnesium isotopes associated with the magnesium flux across the sediment-water interface. Yellow dots are the ocean drilling locations where the fractionations are calculated. b) Isotopic fractionation of magnesium isotopes plotted versus total organic carbon in the upper sediment column. Linear regressions are fit to the data for calcareous sediments (dark purple), and siliceous sediments (light purple) separately. Circles are calcareous oozes, squares are lithogenic sediments, and triangles are siliceous oozes. Epsilon values are for fractionation from the ocean bottom water into the seafloor.

The fractionations associated with the fluxes from the ocean into the sediment column range from -1.6‰ to 0.4‰, within the range for authigenic carbonate formation and aluminosilicate formation, respectively. We find that the net flux into the modern seafloor acts to increase the magnesium isotopic ratio in the ocean, reflecting greater fractionation due to authigenic carbonate formation compared to aluminosilicate formation in the upper sediment column at most sites. There is no clear correlation between the magnitude of the fluxes and the isotopic fractionation factors. Rather, sites with more positive fractionations tend to be those with clay-dominated lithologies and low organic carbon contents, while sites with greater amounts of organic carbon or more carbonate-dominated sediments have more negative fractionation values (Figure 3.5b). These findings are consistent with studies of net fractionation of magnesium isotopes during diagenesis (Chanda and Fantle, 2017; Higgins and Schrag, 2010).

A simple binned regression of sites (Figure 3.5b) based on total organic carbon content and lithology of surface sediments provides a global distribution of the isotopic fractionation associated with the global flux of magnesium into marine sediments (Figure 3.5a). From this regression, we calculate a flux-weighted isotopic fractionation factor of 0.9997 associated with the global flux, indicating the dominance of authigenic carbonate formation in driving the fractionation associated with the global diffusional magnesium flux into marine sediments (See Table 3.7). These results are also consistent with the slight enrichment in light magnesium isotopes of global subducting sediments compared with average continental crust (Hu et al., 2017).

By quantifying this magnesium sink and associated isotopic fractionation, we can more accurately constrain the modern global magnesium budget, including the low-temperature ridge flank sink. The dominant sources of magnesium to the ocean are rivers and groundwater, which input a combined total of about 7 Tmol y^{-1}, with a minor contribution from weathering of seafloor peridotites (Table 3.8). Assuming the present-day oceanic magnesium cycle is in steady state, the sinks of high and low temperature hydrothermal circulation, marine sediments, and biogenic carbonates also have a combined magnitude of about 7 Tmol y^{-1}. After accounting for independent estimates of the magnesium fluxes and isotopic fractionations associated with the known sources and sinks of oceanic magnesium, including the flux into marine sediments found in this study, low-temperature ridge flank hydrothermal circulation accounts for the remaining 3.9 Tmol y^{-1}, making it the largest sink for magnesium in the ocean (Table 3.8, see 3.2.9 for mass balance calculations). Sequestration of magnesium into platform carbonates during pore water advection through these systems may be an additional sink of magnesium, but has not yet been

independently quantified for the modern ocean (Fantle and Higgins, 2014; Holland and Zimmermann, 2000).

Table 3.8. Global oceanic magnesium budget. The budget includes the sources of magnesium to the ocean and sinks of magnesium from the ocean, with their corresponding isotopic delta values. Values in are best estimates for each source/sink, see Section 3.2.9 for full ranges and references.

Sources	**Flux (Tmol y^{-1})**	**δ^{26}Mg (‰)**	**References**
Rivers	5.2	-1.09	Section 3.2.9
Groundwater	1.8	-1.09	Section 3.2.9
Seafloor peridotite weathering	0.15	-1.31	Section 3.2.9
Sinks			
Marine sediments	1.1	-1.1	This study
High-temperature ridge crest circulation	1.5	-0.83	Section 3.2.9
Low-temperature ridge flank circulation	3.9	-0.8	Calculated in this study
Biogenic carbonates	0.6	-3.5	Section 3.2.9
Ion adsorption onto detrital clays	0.1	-0.8	Section 3.2.9

Using the fluxes and isotopic values of the sources and sinks in Table 3.8, the isotopic composition of the low-temperature ridge flank sink is found to be nearly identical to seawater, indicating no significant net isotopic fractionation (see Section 3.2.9 for mass balance calculation and assumptions). The lack of net fractionation associated with the global low-temperature ridge flank sink is contrasted with the fluid-basalt fractionation factor of 1.00055 calculated from carbonate-barren basaltic basement at IODP Site 1253 (Tables 3.5 and 3.6), which is likely dominated by high-magnesium clay formation as found at IODP Site 1256 near the East Pacific Rise, and the carbonate-poor lower basement of Site 801C outboard of the Mariana Trench (Huang et al., 2015; Huang et al., 2018). The low net fractionation value can be explained by the observation that carbonate veins commonly form during low-temperature hydrothermal circulation, as has been observed in magnesium isotope measurements on altered basalts from

ODP Site 504B near the Costa Rica Rift and the carbonate-rich upper basement at Site 801C (Beaumais et al., 2017; Huang et al., 2018). Precipitation of isotopically-light carbonate during low-temperature hydrothermal circulation can reduce the net fractionation associated with this sink, counteracting the fractionation caused by formation of isotopically-heavy aluminosilicates. A low net fractionation during low-temperature hydrothermal circulation suggests that the marine δ^{26}Mg record is primarily controlled by variations in continental weathering, biogenic carbonate formation, particulate organic carbon burial, and diagenetic processes in marine sediment. If the unquantified flux of magnesium associated with the recrystallization of platform carbonates during advective pore water circulation is significant, this additional magnesium sink, with a fractionation factor of 0.9980, would require the low-temperature ridge flank flux to have an heavier isotopic composition (Fantle and Higgins, 2014; Higgins and Schrag, 2012; Mavromatis et al., 2014). Additional factors that may be important controls on the δ^{26}Mg record in the past include the relative preservation rates of foraminifera tests versus coccoliths, and the relative amount of carbonate precipitation versus clay formation during low-temperature ridge flank circulation. These new constraints on the oceanic magnesium cycle offer greater insight into the present-day magnesium cycle and provide a benchmark for models and interpretations of the paleo-oceanographic record.

Chapter 4. FORMATION RATES OF MAGNESIUM-BEARING CARBONATE AND CLAY MINERALS IN MARINE SEDIMENTS

ABSTRACT

Authigenic mineral formation reactions in marine sediments drive exchange of elements between the ocean and lithosphere and are important in many marine geochemical cycles. A more complete understanding of these subseafloor reactions is needed to understand how they affect the oceanic alkalinity, ^{13}C, and $H_2{}^{18}O$ cycles, as well as mineral-bound water delivery to subduction zones. Although authigenic reactions may be globally important, their magnitudes are difficult to quantify due to the relatively small geochemical variations they imprint on bulk sediment. Here, we present a multicomponent reactive-transport model that utilizes pore water concentration profiles of Mg^{2+}, Ca^{2+}, and $\delta^{26}Mg$ from scientific ocean drilling sites to constrain the rates and cumulative amounts of authigenic clay formation, carbonate formation, and carbonate recrystallization in marine sediments.

We apply the multicomponent model to nine ocean drilling sites, including those characterized by pelagic and hemipelagic sedimentation. At these sites, we find that authigenic clay formation in the deep subsurface (>1 meter below seafloor) is a widespread process that accounts for the formation of up to 8 wt% of the bulk sediment. The rate of authigenic clay formation in the deep subsurface could amount to the equivalent of a few percent of the rate of sediment input into the ocean from rivers, and could account for approximately 6% of the structural water content of subducting sediment. Due to the large isotopic fractionation associated with low-temperature authigenic clay formation, this geochemical sink of ^{18}O-

enriched structural water is an important component of the long-term (~10^8 year) oxygen isotope budget of the ocean. The model results indicate that the rates of authigenic carbonate formation in the upper sediment column are underestimated by a factor of at least 1.5 to 2 by models that solely utilize the calcium concentration profiles, suggesting authigenic carbonate formation has a greater role in the long-term carbon cycle and ^{13}C cycle of the ocean than previously estimated. The results from this study add support to evidence for the importance of authigenic mineral formation in global geochemical cycles.

4.1 INTRODUCTION

Formation of authigenic minerals in marine sediments is a globally significant geochemical process for several major chemical cycles in the ocean on timescales of 10^5 – 10^9 years. For example, sulfide mineral precipitation in anoxic marine sediments sequesters sulfate at a rate equal to 15–30% of the flux from rivers (Berner, 1982; Bowles et al., 2014), and authigenic clay formation may account for up to 95% of the potassium removal in the ocean (Berner and Berner, 2012; Michalopoulos and Aller, 1995). Recent estimates of the net global fluxes of magnesium and calcium into marine sediments indicate that authigenic mineral formation is also important in these element cycles (Berg et al., 2018; Sun et al., 2016).

Previous studies have explored the processes controlling magnesium uptake in marine sediments by calculating net rates of magnesium uptake and the associated net isotopic fractionation (Berg et al., 2018; Higgins and Schrag, 2010). These studies suggest that authigenic clay and carbonate formation are important processes in the global magnesium cycle on geologic timescales, which is consistent with estimates of formation rates from calcium fluxes and solid-phase measurements (Dunlea et al., 2017; Sun et al., 2016). However, while net magnitudes of

uptake and isotopic fractionation can distinguish whether the δ^{26}Mg of the pore fluid is controlled by clay formation or carbonate formation, they do not provide the magnitudes of the magnesium uptake due to each individual process. The amount of magnesium uptake due to the individual processes are required to estimate the associated rates of clay and carbonate precipitation, which affect the dynamics of the oceanic δ^{26}Mg, Mg/Ca, and δ^{18}O cycles, and how these processes affect the global carbon cycle (Berg et al., 2018; Higgins and Schrag, 2010; Wallmann, 2001).

Hydrous aluminosilicate minerals in marine sediments are formed *in situ* via tephra alteration, primary silicate weathering, and reverse weathering e.g. (Gieskes and Lawrence, 1981; Kastner, 1981; Michalopoulos and Aller, 1995; Solomon et al., 2014; Wallmann et al., 2008). The aluminosilicate minerals that form in marine sediments are predominantly cation-rich smectite clays and zeolites with high surface area and cation exchange capacity (Kastner, 1981). A typical example of this in the marine environment is the aluminum-limited weathering of plagioclase to montmorillonite clay:

$$1.1CaNaAl_3Si_5O_{16} + 2.5SiO_2 + 0.8Mg^{2+} + (2.6+n)H_2O + 1.2CO_2 \rightarrow (Mg_{0.1}Ca_{0.1}Na_{0.3})(Al_{3.3}Mg_{0.7})[Si_8O_{20}](OH)_4 \cdot nH_2O + 1.0Ca^{2+} + 1.2HCO_3^- + 0.8Na^+$$

Clay minerals such as montmorillonite not only consume water during their formation, but also incorporate a range of other elements into their crystal structures and onto surface adsorption sites. Formation of these minerals from relatively cation-depleted material results in scavenging of some major and minor elements from pore waters (e.g. Mg, K, Li, B), while releasing other elements (e.g. Ca) (Gieskes and Lawrence, 1981; Kastner, 1981). Because of this, understanding the rates of clay formation in marine sediments is important for a first-order

understanding of how this process affects chemical cycles in the ocean, including the sequestration of ^{18}O-enriched water in the mineral structures and interlayers of the authigenic clay minerals. The sequestration of this water in marine sediments may affect the mineral-bound water delivery into subduction zones, as well as the oceanic ^{18}O cycle on geologic timescales (Kastner et al., 2014; Moore and Vrolijk, 1992; Wallmann, 2001).

Authigenic carbonates precipitate in anoxic marine sediments as alkalinity increases due to organic carbon oxidation e.g. (Claypool and Kaplan, 1974; Milliman, 1974). A recent study using net fluxes of calcium into marine sediments to estimate the total alkalinity flux into authigenic carbonates has shown that this process accounts for at least 10% of the carbonate burial in the modern abyssal ocean (Sun and Turchyn, 2014). However, at the pore water Mg^{2+}:Ca^{2+} ratios in the deep subsurface (>1 meter below seafloor), authigenic carbonate is precipitated with both magnesium and calcium. The carbonate that forms is typically composed of approximately 10% $MgCO_3$ when pore waters have the composition of seawater, and increasing with increasing temperature and Mg^{2+}:Ca^{2+} ratio (Morse and Mackenzie, 1990; Snyder et al., 2007). Thus, the assumption of pure calcium carbonate results in significant underestimation of the total authigenic carbonate sink.

More importantly, using net calcium uptake to calculate total carbonate formation further underestimates formation rates by not accounting for the additional calcium being released to pore waters from other diagenetic reactions such as recrystallization of biogenic carbonates to higher-magnesium carbonates. During recrystallization at the temperatures of early diagenesis in marine sediments, carbonates are dissolved *in situ* and reprecipitated within the sediment column. Even in bulk pore waters that are above carbonate saturation, this process may be driven by a combination of forces including dissolution within undersaturated microenvironments,

excess surface free energy of biogenic particle structures relative to inorganically-precipitated crystals, and pressure solution at grain-to-grain contacts in the sediment column (Baker et al., 1980; Baker et al., 1982). Carbonate recrystallization is a common process within marine sediments, having been observed in sediments from a wide range of environments including open ocean carbonate packages and hemipelagic margin sediments (Baker et al., 1980; Baker et al., 1982; Chanda and Fantle, 2017; Delaney, 1989; Fantle, 2015; Huber et al., 2017).

Other processes that can contribute additional calcium to pore waters are aluminosilicate weathering and equilibrium cation exchange (Gieskes and Lawrence, 1981; Kastner, 1981). To fully evaluate the effect of diagenetic reactions on the alkalinity budget of the ocean, the calcium supply from these two processes, in addition to carbonate recrystallization and the supply from the overlying ocean, must be accounted for when calculating the total rates of carbonate precipitation.

These *in situ* processes also have implications for the carbon isotope cycle between marine sediments and the ocean. When formed in the upper sediment column, authigenic carbonates typically have lower $\delta^{13}C$ values than biogenic carbonate or dissolved inorganic carbon in seawater e.g. (Naehr et al., 2007; Schrag et al., 2013). So, total rates of CO_3^{2-} uptake and exchange during authigenic carbonate formation and carbonate recrystallization can affect the carbon isotope cycle in the ocean and are needed to determine the significance of these authigenic processes to the oceanic $\delta^{13}C$ record.

The purpose of this study is to constrain the magnitudes of authigenic clay formation, total carbonate precipitation, and carbonate recrystallization in marine sediments as a first-order evaluation of the effect these processes have on global geochemical cycles. We present a multicomponent reactive-transport model that utilizes pore water Mg^{2+}, Ca^{2+}, and $\delta^{26}Mg$ data

from scientific ocean drilling cores to quantify the rates of hydrous aluminosilicate formation, carbonate precipitation, and carbonate recrystallization in deep marine sediments. This multicomponent model approach provides empirical constraints on the reaction rates, while avoiding variability and sensitivity issues associated with solid-phase measurements. The model is applied to nine ocean drilling sites, including five sites characterized by hemipelagic sedimentation, and four pelagic sedimentation sites (Figure 4.1). These nine sites are used to evaluate the importance of authigenic mineral formation to marine geochemical cycles, including the alkalinity, $\delta^{13}C$, and $\delta^{18}O$ cycles, and the uptake of water into hydrous aluminosilicates.

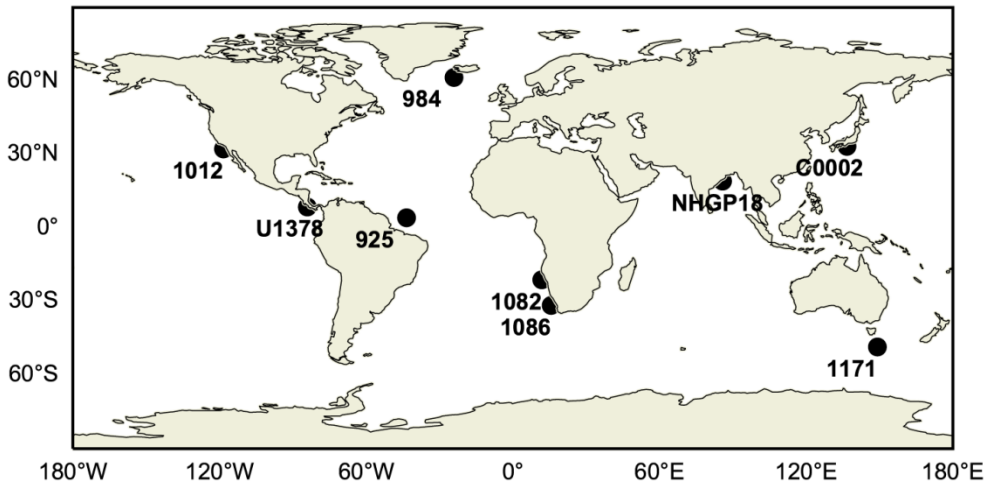

Figure 4.1. Map of the nine ocean drilling site locations analyzed in this study.

4.2 METHODS

4.2.1 *Model description*

The total rates of clay formation, carbonate precipitation, and carbonate recrystallization in marine sediments are calculated using a multicomponent 1-dimensional steady-state reactive-transport model. After accounting for cation exchange, the model calculates the total rates of

magnesium uptake associated with authigenic mineral formation in the sediment column at each ocean drilling site. Then, using the stoichiometries and magnesium isotopic fractionation factors associated with the three authigenic mineral reactions, the proportions of the magnesium uptake associated with each reaction at each depth interval are fit to the calcium and magnesium isotope reaction rate profiles. The three reactions are defined as:

Authigenic clay formation:

$$primary\ aluminosilicate + H_2O + xCO_2 + yMg^{2+} + other\ cations \rightarrow\ clay + xHCO_3^- + zCa^{2+} + other\ cation$$

Primary authigenic carbonate precipitation:

$$xCa^{2+} + yMg^{2+} + CO_3^{2-} \rightarrow Ca_xMg_yCO_3$$

Carbonate recrystallization:

$$Ca_xMg_yCO_3 + zMg^{2+} \rightarrow Ca_{x-z}Mg_{y+z}CO_3 + zCa^{2+}$$

The multicomponent model takes advantage of the unique signatures each of these three reactions has on pore water magnesium and calcium concentrations, and magnesium isotope ratios, as illustrated in Figure 4.2. The model couples all three reactions to simultaneously solve for the stoichiometry and relative fractions of the three reactions that together satisfy the depth profiles of the three pore water components. The stoichiometries of each mineral are then used to calculate the amounts of each that are formed from the calculated rates. The stoichiometric coefficients for these reactions are variable in marine sediments, depending on the environmental conditions and mineralogy of the existing sediments. The stoichiometry ranges and isotopic fractionation factors considered in the model are discussed further in Section 4.2.1.4.

	$[Mg^{2+}]$	$[Ca^{2+}]$	$\delta^{26}Mg$
Clay formation	↓	↑	↓
Carbonate precipitation	↓	↓	↑
Carbonate recrystallization	↓	↑	↑

Figure 4.2. The effect of each in situ reaction on the pore water values of the three components (magnesium and calcium concentrations, and magnesium isotope ratios). Upward arrows indicate increases in the pore water values, and downward arrows indicate decreases. Each reaction has a unique signature on the pore water chemistry.

A schematic of the model architecture is shown in Figure 4.3 and each component of the model is described individually in Sections 4.2.1.1 – 4.2.1.5. In this new approach, the net steady-state pore water magnesium reaction rate profile is combined with equilibrium ion exchange rates, giving the reaction rates profile associated with only the combined uptake of magnesium from pore water due to clay formation, carbonate precipitation, and carbonate recrystallization. Then, the proportions of the magnesium uptake that each of the three reactions are responsible for are determined by applying an iterative gradient descent algorithm to coupled reactive-transport models for pore water Mg^{2+}, Ca^{2+}, and $\delta^{26}Mg$. The depth profiles of Ca^{2+} and $\delta^{26}Mg$ that result from these reaction rates are determined using the parameterized stoichiometries (Mg:Ca reaction ratio) and fractionation factors of each of the three reactions. Because a range of stoichiometries and fractionation factors are possible for each of the reactions, every possible combination of those ranges are used to find the maximum range of reaction rates.

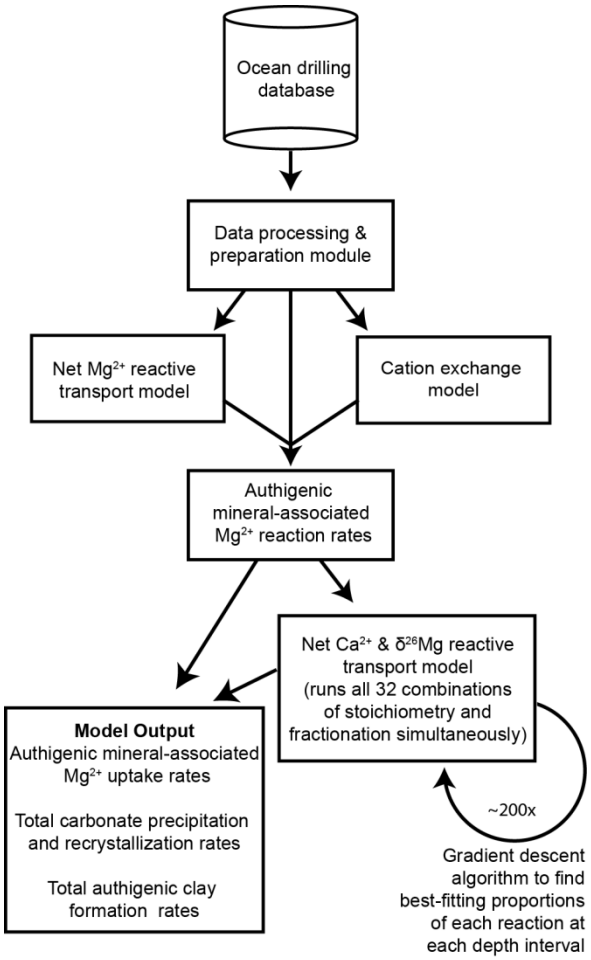

Figure 4.3 – Diagram of the multicomponent model architecture.

4.2.1.1 Net magnesium reactive-transport model

The model calculates the steady-state net reaction rate profile for magnesium using the central difference formulation of the 1-dimensional advection-diffusion equation in porous media:

$$R_{net_i} = \frac{(\varphi D_{sed})_i (C_{i+1} - 2C_i + C_{i-1})}{dz^2} - \frac{b_i (C_{i+1} - C_{i-1})}{2dz}$$

where:

R_{net_i}: net reaction rate at interval i (mol m^{-3} y^{-1})

C: pore water magnesium concentration (mol m^{-3})

φ: sediment porosity

D_{sed}: effective sediment diffusion coefficient ($m^2\ y^{-1}$)

b: volumetric pore water burial flux ($m^3\ y^{-1}$)

dz: interval thickness (m)

The model domain is divided into 50 equally-spaced intervals, with the upper boundary at the sediment-water interface and the lower boundary at the deepest measured pore water magnesium concentration value. The depth profiles of magnesium concentration, porosity, and sediment age are fit to curves as a regularization method, which prevents large variations arising in the model output from small-scale variations in these parameters due to measurement errors or sampling artifacts. Magnesium concentrations at the 50 depth intervals are interpolated using a smoothed curve fit to the measured concentrations. Consistent with the steady-state model formulation, Dirichlet boundary conditions are employed for the pore water concentrations, with the deepest fitted concentration as the bottom boundary, and the upper boundary set at the average seawater concentration that is adjusted for salinity using the NOAA World Ocean Atlas gridded salinity dataset (Zweng et al., 2013). The sediment age-depth relationship is fit with a piecewise linear regression of the biostratigraphic age-depth data. Measured sediment porosity profiles are used to fit an Athy's Law curve:

$$\varphi = (\varphi_0 - \varphi_L)e^{-az} + \varphi_L$$

where φ_0 is the porosity at the sediment-water interface, φ_L is the porosity at depth where compaction of the sediment column becomes negligible, z is depth, and a is an empirical compaction coefficient. If differential compaction of lithologic units is apparent in the porosity profile, the Athy's Law model is fit to the uppermost compaction regime. The cutoff depths for the porosity curve fits are listed in Table C2.

The effective sedimentary diffusion coefficient, D_{sed}, is calculated at each depth interval, accounting for sediment tortuosity with the relationship (Boudreau, 1996):

$$D_{sed} = \frac{D_{sw}}{(1 - \ln(\varphi^2))}$$

where D_{sw} is the molecular diffusion coefficient in seawater corrected for bottom water temperatures and geothermal gradient using the Stokes-Einstein equation (Locarnini et al., 2013).

The calculated volumetric pore water burial flux accounts for sediment compaction using the relationship:

$$b = \frac{\varphi_L S_v}{(1 - \varphi_L)}$$

where S_v is the dry sediment volume accumulation rate (m^3 y^{-1}), which is calculated by integrating the total dry sediment volume over the depth range corresponding to the most recent sedimentation regime; that is, the uppermost depth range over which sedimentation rate has been nearly constant:

$$S_v = \frac{\int_0^h (1 - \varphi) dz}{t_h}$$

where h is the deepest depth within the most recent sedimentation regime package, and t_h is the age corresponding with that depth.

4.2.1.2 Cation exchange model

Rates of equilibrium cation exchange of Mg and Ca are calculated for sediments undergoing burial in a steady-state sedimentation and compaction regime. The underlying assumption of the cation exchange model is that the sediments are in equilibrium with the surrounding pore water on the timescales under consideration. The amount of each cation adsorbed to each type of

adsorbant sediment, *j* (smectite, illite, chlorite, kaolinite, and opal) at each depth interval, *i*, is calculated accounting for pore water concentrations of magnesium or calcium, and ammonium, and the cation exchange capacity of the solids using the formulation (von Breymann et al., 1990a):

$$\langle X_{sorb}\rangle_{i,j} = \left(\frac{CEC_j \cdot [X]_i}{\alpha_{Mg} + \beta_{Mg}[X]_i} - \left(\frac{[NH_4]_i^2 \cdot K_j \cdot CEC_j \cdot \langle X_{sorb}\rangle_{i,j}}{[X]_i}\right)^{1/2}\right) \cdot f_j$$

where:

$<X_{sorb}>$ is the amount of exchange sites occupied by either magnesium or calcium (meq kg^{-1})

[X] is the pore water concentration of magnesium or calcium (mM)

CEC is the cation exchange capacity (meq kg^{-1})

α_{Mg} (mM) and β_{Mg} (unitless) are empirical constants

K_{cond} is the conditional exchange constant (L $mmol^{-1}$)

f_j is the dry weight fraction of adsorbant sediment type j

The values of $<X_{sorb}>_{i,j}$ are found using an iterative gradient-descent method to within <0.1% of the best-fit values. The dry weight fraction of each adsorbant sediment type are assigned from measured values in the individual site reports or estimated based on global distributions of surface sediment lithology (Griffin et al., 1968). The model domain for each site is limited to the depth over which f_j values, and thus also CEC values, are approximately constant. The empirical constants α and β relate the amount of adsorbed cations in bulk sediment (X_{sorb}) to the concentration of the cation in the pore water at a given temperature (Sayles and Mangelsdorf Jr, 1977; von Breymann et al., 1990a). Because the temperature effect is small for the empirical constants α, β, and K_i for magnesium and calcium, these are also kept constant

within the model domain (von Breymann et al., 1990a; Von Breymann and Suess, 1988). The values for α and β are approximated with those for a hemipelagic sediment, and CEC, K_{cond} are specified for each adsorbant sediment type (Laudelout et al., 1968; Sayles and Mangelsdorf Jr, 1977; von Breymann et al., 1990a; Von Breymann and Suess, 1988). The values of CEC, K_{cond}, α, and β used for both Mg and Ca in this study are listed in Table C1.

The total amount of adsorbed magnesium and calcium per kilogram dry sediment (mmol kg^{-1}) at each depth interval is calculated by adding the amount adsorbed to each sediment type and correcting for the divalent charge:

$$\{X_{sorb}\}_i = \frac{1}{2}\sum_{j=1}^{n} \langle X_{sorb} \rangle_{i,j}$$

And the steady-state rates of net cation exchange (mol m^{-3} y^{-1}) at each depth interval are calculated by:

$$R_{ex_i} = \frac{S_v \cdot \rho \cdot (\{X_{sorb}\}_i - \{X_{sorb}\}_{i-1})}{1000dz}$$

where ρ is the grain density, set at a constant 2600 kg m^{-3} in the model domain for each site, and *dz* is the interval thickness (m). Positive values of R_{ex} correspond to uptake of magnesium onto adsorbant minerals from pore water as sediment is buried.

The isotopic ratio of the magnesium being adsorbed or desorbed due to equilibrium cation exchange is also calculated with a mass balance approach. The constraint of no difference in isotopic ratios between pore water magnesium and adsorbed magnesium (i.e. no isotopic fractionation) for any given interval is supported by batch experiments on marine clays (Wimpenny et al., 2014). The formulation follows from the mass balance:

$$\{Mg_{sorb}\}_{i-1} \cdot \delta^{26}Mg_{i-1} - \{Mg\}_{ex_i} \cdot \delta^{26}Mg_{ex_i} = \{Mg_{sorb}\}_i \cdot \delta^{26}Mg_i$$

where $\delta^{26}Mg_{ex_i}$ is the isotopic composition of the magnesium exchanged as sediment is buried from an interval into the next underlying interval, and $\{Mg\}_{ex_i}$ is the amount of magnesium exchanged per kilogram dry sediment in that underlying interval:

$$\{Mg\}_{ex_i} = \{Mg_{sorb}\}_i - \{Mg_{sorb}\}_{i-1}$$

And rearranging the mass balance equation and substituting the above equation to solve for the isotopic ratio of the exchanged magnesium:

$$\left(\frac{^{26}Mg}{^{24}Mg}\right)_{ex_i} = -\left(\left(\frac{\{Mg_{sorb}\}_i \cdot \delta^{26}Mg_i - \{Mg_{sorb}\}_{i-1} \cdot \delta^{26}Mg_{i-1}}{\{Mg_{sorb}\}_i - \{Mg_{sorb}\}_{i-1}} \Big/ 1000\right) + 1\right) \cdot {}^{26}F_{std}$$

where $^{26}F_{std}$ is the $^{26}Mg/^{24}Mg$ in the DSM3 magnesium isotope standard. The rate of adsorption or desorption for individual isotopes ^{24}Mg and ^{26}Mg are then calculated at each depth interval as:

$$R_{24_i} = \frac{R_{ex_i}}{1 + \left(\frac{^{26}Mg}{^{24}Mg}\right)_{ex_i} + \left(\frac{^{25}Mg}{^{24}Mg}\right)_{ex_i}}$$

And:

$$R_{26_i} = R_{24_i} \cdot \left(\frac{^{26}Mg}{^{24}Mg}\right)_{ex_i}$$

4.2.1.3 Total authigenic mineral-associated reaction rates

The total rates of magnesium uptake from pore water due to clay formation, carbonate precipitation, and carbonate recrystallization are calculated at each interval *i*, taking into account rates of equilibrium cation exchange and net reaction rates:

$$R_{auth_i} = R_{net_i} - R_{ex_i}$$

This same calculation is also done for the calcium reaction rate profile. However for calcium, R_{auth} does not necessarily represent net uptake of calcium from pore waters, because the in contrast to magnesium, carbonate recrystallization and clay formation result in a release of calcium into pore waters.

4.2.1.4 Iterative gradient descent method

The proportions of the total magnesium uptake rate driven by carbonate precipitation, recrystallization, and clay formation are found simultaneously using an iterative gradient descent procedure. The proportions of each reaction are iteratively adjusted to find the best fit to the profiles of magnesium concentration, calcium concentration, and magnesium isotopic ratios at a given site. The sum of the magnesium uptake of all the reactions at each interval must equal the total magnesium uptake rate at that interval.

Reaction stoichiometries of magnesium and calcium are determined using empirical reaction ratios of mineral dissolution and formation in the marine sedimentary environment. The Mg:Ca ratio in precipitated and recrystallized carbonates is parameterized using laboratory-determined distribution coefficients between the minerals and the Mg^{2+}:Ca^{2+} ratio in the pore water (Morse and Mackenzie, 1990). The Mg:Ca reaction ratio for the replacement of calcium for magnesium during carbonate recrystallization is set at -1 rather than providing a range, recognizing the 1:1 nature of the replacement. The number of moles of calcium released to pore water for every mole of magnesium removed during authigenic clay formation is parameterized using the reaction stoichiometries of the incongruent weathering of plagioclase, which is also consistent with other studies of authigenic clay formation based on measurements of magnesium

and calcium in marine pore waters e.g. (Gieskes and Lawrence, 1981; Miller et al., 1979). The fractionation factors for authigenic carbonate precipitation and clay formation are also kept constant within the model domain, with the same fractionation factors used for primary authigenic carbonate precipitation and carbonate recrystallization (Gothmann et al., 2017; Higgins and Schrag, 2012; Immenhauser et al., 2010; Liu et al., 2017; Milliman, 1993; Pogge von Strandmann, 2008; Pogge von Strandmann et al., 2014; Tipper et al., 2006; Wimpenny et al., 2014; Wombacher et al., 2011).

For each site, the full range of possible reaction proportions at each interval is found using all possible combinations of the minimum and maximum reaction stoichiometries and fractionation factors. With variable stoichiometric ratios for carbonate precipitation and clay formation, a constant stoichiometric ratio for carbonate recrystallization, and variable fractionation factors for carbonate precipitation/recrystallization and clay formation, 16 different combinations are needed to test the full possible range of profiles of the proportions of the gross magnesium uptake that is due to each reaction. The parameterization of the ranges in the reaction stoichiometries and fractionation factors are listed in Table C1.

For each iteration of those 16 model runs, the steady-state profiles of calcium and magnesium concentration, and magnesium isotopic ratios are calculated from the rate profiles using a bounded steady-state variation of the tridiagonal algorithm outlined in Glover et al. (2011). Rearranging the central difference formula, an interior point equation can be written as:

$$\alpha_i C_{i-1} + \beta_i C_i + \gamma_i C_{i+1} = 0$$

where:

$$\alpha_i = \frac{(\varphi D_{sed})_i}{dz^2} + \frac{b_i}{2dz}$$

$$\beta_i = -\left(\frac{2(\varphi D_{sed})_i}{dz^2} + \frac{b_i}{2dz}\right)$$

$$\gamma_i = \frac{(\varphi D_{sed})_i}{dz^2}$$

Using Dirichlet boundary conditions for the upper and lower bounds of the model domain, the interior point equation can be written as a linear function:

$$C_i = \varepsilon_i C_{i+1} + \zeta_i$$

where:

$$\varepsilon_i = \frac{-\gamma_i}{\beta_i + \alpha_i \cdot \varepsilon_{i-1}}$$

$$\zeta_i = \frac{-\alpha_i \cdot \zeta_{i-1}}{\beta_i + \alpha_i \cdot \varepsilon_{i-1}}$$

After each iteration, the gradient descent algorithm adjusts the proportions of each reaction to minimize the difference between the modeled and measured pore water concentrations and isotope ratios. The algorithm finds the best fit that minimizes the combined normalized error at each depth interval.

4.2.1.5 Calculating authigenic carbonate and aluminosilicate mineral precipitation rates

The total rates of *in situ* carbonate formation, recrystallization, and clay formation are calculated by applying the best-fitting proportions of magnesium uptake for each reaction to the magnesium

content of the respective mineral. For example, if 50% of a total magnesium uptake of 2 mmol m^{-3} y^{-1} at a given depth interval is due to authigenic carbonate precipitation, with a Mg:Ca ratio in the precipitating carbonates of 0.10, that 1 mmol m^{-3} y^{-1} of magnesium uptake due to carbonate precipitation would result in 10 mmol m^{-3} y^{-1} (1.1 grams m^{-3} y^{-1}) of $CaMg_{0.1}(CO_3)_{1.1}$.

Montmorillonite is used as the representative authigenic clay mineral for model parameterization, as it is the predominant authigenic clay formed in low-temperature marine sediments. Based on the representative formula for montmorillonite in Section 4.1, a magnesium content of 2.3 wt% is used in the calculations. So, 1 mmol m^{-3} y^{-1} of magnesium uptake due to clay formation would result in 1.0 grams m^{-3} y^{-1} of montmorillonite clay.

4.2.2 *Site Descriptions*

4.2.2.1 Hemipelagic Sites

The scientific ocean drilling sites used in this study span a range of depositional environments, including locations characterized by hemipelagic and pelagic sedimentation studied as part of the Ocean Drilling Program (ODP), Integrated Ocean Drilling Program (IODP), and the Indian National Gas Hydrate Program (NGHP) (Figure 4.1). IODP Site C0002, NGHP Site 18, and IODP Site U1378 are located on the Nankai, southeast Indian, and western Costa Rican margins, respectively (Collett et al., 2008; Kinoshita et al., 2009a; Vannucchi et al., 2012a). They are characterized by rapid sedimentation rates (8 – 52 cm/ky) of hemipelagic material in their upper lithologic units. These sites are dominated by lithogenic material, averaging 80 – 95 weight% (wt%) of the dry bulk sediment. The average organic carbon content of the sediment at these sites ranges from 0.5 – 2 wt%. Sites 1012 and 1082 are located in coastal upwelling regions on the Californian and southwest African margins, respectively (Lyle et al., 1997; Wefer et al.,

1998). Hemipelagic sedimentation rates at these sites are 6.5 at Site 1012 and 14 cm/ky at Site 1082, with lithogenic material composing approximately 55 wt% at Site 1012, and 60 wt% at Site 1082. Average organic carbon contents of the sediment at Sites 1012 and 1082 are high, with approximately 3.1 and 3.5 wt%, respectively.

4.2.2.2 Pelagic Sites

Site 1086 is located in coastal upwelling region on the southwest African margin (Wefer et al., 1998). Sedimentation at Site 1086 is dominantly pelagic, with a 1.6 cm/ky sedimentation rate, composed of approximately 80% nannofossil ooze, 20 wt% lithogenic material, and 0.9 wt% organic carbon. ODP Site 984 is located on the Bjorn drift on the eastern flank of the Reykjanes Ridge (Jansen et al., 1996). The site is characterized by rapid pelagic sedimentation (12 cm/ky) in the upper sediment section. The sediment is primarily composed of lithogenic material (90%), with about 10 – 15 wt% biogenic carbonate. ODP Site 1171 is a carbonate platform site located on the South Tasman Rise, with a sedimentation rate of approximately 1.4 cm/ky (Exon et al., 2001). Sediments in the upper section at this site are approximately 90% pelagic carbonates, with a minor lithogenic component. ODP Site 925 is located on the Ceara Rise in the western Atlantic basin (Curry et al., 1995). Sedimentation at this site is low (2.9 cm/ky), and primarily composed of pelagic carbonates (55%) and lithogenic material (40%). Organic carbon concentrations in the upper sections at Sites 984, 1171, and 925 are low, averaging 0.3, 0.5, and 0.01 wt%, respectively.

4.2.3 *Ocean Drilling Data*

Measurements of sediment porosity, biostratigraphic age, and pore water concentrations of magnesium, calcium, and ammonium were compiled from the Janus (http://www-odp.tamu.edu/database), LIMS (http://web.iodp.tamu.edu/LORE), and J-CORES (http://sio7.jamstec.go.jp) databases that house drilling data from the ODP and IODP. Additional data were compiled from the NGHP Expedition 01 Initial Reports (Collett et al., 2008) and Solomon et al. (2014). This dataset includes data collected with both the JOIDES Resolution and D/V CHIKYU.

Pore water magnesium isotope ratios from IODP Sites U1378/U1380, and C0002, and NGHP Site 18 were analyzed using the methods described in Berg et al. (2018, submitted). Analyses were conducted at the University of Washington Isotope Laboratory via multi-collector inductively-coupled plasma mass spectrometry (MC-ICPMS) after chromatographic separation. Magnesium isotopic data are reported in delta (δ) notation in per mil relative to DSM3 standard (Galy et al., 2003). Repeated analyses indicate data reproducibility is ±0.06‰ (2σ) or better for δ^{26}Mg, far below the natural variations observed in the pore water profiles. All measured magnesium isotope analytical data are provided in the Supplementary Information of Berg et al., 2018. Pore water magnesium isotope values from ODP Sites 925, 984, 1012, 1082, 1086, and 1171 were obtained from previous studies, and the collection and analytical methods can be found in their respective publications (Chanda and Fantle, 2017; Higgins and Schrag, 2010).

All other data, including bottom water temperatures, geothermal gradients, and lithologies were obtained from the individual site reports. Bottom water temperatures and geothermal gradients for ODP Sites 1082 and 1086 are not available, so the values from nearby Sites 1081 and 1087 are used, respectively.

4.3 RESULTS

The model fits to the magnesium concentration profiles are in agreement with the general trends at the sites (Figure 4.4). The results indicate that the greatest uptake of magnesium from pore water occurs in the upper sediment column, as would be expected for sediments and organic matter undergoing early diagenesis in the anoxic environment of the subsurface. However, discrepancies between the modeled and measured magnesium concentration profiles at some sites, such as Sites 1012 and 1082, indicate that magnesium release from the sediments into the pore water is not fully captured by the model. The discrepancies at these locations may be caused by other mineral-rock reactions, which can affect the shape of the magnesium profiles. For example, dissolution of high-magnesium aluminosilicates has been hypothesized to increase magnesium concentrations in marine pore water in some regions (Wallmann et al., 2008), however the mineralogies at Sites 1012 and 1082 do not suggest this as a likely process. Alternatively, the discrepancies may be caused by desorption of magnesium driven by other processes that affect equilibrium cation exchange, such as increased formation of $MgCO_3^0$ ion pairs in zones of high alkalinity (von Breymann et al., 1990a). Another possibility is that non-steady state sedimentation that is not well-reflected in the biostratigraphy data has occurred over the depth interval considered within the model domain.

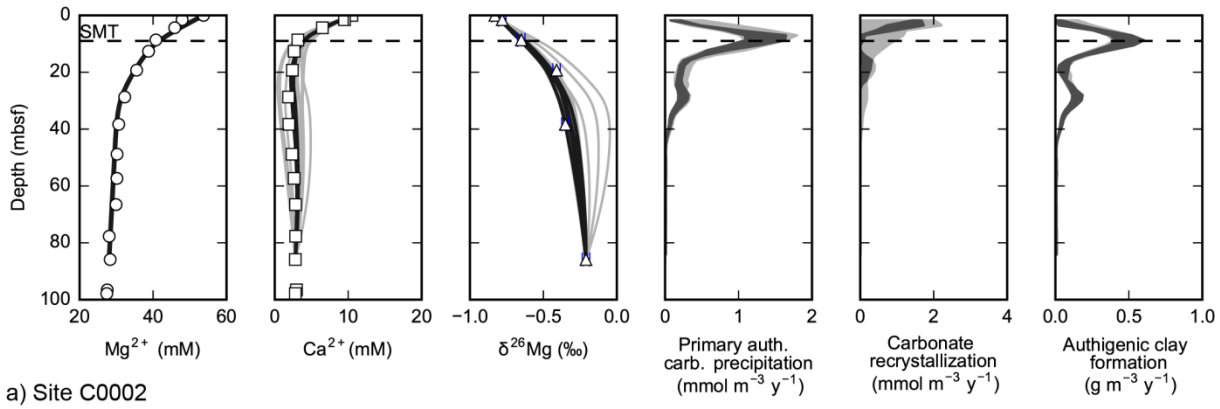

a) Site C0002

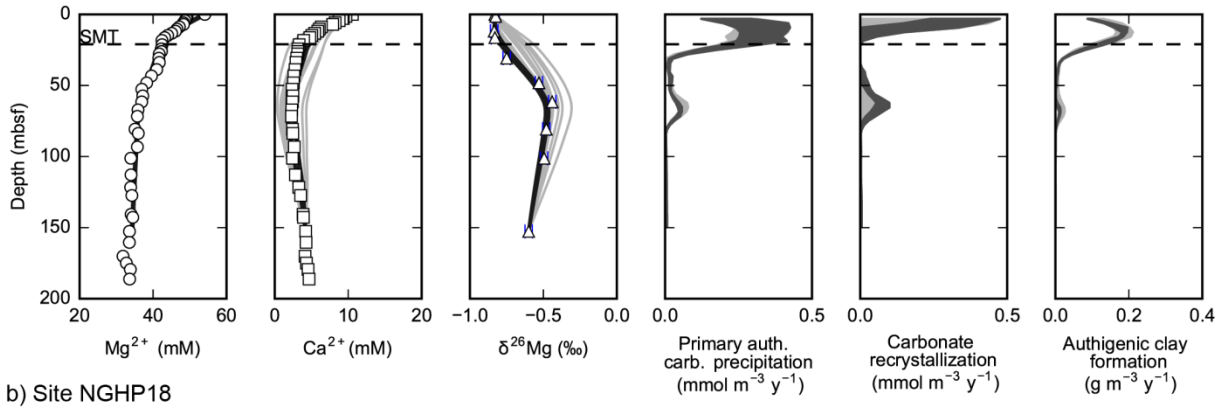

b) Site NGHP18

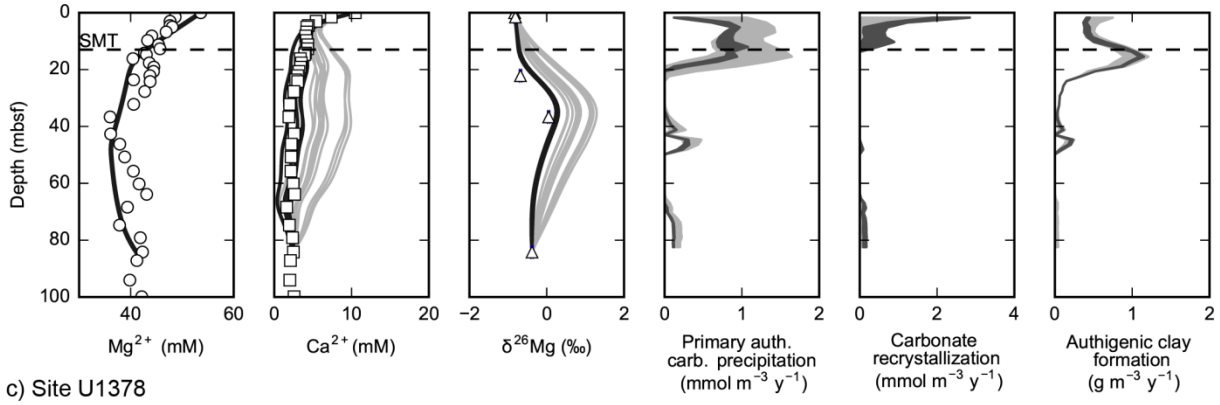

c) Site U1378

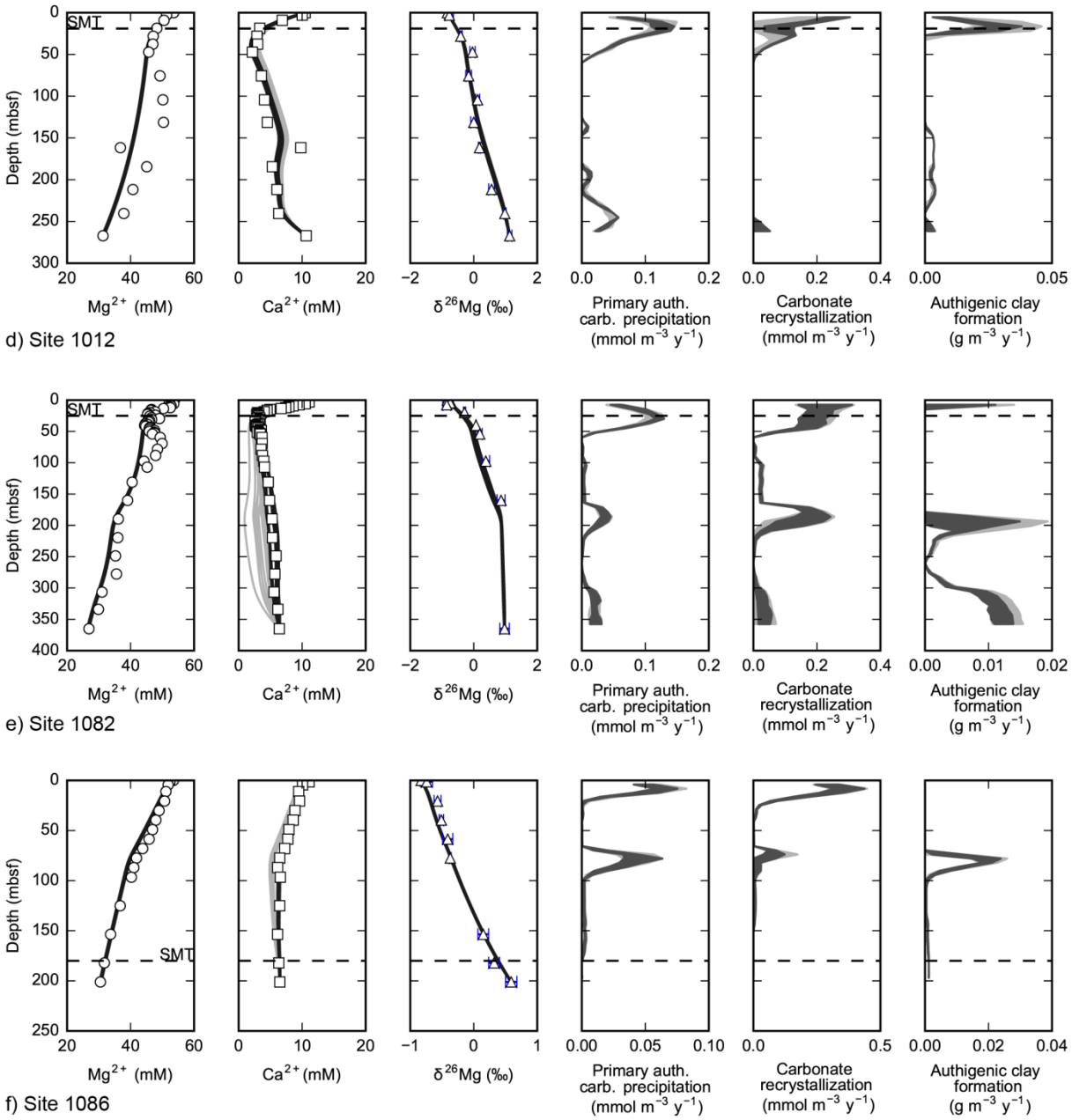
SMI
Depth (mbsf)
Mg2+ (mM)
Ca2+ (mM)
δ26Mg (‰)
Primary auth. carb. precipitation (mmol m−3 y−1)
Carbonate recrystallization (mmol m−3 y−1)
Authigenic clay formation (g m−3 y−1)
d) Site 1012
e) Site 1082
SMT
f) Site 1086

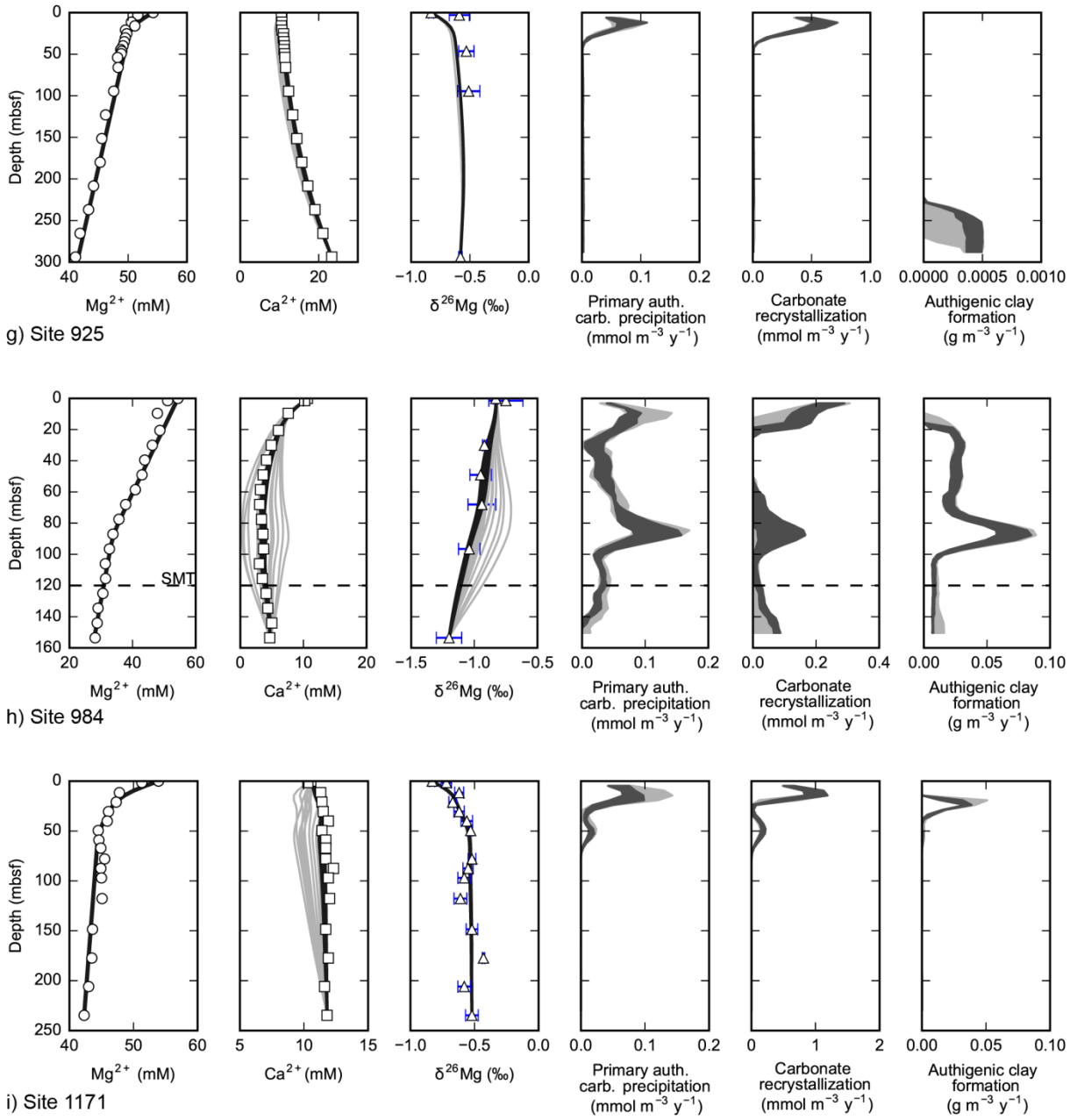

Figure 4.4 – Coupled model output. The three left-most subplots for each site show the measured pore water Mg, Ca, and δ^{26}Mg depth profiles in open circles, squares, and triangles, respectively. Error bars for Mg and Ca concentrations are smaller than symbols. Lines are the coupled fits to the measured pore water profiles (dark lines in the calcium and δ^{26}Mg profiles represent the four best-fitting combinations of reaction stoichiometries and fractionation factors, and light gray lines represent the other 12 combinations). The three right-most subplots for each

site show the full ranges of the modeled rates of carbonate precipitation, carbonate recrystallization, and authigenic clay formation, with the dark shaded areas representing the range corresponding to the four dark colored model fits in the calcium and δ^{26}Mg profiles, and the light gray shaded area represents the full range of all 16 possible combinations. The dashed horizontal lines indicate the depth of the sulfate-methane transition (SMT), where applicable.

The iterative gradient descent method provides good fits to the pore water calcium and δ^{26}Mg profiles for subsets of the reaction stoichiometry and magnesium isotopic fractionation combinations (Figure 4.4). Although the actual reaction stoichiometries are likely between the minimum and maximum values and may change with depth, at least four of the 16 combinations of minimum or maximum value combinations provide a reasonable fit to the profiles, as shown with the darker lines in Figure 4.4. The δ^{26}Mg profile fit at Site 925 underestimates the magnitude of isotopic fractionation, suggesting that the fractionation factor associated with carbonate precipitation at that site may be outside of the model parameters.

Primary authigenic carbonate precipitation rates are greatest within the upper 50 meters at all sites, with the highest rates at Sites C0002, NGHP18, U1378, and 984 (Figure 4.4). The higher rates at these sites are likely driven by increases in pore water alkalinity due to greater organic carbon burial and rates of organic carbon degradation and/or anaerobic oxidation of methane (AOM). The higher rates of authigenic carbonate precipitation near the sulfate-methane transition zone, due to AOM, is apparent in several of the profiles. The modeled rates of carbonate recrystallization are greatest in the upper section of the sediment column as well. This is partly due to the Mg:Ca distribution coefficient, with lower Mg:Ca ratios in the upper sediment column at most sites, a greater mass of carbonate is recrystallized for every mole of magnesium taken up through this process. While hemipelagic sites tend to have greater absolute rates of both primary authigenic carbonate precipitation and carbonate recrystallization, pelagic

sites and sites with greater amounts of biogenic carbonate sediment tend to have higher ratios of carbonate recrystallization to primary authigenic carbonate precipitation than hemipelagic sites. This result is expected considering the lower pore water alkalinities and greater fractions of biogenic carbonate present in pelagic sedimentary environments.

The rates of carbonate recrystallization calculated at Sites 984 and 1171 are presented in Figure 4.5. At carbonate-dominated Site 1171, the upper limit of the model results show about 11% of the carbonate recrystallized in the upper 20 meters of the sediment column, and an additional 5% recrystallization by 50 mbsf. The recrystallization rate distribution at Site 1171, with greater rates in the upper sediment column, is consistent with model results from previous studies using strontium geochemistry and calcium isotope data (Fantle, 2015; Huber et al., 2017). However, the amounts of recrystallization are about two times less than the amount of recrystallization that was estimated using those methods. For Site 984, which is dominated by lithogenic sediment, the modeled amounts of recrystallization are lower than at carbonate-dominated Site 1171. Most recrystallization at Site 984 is occurring at about 80 – 100 mbsf, resulting in about 1.5 – 4% recrystallization by 150 mbsf, which is slightly above the 1.3% recrystallization by that depth modeled using calcium isotope profiles (Huber et al., 2017). This suggests that the rates of carbonate recrystallization may be underestimated by the multicomponent model presented here in carbonate-dominated environments and potentially slightly overestimated in environments with more lithogenic material. The discrepancy from carbonate-dominated environments may be due to recrystallization of low-magnesium calcite without significant incorporation of additional magnesium in these environments, while the model is parameterized for high-magnesium calcite formation. Additional plots of cumulative authigenic carbonate formation and carbonate recrystallization for all sites are provided in Figure

C1. The cumulative amounts of authigenic carbonate and recrystallized carbonate that are modeled are well within reasonable ranges compared to the total weight percent of carbonate sediments at each site.

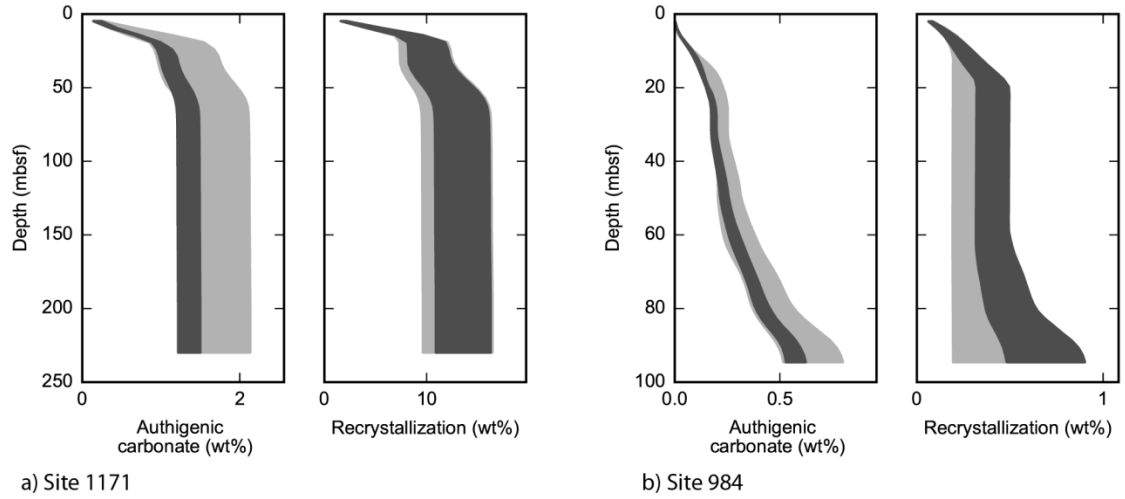

Figure 4.5. Total amounts of primary carbonate and recrystallized carbonate at a) Site 1171 and b) Site 984. The dark shaded region represents the range corresponding to the four best-fitting combinations of reaction stoichiometries and fractionation factors, and light gray region represents the full range of all 16 possible combinations. Units are in weight percent of dry bulk sediment.

As with carbonate precipitation and recrystallization, modeled rates of authigenic clay formation tend to be greatest in the upper 50 meters of the sediment column, although there is more variability with depth (Figure 4.4). Maximum rates range between 0.2 – 1 g m^{-3} y^{-1} at Sites C0002, NGHP18, U1378, and 984, and are about an order of magnitude lower at Sites 1012, 1082, 1086, and 1171. Site 925 exhibits the lowest overall rates, with greater rates in the lower section that are about two orders of magnitude less than the highest rates at other pelagic sites. The greater variability of the depth distribution of authigenic clay formation rates is consistent with a greater effect of the source minerology on this process than for carbonate precipitation,

which is driven more by biogeochemical processes associated with organic matter degradation. The total modeled amounts of authigenic clay formation at each site are presented in Figure 4.6. To provide a conservative estimate of the amounts of authigenic clay being formed, the amounts are calculated assuming incongruent weathering of a magnesium-free mineral to montmorillonite. The modeled abundance of authigenic clay formed at the lower limit of the model domains ranges from about 1 kg m^{-3} to over 80 kg m^{-3}. These amounts correspond to between about 0.1% to 8% of the dry bulk weight of the sediments (Figure C1). At the hemipelagic continental margin sites (C0002, NGHP18, U1378, 1012, and 1082), the modeled authigenic clay abundance ranges from about 1% to 5% at the lower limit of their model domains. The pelagic sedimentation sites (925, 984, 1086, and 1171) generally have much lower rates of authigenic clay formation, although the slower sediment accumulation rates result in Sites 984 and 1171 having similar total abundances of authigenic clay as the hemipelagic margin sites. The authigenic clay abundances at the lower limit of the model domains for these pelagic sites range from approximately 0.1% to 2%.

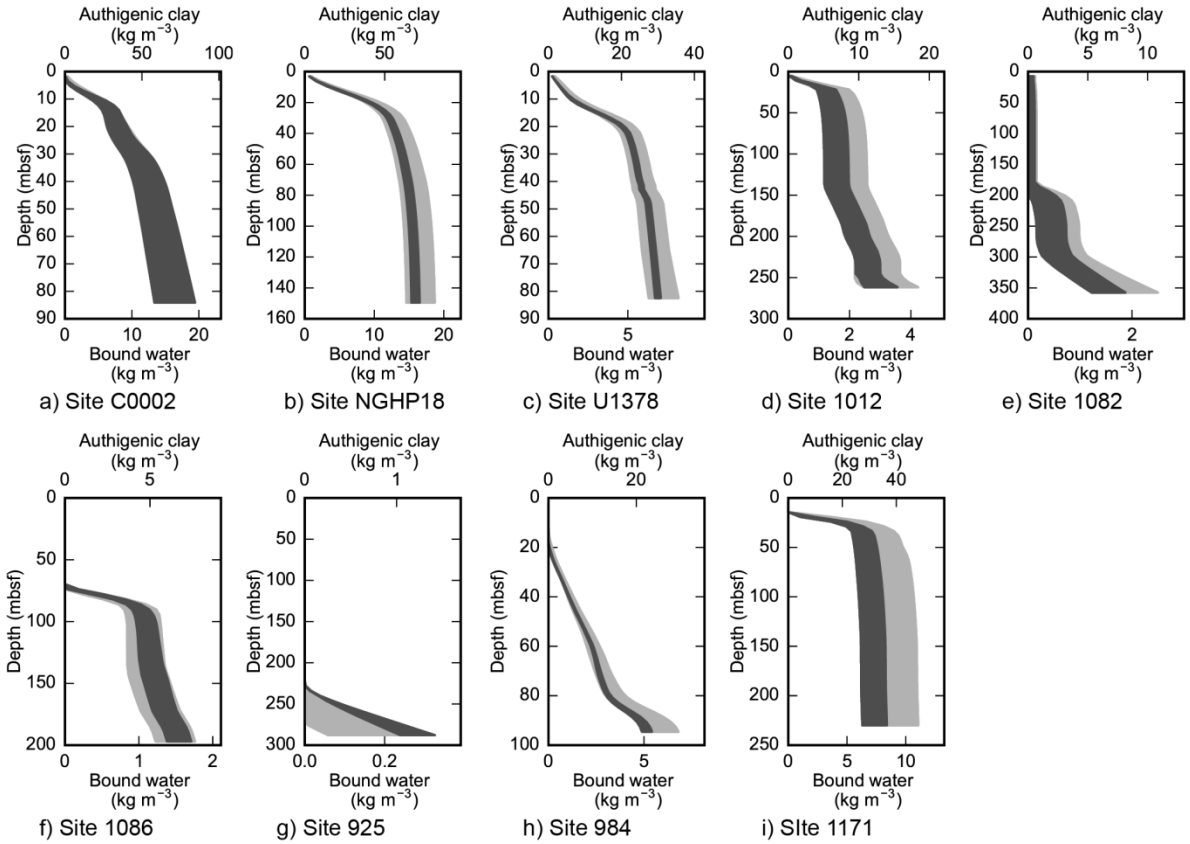

Figure 4.6. Ranges in total authigenic clay and associated bound water at all sites. The top row of figures (a – e) are sites with hemipelagic sedimentation, and the bottom row (f – g) are sites with pelagic sedimentation. The dark shaded region represents the range corresponding to the four best-fitting combinations of reaction stoichiometries and fractionation factors, and light gray region represents the full range of all 16 possible combinations.

4.4 DISCUSSION

4.4.1 *Authigenic clay formation in the geologic water and oceanic ^{18}O budgets*

Measurements on solid-phase marine sediments suggest that the incongruent weathering of the most highly-weatherable material such as volcanic glass fragments predominantly takes place close to the sediment water interface in the pelagic environment (Dunlea et al., 2017). With the slow burial rates of volcanogenic material, authigenic clay fractions at sites that are

predominantly volcanogenic material are shown to reach up to 40 wt% within the upper meter of sediment, with the variability in this initial alteration typically being greater than the additional alteration that occurs deeper in the sediment column, preventing the evaluation of further alteration in the deep subseafloor (>1 meter below seafloor). However, the results of the multicomponent model in this study suggest that authigenic clay formation does take place in the deep subseafloor at levels that may be difficult to detect with solid-phase analyses. These deeper-formed authigenic clays may be significant to long-term geochemical cycles if their formation is widespread and they are predominantly cation-rich clays, such as smectites.

The modeled abundances presented here indicate that authigenic clay formation in deep marine sediments is indeed widespread in both pelagic and hemipelagic sedimentation regimes, with higher formation rates and greater total amounts of authigenic clay generally occurring on continental margins characterized by hemipelagic sedimentation. With most of the global sedimentation taking place on the continental margins, and authigenic clay abundances up to 8 wt%, the total rate of authigenic clay formation in the deep subsurface could amount to the equivalent of a few percent of the total sediment input into the ocean from rivers.

In addition to being cation-rich, the smectite clays that form in the low-temperature marine environment have combined structural and interlayer water contents of up to 25 wt%, much more than the 5 wt% water content of average detrital clay that is more commonly formed on continents and delivered to ocean basins (Gieskes and Lawrence, 1981; Griffin et al., 1968; Peacock, 1990). The amount of structural water associated with authigenic clays formed in the deep subsurface at each site is shown in Figure 4.6, ranging from about 0.2 to 15 kg m^{-3}, which amounts to about 0.02 to 1.5 wt% of the dry bulk sediment.

These water contents become relevant when considering the fractionation of oxygen isotopes of water during incorporation into authigenic clays at low temperatures. During authigenic clay formation, water is incorporated into the crystal structure and interlayers of the minerals with a preference for $H_2{}^{18}O$ over $H_2{}^{16}O$, resulting in a fractionation of the pore water oxygen isotopes (Hoefs, 1980). The magnitude of fractionation in marine sediments (+10‰ to +30‰) is significantly larger than the fractionation during hydration of the oceanic crust or clays formed on land, due to the lower temperatures of reaction in the sediment. Interpretations of paleo-oceanographic reconstructions of $\delta^{18}O$ of seawater on geologic timescales (not associated with orbital variations) are based on the known geologic processes controlling H_2O uptake (Jaffrés et al., 2007; Wallmann, 2001). However, the contribution of *in situ* hydrous aluminosilicate formation in marine sediments is an unconstrained sink for $H_2{}^{18}O$ that adds additional uncertainty to interpretations of the paleo-oceanographic record of the $\delta^{18}O$ values of seawater. For authigenic clays composing an average of just 2% of the dry bulk weight of global marine sediment, with an average 20 wt% structural water that has an average $\delta^{18}O$ value of +30‰, authigenic marine clays would account for an ^{18}O output from the ocean of 0.2×10^9 mol y^{-1}. This sink for ^{18}O from the ocean is equivalent to that calculated for the net fixation of water in continental weathering products (Wallmann, 2001), suggesting that the formation of authigenic clays in marine sediments should be included in ^{18}O budgets of the ocean on geologic timescales.

4.4.2 *Authigenic clay formation and water input to subduction zones*

Water that is structurally-bound in both detrital and authigenic clays is effectively sequestered in abyssal sediments until reaching high temperatures and pressures that are characteristic of

subduction zones (Moore and Vrolijk, 1992). The interlayer water of clays in abyssal ocean sediments may be released during metamorphic alteration of the minerals as they are subducted, contributing to increases in pore pressures and changes to the frictional properties along the plate boundary. This release of interlayer water is hypothesized to be a controlling factor in fault slip behavior and the seismicity of many subduction zones (Moore and Saffer, 2001; Saffer and Tobin, 2011). In addition, other structurally-bound water may persist to greater depths where further metamorphic alteration occurs, contributing to water delivery to the volcanic arc and mantle e.g. (Ernst, 1990; Peacock, 1990).

The structural water content of global subducting sediment (GLOSS) has been estimated to be about 7 wt% (Plank and Langmuir, 1998). Assuming on average 2% of the bulk dry weight of pelagic sediments are authigenic clays that have a structural water content of ~20 wt%, authigenic clays formed in the deep subsurface could account for approximately 0.4 wt% of the dry bulk weight of subducting sediment, or about 6% of the structural water in subducting sediment. These values would increase further when considering the contribution of authigenic clays formed in the shallow subsurface, near the sediment-water interface.

4.4.3 *Authigenic carbonate precipitation and carbonate recrystallization*

The burial of calcium carbonate in marine sediments accounts for approximately 80% of the total carbon removed from the Earth's surface on geologic timescales (Derry, 2014; Wedepohl, 1995). This carbonate sink also affects other elements such as calcium, magnesium, and strontium. The fraction of biogenic calcium carbonate deposited on the seafloor, versus the fraction that precipitates authigenically in marine sediments has implications for several chemical cycles in the ocean, due to the differences in the chemical composition of biogenic and authigenic

carbonates (Milliman, 1974). In addition, it may be an important factor in the oceanic carbon isotope cycle and for interpretations of the carbon isotope record of marine dissolved inorganic carbon (Mitnick et al., 2018; Schrag et al., 2013).

Previous studies estimated authigenic $CaCO_3$ formation accounts for about 10% of the total carbonate accumulation in the abyssal ocean, or about 4% of total carbonate formation in the ocean (Milliman, 1993; Sun and Turchyn, 2014). These estimates have been calculated using pore water calcium concentration profiles, assuming formation of pure calcium carbonate and excluding the continental shelves. However, inorganically-precipitated authigenic carbonates in marine sediments tend to be high in Mg, ranging from high-Mg calcites, with ~10 – 20% $MgCO_3$, to dolomites with ~50% $MgCO_3$ (Milliman, 1974). So, assuming pure $CaCO_3$ to estimate carbonate formation rates may result in a ~11 – 100% underestimation of the authigenic carbonate alkalinity sink. In addition, other forms of carbonate in marine sediments, such as siderite and manganese carbonates can be abundant deeper in the sediment column, potentially affecting the carbon budget on longer timescales through sequestration of the more deeply-sourced remineralized carbon.

Calculations of primary authigenic carbonate precipitation rates can also be affected by consideration of other *in situ* processes in marine sediments that control the concentrations of calcium in pore waters. An analysis of the net rates of calcium uptake based solely on diffusion of calcium from the overlying ocean versus the gross rates of calcium uptake that consider *in situ* processes at each site is presented in Figure 4.7. The net rates are calculated solely from the steady-state reactive transport modeling of the pore water calcium profile, which considers only calcium sourced from diffusion into the sediments. The gross rates are calculated accounting for the additional calcium being sourced from cation exchange, aluminosilicate weathering, and

carbonate recrystallization to higher-magnesium carbonates. Equilibrium cation exchange results in a release of sediment-adsorbed calcium as pore water calcium is sequestered in precipitating carbonates, requiring a greater rate of calcium uptake for a given decrease in pore water concentrations. Incongruent weathering of calcium-bearing aluminosilicates in the marine environment also results in an additional release of calcium to pore waters as authigenic clays are formed. Finally, replacement of some of the $CaCO_3$ with $MgCO_3$ in the crystal structure of carbonates during recrystallization releases that calcium into the pore water as well (Walter et al., 1993). All of these *in situ* processes act to mask the full rate of calcium uptake into authigenic carbonates when calculated solely using a steady-state reactive transport model of the pore water calcium profiles. This is demonstrated at all sites presented in Figure 4.7, where the total rates of calcium uptake in the upper sediment column are greater than the net rates by a factor of at least 1.5 to 2, demonstrating that the total amount of authigenic carbonate formation in the deep ocean is greater than the 1 Tmol y^{-1} calculated using pore water calcium profiles, by at least 1.5 – 2 times (Sun and Turchyn, 2014). This authigenic carbonate sink in the upper sediment column can affect the dissolved inorganic carbon budget of the ocean on timescales similar to its ~10^5 year residence time in the ocean by reducing the diffusional flux into the overlying ocean.

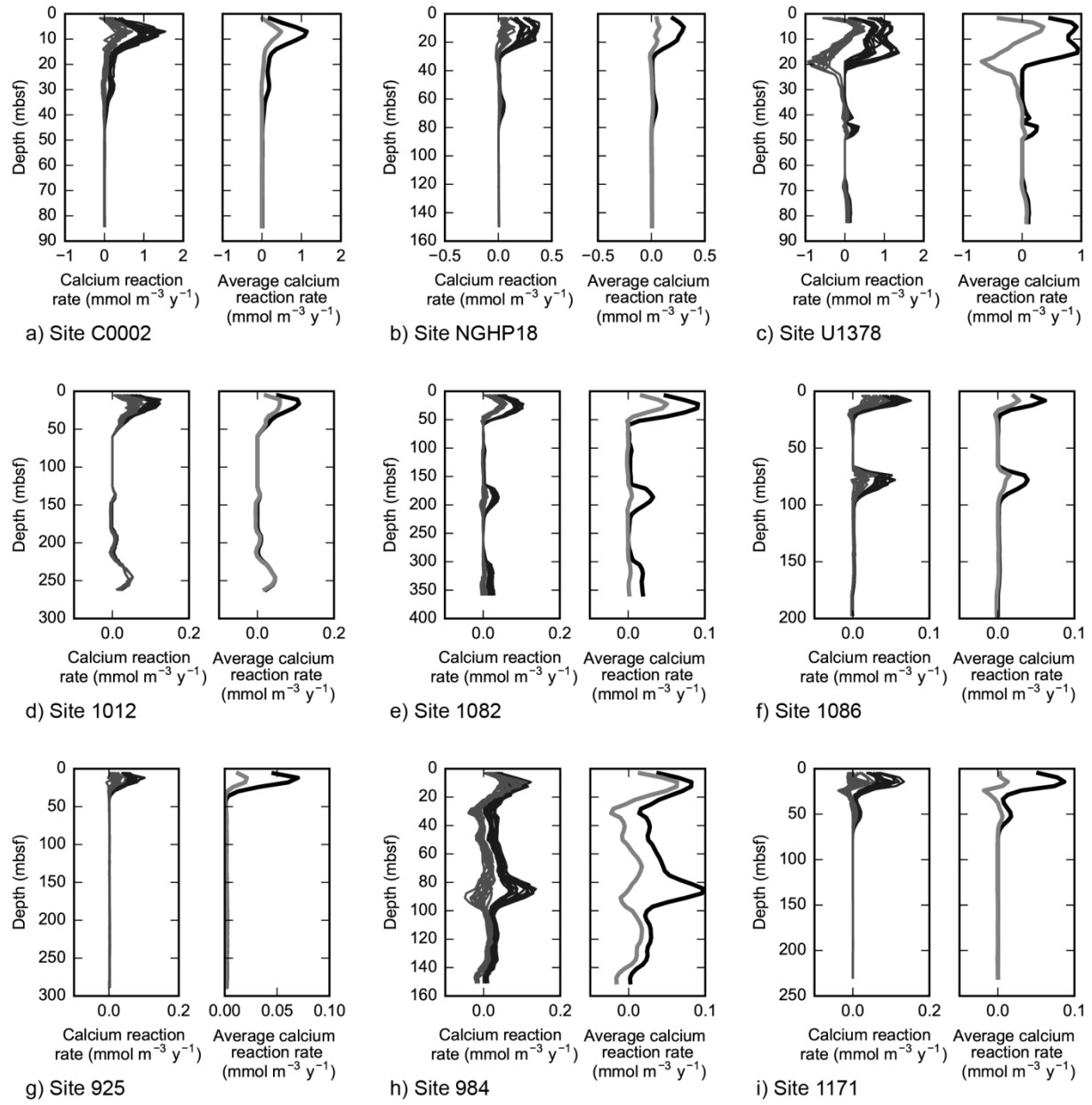

Figure 4.7. Calcium uptake (positive values) or release (negative values) rates at each site, with gross rates (dark lines) and net rates (light gray lines) of all 16 model combinations shown in left plot for each site, and the average of the 16 gross and net rates shown in the right plot for each site.

The authigenic carbonate sink near the sediment-water interface can also affect the $\delta^{13}C$ balance of the ocean on geologic timescales. The carbon isotope record of DIC in the ocean is

interpreted as a balance between inputs, and sinks of organic carbon ($\delta^{13}C_{org}$) and carbonate minerals ($\delta^{13}C_{carb}$). This relationship can be described by the equation:

$$\delta^{13}C_{in} = \delta^{13}C_{org} * f_{org} + \delta^{13}C_{carb} * (1 - f_{org})$$

Changes in the $\delta^{13}C$ record through geologic time are typically interpreted to be due to variations in the relative fractions of organic carbon burial (f_{org}) versus carbonate carbon burial (Hayes et al., 1999; Knoll et al., 1986). However, as diagenesis occurs, some of the organic carbon is degraded and ultimately transformed to DIC in the pore waters, where it can precipitate and be sequestered as authigenic carbonates. Because of this additional capture of inorganic carbon that has an isotopic value different than that of biogenic carbonate, the ratio of authigenic to biogenic carbonate burial is hypothesized to be an important factor in controlling the carbon isotopic record (Schrag et al., 2013). The formulation for this model is described by:

$$\delta^{13}C_{in} = \delta^{13}C_{org} * f_{org} + \delta^{13}C_{bc} * f_{bc} + \delta^{13}C_{ac} * f_{ac}$$

The precipitation of authigenic carbonates would affect the $\delta^{13}C$ record because biogenic carbonates have $\delta^{13}C_{bc}$ values similar to that of seawater DIC, but authigenic carbonates typically have lower values of $\delta^{13}C_{ac}$, especially when formed in the upper sediment column above the methanogenic zone e.g. (Solomon et al., 2014; Teichert et al., 2014; Torres and Kastner, 2008). The highest modeled rates of authigenic carbonate formation at every site, presented in Figure 4.4, are in the upper sediment column at or above the sulfate-methane transition where isotopically-light methane is being oxidized, creating isotopically-light DIC. Thus, these results

suggest that not only are more authigenic carbonates formed than previously calculated, but also that isotopically-light authigenic carbonate formation has a greater role in the ^{13}C cycle of the ocean than previously estimated. Precipitation of other forms of carbonate deeper in marine sediments, such as siderite and manganese carbonates could also affect the carbon isotope budget on longer timescales through sequestration of isotopically heavier carbon from microbial methanogenesis and deeper-sources.

In addition to the effect of primary authigenic carbonate formation, recrystallization of biogenic carbonates can also affect the oceanic ^{13}C cycle. During recrystallization, carbonates are dissolved *in situ* and reprecipitated, with the CO_3^{2-} in the reprecipitated carbonates sourced from the pore water. As the results in Figure 4.4 indicate, carbonate recrystallization rates are generally greatest in the upper sediment column, and may be greater than primary authigenic carbonate precipitation in some environments, particularly in carbonate-dominated pelagic sediments. As with primary authigenic carbonate precipitation, the recrystallized carbonates above the SMT typically have a lower $\delta^{13}C$ value due to the lower isotopic values of the pore water in the upper sediment column. The $\delta^{13}C$ values of the carbonates after recrystallization are dependent on the extent of dissolution prior to recrystallization and the $\delta^{13}C$ of the pore water. In this way, recrystallization of carbonates can affect the long-term $\delta^{13}C$ record by replacing CO_3^{2-} in carbonates with CO_3^{2-} that has lower $\delta^{13}C$ values than the original biogenic carbonate that was deposited. Other geochemical constraints are consistent with the highest rates of recrystallization in the upper sediment column, and calculate even greater rates than are modeled here (Fantle, 2015; Huber et al., 2017). Although the large range in modeled recrystallization rates lends uncertainty to the implications, the modeled rates provide evidence that carbonate recrystallization is a significant process in the ^{13}C cycle in marine sediments, and potentially in

the oceanic ^{13}C cycle on geologic timescales. However, more work needs to be done to find consistency between approaches to calculating carbonate recrystallization using calcium isotope data and strontium data, as well as other methods such as the multicomponent model presented here.

4.5 CONCLUSIONS

The multicomponent model described in this study provides first-order insight into the total rates of authigenic mineral formation reactions based on pore water magnesium and calcium concentrations, and magnesium isotope ratios. The results suggest that authigenic carbonate precipitation and recrystallization are important processes in the oceanic carbon cycle on geologic timescales, affecting both the alkalinity and ^{13}C cycles in the ocean to a greater degree than previously recognized. The modeled rates of authigenic clay formation are also high enough to affect geochemical cycles on geologic timescales, such as the oceanic $H_2{}^{18}O$ cycle, as well as contributing up to 6% of the mineral-bound water delivery to subduction zones. The model results also indicate a large disparity between net rates and total rates of solute uptake in marine sediments, caused by *in situ* weathering and recrystallization reactions that are significant sources of solutes within the sediment column. These large disparities demonstrate the need for quantifying total rates of solute uptake when estimating authigenic mineral formation rates in marine sediments.

Chapter 5. CONCLUSIONS

With marine sediment covering the majority of Earth's surface, the chemical reactions that occur within those sediments can drive chemical fluxes large enough to be important in several global geochemical cycles. Most of these reactions are ultimately driven by microbially-mediated organic matter oxidation and fermentation, which alter the alkalinity, pH, and redox potential of the pore water away from seawater values. These changes in pore water chemistry drive further mineral precipitation and weathering reactions within the sediment column, which affect alteration and preservation of marine sediments, and regulation of long-term climate through burial of carbon. In addition, these changes in pore water chemistry create chemical gradients between pore water and the overlying ocean, driving diffusive fluxes between the two reservoirs. Through this diffusive flux, as well as through advective exchange, the reactions that occur in marine sediments affect ocean chemistry, making quantification of these reactions on a global scale important for a full understanding of geochemical cycles in the ocean. On the individual site scale, characterization of the reactions is critical for identifying the controlling processes and for interpretation of how these reactions may alter sediment properties and affect other geochemical cycles during diagenesis.

5.1 GEOCHEMICAL REACTIONS IN MARINE SEDIMENT ON THE GLOBAL SCALE

Quantification of global chemical cycles for major elements such as magnesium require surveys of the potentially significant sources and sinks of these elements to and from the ocean. The research presented Chapter 2 addresses the exchange of magnesium and magnesium isotopes

across the sediment-water interface. As part of this research, the most accurate estimate of global magnesium flux into marine sediments to date is calculated and included as part of the most comprehensive oceanic magnesium budget that has been compiled. By quantifying the known sources and sinks of magnesium, this new compilation estimates that the magnitude of the remaining major magnesium sink, the low-temperature ridge flank hydrothermal circulation, is approximately 75% of the river input of magnesium. Overall, the new compilation offers greater insight into the present-day magnesium cycle, and provides a benchmark for models and interpretations of the paleo-oceanographic record.

The more surprising finding is in the magnesium isotope results, which indicate that the isotopic composition of the low-temperature ridge flank sink is found to be nearly identical to seawater, with no significant net isotopic fractionation. The small magnitude of the net fractionation is likely a result of the combined effect of the opposing fractionations associated with clay formation and carbonate formation in the basement. A low net fractionation during low-temperature hydrothermal circulation suggests that the marine δ^{26}Mg record is primarily controlled by variations in continental weathering, biogenic carbonate formation, particulate organic carbon burial, and diagenetic processes in marine sediment. Additional factors that may be important controls on the δ^{26}Mg record in the past include the relative preservation rates of foraminifera tests versus coccoliths, and the relative amount of carbonate precipitation versus clay formation during low-temperature ridge flank circulation. Further paleo-oceanographic and paleoclimatic studies should consider these factors when interpreting variations in the magnesium isotope ratio in the ocean in the past.

5.2 GEOCHEMICAL REACTIONS IN MARINE SEDIMENT ON THE SITE SCALE

The specific geochemical reactions that control the solute concentrations in pore waters and solute fluxes across the sediment-water interface can be investigated in greater detail on the individual site scale than on the global scale. Chapters 3 and 4 investigate the reactions occurring in the sediment column at specific ocean drilling sites from a range of environments. Chapter 3 investigates the reactions controlling magnesium, calcium, and magnesium isotopes in marine sediments, while Chapter 4 quantifies the processes controlling the release of bromine into pore water during microbial dehalogenation of organic matter.

The multicomponent reactive-transport model described in Chapter 3 provides first-order insight into the total rates of authigenic mineral formation reactions in marine sediments, including the reactions that are driving the magnesium fluxes described in Chapter 2. The model addresses the formation of authigenic clays and total formation of authigenic carbonates in marine sediments. These two mineral formation reactions are potentially of major importance in global oceanic geochemical cycles, but have not been well quantified due to the difficulties in solid-phase measurements. The results suggest that authigenic clay formation and carbonate precipitation affect the alkalinity and ^{13}C cycles in the ocean to a greater degree than previously recognized. The new model also suggests that rates of authigenic clay formation are high enough to affect the oceanic $H_2{}^{18}O$ cycle on geologic timescales, and to contribute to the mineral-bound water delivery to subduction zones.

Focusing more on biogeochemical reactions, the combination of measurements, experiments, and numerical modeling described in Chapter 4 address the rates of organbromine respiration, which have been hypothesized to be a significant source of energy for the deep

biosphere. The results provide an upper limit constraint on the rates of organobromine respiration at several continental margin sites. The modeled bromide production rates indicate that the rates of bromide production decrease with depth, decreasing to near zero where solid phase bromine concentrations reach a minimum. The modeling approach quantifies the total rate of debromination from all potential pathways, including organobromine respiration, fermentation, fortuitous debromination through co-metabolic processes or direct cofactor catalysis, and abiotic reaction, thus providing an upper limit to any of these pathways. The results indicate that the maximum integrated rates of organobromine respiration in the sediment column are at least an order of magnitude lower than sulfate reduction and several orders of magnitude lower than methanogenesis, but could still be an important niche energy source for some microbes.

5.3 FURTHER ADVANCEMENT IN QUANTIFYING MARINE GEOCHEMICAL CYCLES

In addition to presenting new insights in geochemical cycling in the ocean and modeling tools for diagenesis within marine sediments, this dissertation more broadly emphasizes the importance of data quality and uncertainty estimates for quantitative marine geochemistry research. Numerical modeling can be a powerful tool to use for quantification of diagenetic processes, but only in combination with high-quality data that have known error bounds. Only with known error bounds can the uncertainty of model results be quantified and evaluated. The uncertainties of any estimates based on modeling are critical for interpretation of the results and the information they provide about actual physical processes. For example, when calculating small solute fluxes using solute concentration profiles, the propagation of the measurement error may result in the calculated flux falling outside of reasonable limits, or in a reversal of the flux

altogether. In these cases, quantification of the uncertainty bounds are critical for interpreting the experimental results and the insights into the physical processes under investigation.

Large datasets that represent a collection of data from many separate research projects are becoming increasingly available, and provide a rich resource for new discoveries that require data from a diverse range of environments or extensive spatial coverage. These datasets offer further opportunities for research beyond the objectives of the individual research studies which contribute their data. But while these large datasets are valuable, they are commonly lacking co-located uncertainty estimates and standardization of records. Standardization of data and measurement uncertainties are critical in studies such as those detailed in this dissertation that rely on large amounts of data to quantify large-scale processes. With the increase in available data in ocean research, it will be increasingly important for organizations that maintain data repositories to design easily-accessible databases with priority placed on standardization of data formats and co-location of uncertainty estimates with measurement data.

While the research presented in this dissertation is based largely on scientific ocean drilling data, further discoveries related to the global-scale chemical exchange between the seafloor and the ocean may be made across depth scales and geographic areas where seafloor drilling does not have adequate coverage. For some solutes that have active reaction zones closer to the sediment-water interface than those sampled during drilling, short core data can provide greater insight into the cycling of chemicals between the subsurface and the ocean. A large amount of short core data exist, but are not housed within a common, easily-accessible repository with standardized data formats. For that reason, the work involved with collecting, compiling, cleaning, and performing quality control on short core data would be extensive, but the resulting dataset would be of high value to the field of global geochemical cycles.

One of the environments that contains the most opportunity for large-scale research using a compilation of short core data are the continental shelves. With the high sedimentation and organic carbon burial rates on the continental shelves in the modern environment, the rates of biogeochemical cycling are typically much higher than in deeper ocean environments farther from the coastlines. Because of these higher rates of reaction, the shelves are likely a major contributor to geochemical cycles in the ocean during sea-level high-stands such as today, and should be considered when compiling global oceanic chemical budgets. With further data compilation, standardization, and modeling, further discoveries remain to be made in this and other areas of ocean research.

BIBLIOGRAPHY

Amante C. and Eakins B. W. (2009) ETOPO1 1 arc-minute global relief model: procedures, data sources and analysis, NOAA Technical Memorandum NESDIS NGDC-24. National Geophysical Data Center, NOAA.

Anderson B. W., Coogan L. A. and Gillis K. M. (2014) Fluid seepage velocities through marine sediments constrained by a global compilation of interstitial water SO_4^{2-}, Mg^{2+}, and Ca^{2+} profiles. *Journal of Geophysical Research: Solid Earth* **119**, 6823-6840.

Anderson R. N., Langseth M. G. and Sclater J. G. (1977) The mechanisms of heat transfer through the floor of the Indian Ocean. *J. Geophys. Res.* **82**, 3391-3409.

Aulenta F., Beccari M., Majone M., Papini M. P. and Tandoi V. (2008) Competition for H_2 between sulfate reduction and dechlorination in butyrate-fed anaerobic cultures. *Process Biochemistry* **43**, 161-168.

Baker P., Kastner M., Byerlee J. and Lockner D. (1980) Pressure solution and hydrothermal recrystallization of carbonate sediments—an experimental study. *Mar. Geol.* **38**, 185-203.

Baker P. A., Gieskes J. M. and Elderfield H. (1982) Diagenesis of carbonates in deep-sea sediments; evidence from Sr/Ca ratios and interstitial dissolved Sr (super 2+) data. *J. Sediment. Res.* **52**, 71-82.

Baker P. A. and Kastner M. (1981) Constraints on the formation of sedimentary dolomite. *Science* **213**, 214-216.

Beaumais A., Teagle D. A., James R. H., Harris M., Pearce C. R., Milton J. A., Cooper M. J. and Alt J. C. (2017) Magnesium isotope composition of the altered upper oceanic crust at ODP Holes 504B and 896A, Costa Rica Rift, EGU General Assembly Conference Abstracts, p. 18056.

Berg R. D. and Solomon E. A. (2016) Geochemical constraints on the distribution and rates of debromination in the deep subseafloor biosphere. *Geochim. Cosmochim. Acta* **174**, 30-41.

Berg R. D., Solomon E. A. and Teng F.-Z. (2018) The role of marine sediments in the modern oceanic magnesium cycle (submitted).

Berner E. K. and Berner R. A. (2012) *Global environment: water, air, and geochemical cycles*. Princeton University Press.

Berner R. A. (1980) *Early Diagenesis: A Theoretical Approach*. Princeton University Press.

Berner R. A. (1982) Burial of organic carbon and pyrite sulfur in the modern ocean; its geochemical and environmental significance. *Am. J. Sci.* **282**, 451-473.

Biddle J. F., Fitz-Gibbon S., Schuster S. C., Brenchley J. E. and House C. H. (2008) Metagenomic signatures of the Peru Margin subseafloor biosphere show a genetically distinct environment. *Proc. Nat. Acad. Sci.* **105**, 10583-10588.

Boetius A., Ravenschlag K., Schubert C. J., Rickert D., Widdel F., Gieseke A., Amann R., Jorgensen B. B., Witte U. and Pfannkuche O. (2000) A marine microbial consortium apparently mediating anaerobic oxidation of methane. *Nature* **407**, 623-626.

Boudreau B. P. (1996) The diffusive tortuosity of fine-grained unlithified sediments. *Geochim. Cosmochim. Acta* **60**, 3139-3142.

Boudreau B. P. (1997) *Diagenetic models and their implementation*. Springer, Berlin.

Bowen H. J. M. (1966) *Trace Elements in Biochemistry*. Academic Press, London.

Bowles M. W., Mogollón J. M., Kasten S., Zabel M. and Hinrichs K.-U. (2014) Global rates of marine sulfate reduction and implications for sub–sea-floor metabolic activities. *Science* **344**, 889-891.

Broecker W. and Clark E. (2009) Ratio of coccolith $CaCO_3$ to foraminifera $CaCO_3$ in late Holocene deep sea sediments. *Paleoceanography* **24**.

Broecker W. and Yu J. (2011) What do we know about the evolution of Mg to Ca ratios in seawater? *Paleoceanography* **26**.

Burwicz E. B., Rüpke L. H. and Wallmann K. (2011) Estimation of the global amount of submarine gas hydrates formed via microbial methane formation based on numerical reaction-transport modeling and a novel parameterization of Holocene sedimentation. *Geochim. Cosmochim. Acta* **75**, 4562-4576.

Chanda P. and Fantle M. S. (2017) Quantifying the effect of diagenetic recrystallization on the Mg isotopic composition of marine carbonates. *Geochim. Cosmochim. Acta* **204**, 219-239.

Claypool G. E. and Kaplan I. (1974) The origin and distribution of methane in marine sediments. In: *Natural gases in marine sediments* (Eds. Springer. pp. 99-139.

Colberg P. J. S. (1990) Role of sulfate in microbial transformations of environmental contaminants: Chlorinated aromatic compounds. *Geomicrobiol. J.* **8**, 147-165.

Collett T., Riedel M., Cochran J., Boswell R., Presley J., Kumar P. and Sathe A. (2008) Indian National Gas Hydrate Program Expedition 01 Initial Reports. Directorate General of Hydrocarbons, Ministry of Petroleum & Natural Gas, New Delhi.

Colwell F., Matsumoto R. and Reed D. (2004) A review of the gas hydrates, geology, and biology of the Nankai Trough. *Chem. Geol.* **205**, 391-404.

Colwell F. S., Boyd S., Delwiche M. E., Reed D. W., Phelps T. J. and Newby D. T. (2008) Estimates of biogenic methane production rates in deep marine sediments at Hydrate Ridge, Cascadia Margin. *Appl. Environ. Microbiol.* **74**, 3444-3452.

Curry W. B., Shackleton N. J. and Richter C. (1995) Proc. ODP, Init. Repts, 154. Ocean Drilling Program, College Station, TX.

D'Hondt S., Jørgensen B. B., Miller D. J., Batzke A., Blake R., Cragg B. A., Cypionka H., Dickens G. R., Ferdelman T. and Hinrichs K. U. (2004) Distributions of microbial activities in deep subseafloor sediments. *Science* **306**, 2216-2221.

D'Hondt S., Rutherford S. and Spivack A. J. (2002) Metabolic activity of subsurface life in deep-sea sediments. *Science* **295**, 2067-2070.

Davis E., Hyndman R. and Villinger H. (1990) Rates of fluid expulsion across the Northern Cascadia Accretionary Prism: Constraints from new heat row and multichannel seismic reflection data. *Journal of Geophysical Research: Solid Earth* **95**, 8869-8889.

Delaney M. L. (1989) Temporal changes in interstitial water chemistry and calcite recrystallization in marine sediments. *Earth Planet. Sci. Lett.* **95**, 23-37.

Derry L. A. (2014) 12.9 - Organic Carbon Cycling and the Lithosphere. In: *Treatise on Geochemistry (Second Edition)* (Eds. H. D. Holland, K. K. Turekian). Elsevier, Oxford. pp. 239-249.

Dolfing J. (2003) Thermodynamic Considerations for Dehalogenation. In: *Dehalogenation: Microbial Processes and Environmental Applications* (Eds. M. M. Häggblom, I. D. Bossert). Springer. pp. 89-114.

Drever J., Li Y. and Maynard B. (1988) Geochemical cycles - the continental crust and the oceans. In: *Chemical Cycles in the Evolution of the Earth* (Eds. C. B. Gregor, R. M. Garrels, F. T. Mackenzie, J. B. Maynard). pp. 17-54.

Dunlea A. G., Murray R. W., Santiago Ramos D. P. and Higgins J. A. (2017) Cenozoic global cooling and increased seawater Mg/Ca via reduced reverse weathering. *Nature Communications* **8**, 844.

Dutkiewicz A., Müller R. D., O'Callaghan S. and Jónasson H. (2015) Census of seafloor sediments in the world's ocean. *Geology* **43**, 795-798.

Dzhamalov R. G. and Safronova T. I. (2002) On estimating chemical discharge into the world ocean with groundwater. *Water Resour.* **29**, 626-631.

Edwards K., Fisher A. and Wheat C. G. (2012) The deep subsurface biosphere in igneous ocean crust: Frontier habitats for microbiological exploration. *Frontiers in Microbiology* **3**.

Elderfield H. and Schultz A. (1996) Mid-ocean ridge hydrothermal fluxes and the chemical composition of the ocean. *Annual Review of Earth and Planetary Sciences* **24**, 191-224.

Ernst W. G. (1990) Thermobarometric and fluid expulsion history of subduction zones. *Journal of Geophysical Research: Solid Earth* **95**, 9047-9053.

Exon N. F., Kennett J. P. and Malone M. J. (2001) Proc. ODP, Init. Repts., 189. Ocean Drilling Program, College Station, TX

Fantle M. S. (2015) Calcium isotopic evidence for rapid recrystallization of bulk marine carbonates and implications for geochemical proxies. *Geochim. Cosmochim. Acta* **148**, 378-401.

Fantle M. S. and Higgins J. (2014) The effects of diagenesis and dolomitization on Ca and Mg isotopes in marine platform carbonates: Implications for the geochemical cycles of Ca and Mg. *Geochim. Cosmochim. Acta* **142**, 458-481.

Fehn U., Lu Z. and Tomaru H. (2006) Data report: ^{129}I/I ratios and halogen concentrations in pore water of Hydrate Ridge and their relevance for the origin of gas hydrates: a progress report. In: *Proc. ODP, Sci. Results* (Eds. A. M. Tréhu, Bohrmann, G., Torres, M.E., and Colwell F.S.). Ocean Drilling Program, College Station, TX pp. 1–25.

Fetzner S. (1998) Bacterial dehalogenation. *Applied Microbiology and Biotechnology* **50**, 633-657.

Fielman K. T., Woodin S. A., Walla M. D. and Lincoln D. E. (1999) Widespread occurrence of natural halogenated organics among temperate marine infauna. *Mar. Ecol. Prog. Ser.* **181**, 1-12.

Froelich P. N., Klinkhammer G., Bender M. L., Luedtke N., Heath G. R., Cullen D., Dauphin P., Hammond D., Hartman B. and Maynard V. (1979) Early oxidation of organic matter in pelagic sediments of the eastern equatorial Atlantic: suboxic diagenesis. *Geochim. Cosmochim. Acta* **43**, 1075-1090.

Futagami T., Morono Y., Terada T., Kaksonen A. H. and Inagaki F. (2009) Dehalogenation activities and distribution of reductive dehalogenase homologous genes in marine subsurface sediments. *Appl. Environ. Microbiol.* **75**, 6905-6909.

Futagami T., Morono Y., Terada T., Kaksonen A. H. and Inagaki F. (2013) Distribution of dehalogenation activity in subseafloor sediments of the Nankai Trough subduction zone. *Philos. Trans. R. Soc. London [Biol.]* **368**, 20120249.

Galy A., Yoffe O., Janney P. E., Williams R. W., Cloquet C., Alard O., Halicz L., Wadhwa M., Hutcheon I. D., Ramon E. and Carignan J. (2003) Magnesium isotope heterogeneity of the isotopic standard SRM980 and new reference materials for magnesium-isotope-ratio measurements. *J. Anal. At. Spectrom.* **18**, 1352-1356.

Galy A., Young E. D., Ash R. D. and Keith O'Nions R. (2000) The formation of chondrules at high gas pressures in the solar nebula. *Science* **290**, 1751-1753.

Gieskes J. M. and Lawrence J. R. (1981) Alteration of volcanic matter in deep sea sediments: evidence from the chemical composition of interstitial waters from deep sea drilling cores. *Geochim. Cosmochim. Acta* **45**, 1687-1703.

Glover D. M., Jenkins W. J. and Doney S. C. (2011) *Modeling methods for marine science*. Cambridge University Press.

Gothmann A. M., Stolarski J., Adkins J. F. and Higgins J. A. (2017) A Cenozoic record of seawater Mg isotopes in well-preserved fossil corals. *Geology* **45**, 1039-1042.

Gribble G. W. (1999) The diversity of naturally occurring organobromine compounds. *Chemical Society Reviews* **28**, 335-346.

Griffin J. J., Windom H. and Goldberg E. D. (1968) The distribution of clay minerals in the World Ocean. *Deep Sea Research and Oceanographic Abstracts* **15**, 433-459.

Harris R. N., Sakaguchi A., Petronotis K. and Scientists E. (2013) Costa Rica Seismogenesis Project, Program A Stage 2 (CRISP-A2), Proc. IODP, College Station, TX.

Harvey G. R. (1980) A study of the chemistry of iodine and bromine in marine sediments. *Mar. Chem.* **8**, 327-332.

Hayes J. M., Strauss H. and Kaufman A. J. (1999) The abundance of 13C in marine organic matter and isotopic fractionation in the global biogeochemical cycle of carbon during the past 800 Ma. *Chem. Geol.* **161**, 103-125.

Higgins J. A. and Schrag D. P. (2010) Constraining magnesium cycling in marine sediments using magnesium isotopes. *Geochim. Cosmochim. Acta* **74**, 5039-5053.

Higgins J. A. and Schrag D. P. (2012) Records of Neogene seawater chemistry and diagenesis in deep-sea carbonate sediments and pore fluids. *Earth Planet. Sci. Lett.* **357–358**, 386-396.

Higgins J. A. and Schrag D. P. (2015) The Mg isotopic composition of Cenozoic seawater – evidence for a link between Mg-clays, seawater Mg/Ca, and climate. *Earth Planet. Sci. Lett.* **416**, 73-81.

Hoefs J. (1980) *Stable isotope geochemistry*. Springer.

Hoehler T. M., Alperin M. J., Albert D. B. and Martens C. S. (1994) Field and laboratory studies of methane oxidation in an anoxic marine sediment: Evidence for a methanogen-sulfate reducer consortium. *Global Biogeochem. Cycles* **8**, 451-463.

Hoehler T. M., Alperin M. J., Albert D. B. and Martens C. S. (1998) Thermodynamic control on hydrogen concentrations in anoxic sediments. *Geochim. Cosmochim. Acta* **62**, 1745-1756.

Holland H. D. and Zimmermann H. (2000) The dolomite problem Revisited. *Int. Geol. Rev.* **42**, 481-490.

Holmden C., Papanastassiou D., Blanchon P. and Evans S. (2012) δ44/40Ca variability in shallow water carbonates and the impact of submarine groundwater discharge on Ca-cycling in marine environments. *Geochim. Cosmochim. Acta* **83**, 179-194.

Hong W.-L., Solomon E. A. and Torres M. E. (2014) A kinetic-model approach to quantify the effect of mass transport deposits on pore water profiles in the Krishna–Godavari Basin, Bay of Bengal. *Mar. Pet. Geol.* **58, Part A**, 223-232.

Hu Y., Teng F.-Z., Plank T. and Huang K.-J. (2017) Magnesium isotopic composition of subducting marine sediments. *Chem. Geol.* **466**, 15-31.

Huang J., Ke S., Gao Y., Xiao Y. and Li S. (2015) Magnesium isotopic compositions of altered oceanic basalts and gabbros from IODP site 1256 at the East Pacific Rise. *Lithos* **231**, 53-61.

Huang K.-J., Teng F.-Z., Plank T., Staudigel H., Hu Y. and Bao Z.-Y. (2018) Magnesium isotope composition of the altered oceanic crust and the global Mg cycle. *Geochim. Cosmochim. Acta* **238**, 357-373.

Huber C., Druhan J. L. and Fantle M. S. (2017) Perspectives on geochemical proxies: The impact of model and parameter selection on the quantification of carbonate recrystallization rates. *Geochim. Cosmochim. Acta* **217**, 171-192.

Immenhauser A., Buhl D., Richter D., Niedermayr A., Riechelmann D., Dietzel M. and Schulte U. (2010) Magnesium-isotope fractionation during low-Mg calcite precipitation in a limestone cave – field study and experiments. *Geochim. Cosmochim. Acta* **74**, 4346-4364.

Inagaki F., Nunoura T., Nakagawa S., Teske A., Lever M., Lauer A., Suzuki M., Takai K., Delwiche M., Colwell F. S., Nealson K. H., Horikoshi K., D'Hondt S. and Jørgensen B. B. (2006) Biogeographical distribution and diversity of microbes in methane hydrate-bearing deep marine sediments on the Pacific Ocean Margin. *Proc. Nat. Acad. Sci.* **103**, 2815-2820.

Jaffrés J. B. D., Shields G. A. and Wallmann K. (2007) The oxygen isotope evolution of seawater: A critical review of a long-standing controversy and an improved geological water cycle model for the past 3.4 billion years. *Earth-Science Reviews* **83**, 83-122.

Jansen E., Raymo M. E. and Blum P. (1996) Proc. ODP, Init. Repts., 162. Ocean Drilling Program, College Station, TX.

Jørgensen B. B. and Boetius A. (2007) Feast and famine — microbial life in the deep-sea bed. *Nature Reviews Microbiology* **5**, 770.

Justicia-Leon S. D., Ritalahti K. M., Mack E. E. and Löffler F. E. (2012) Dichloromethane Fermentation by a Dehalobacter sp. in an Enrichment Culture Derived from Pristine River Sediment. *Appl. Environ. Microbiol.* **78**, 1288-1291.

Kallmeyer J., Pockalny R., Adhikari R. R., Smith D. C. and D'Hondt S. (2012) Global distribution of microbial abundance and biomass in subseafloor sediment. *Proc. Nat. Acad. Sci.* **109**, 16213-16216.

Kaster A.-K., Mayer-Blackwell K., Pasarelli B. and Spormann A. M. (2014) Single cell genomic study of Dehalococcoidetes species from deep-sea sediments of the Peruvian Margin. *The ISME Journal* **8**, 1831-1842.

Kastner M. (1981) Authigenic silicates in deep-sea sediments: formation and diagenesis. In: *The Oceanic Lithosphere* (Eds. C. Emiliani). Interscience Publ., New York. pp. 915-980.

Kastner M., Solomon E. A., Harris R. N. and Torres M. E. (2014) Fluid origins, thermal regimes, and fluid and solute fluxes in the forearc of subduction zones. In: *Developments in Marine Geology* (Eds. R. Stein, D. K. Blackman, F. Inagaki, H.-C. Larsen). Elsevier. pp. 671-733.

Kinoshita M., Tobin H., Ashi J., Kimura G., Lallemant S., Screaton E. J., Curewitz D., Masago H. and Moe K. T. (2009a) Proc. IODP, 314/315/316. Integrated Ocean Drilling Program Management International, Inc., Washington, DC.

Kinoshita M., Tobin H., Ashi J., Kimura G., Lallemant S., Screaton E. J., Curewitz D., Masago H., Moe K. T. and Scientists E. (2009b) NanTroSEIZE Stage 1: investigations of seismogenesis, Nankai Trough, Japan, Proc. IODP. Integrated Ocean Drilling Program Management International, Inc., Washington, DC.

Knoll A. H., Hayes J. M., Kaufman A. J., Swett K. and Lambert I. B. (1986) Secular variation in carbon isotope ratios from Upper Proterozoic successions of Svalbard and East Greenland. *Nature* **321**, 832.

Krüger M., Wolters H., Gehre M., Joye S. B. and Richnow H.-H. (2008) Tracing the slow growth of anaerobic methane-oxidizing communities by 15N-labelling techniques. *FEMS Microbiol. Ecol.* **63**, 401-411.

Lange J. (1970) Geochemische Untersuchungen an Sedimenten des Persischen Golfes. *Contrib. Mineral. Petrol.* **28**, 288-305.

Lasaga A. C., Berner R. A. and Garrels R. M. (1985) An improved geochemical model of atmospheric CO2 fluctuations over the past 100 million years. *The Carbon Cycle and Atmospheric CO: Natural Variations Archean to Present*, 397-411.

Laske G. (1997) A global digital map of sediment thickness. *Eos Trans. AGU* **78**, F483.

Laudelout H., van Bladel R., Bolt G. H. and Page A. L. (1968) Thermodynamics of heterovalent cation exchange reactions in a montmorillonite clay. *Transactions of the Faraday Society* **64**, 1477-1488.

Lea D. (2003) Elemental and isotopic proxies of past ocean temperatures. *Treatise on Geochemistry* **6**, 365-390.

Lee M., Low A., Zemb O., Koenig J., Michaelsen A. and Manefield M. (2012) Complete chloroform dechlorination by organochlorine respiration and fermentation. *Environmental Microbiology* **14**, 883-894.

Lee T. and Wood W. T. (2018) Machine learning to predict global seafloor total organic carbon (submitted).

Leri A. C., Hakala J. A., Marcus M. A., Lanzirotti A., Reddy C. M. and Myneni S. C. B. (2010) Natural organobromine in marine sediments: New evidence of biogeochemical Br cycling. *Global Biogeochem. Cycles* **24**, GB4017.

Leri A. C., Mayer L. M., Thornton K. R., Northrup P. A., Dunigan M. R., Ness K. J. and Gellis A. B. (2015) A marine sink for chlorine in natural organic matter. *Nature Geosci* **8**, 620-624.

Lever M. A. (2013) Functional gene surveys from ocean drilling expeditions – a review and perspective. *FEMS Microbiol. Ecol.* **84**, 1-23.

Li Y.-H. and Gregory S. (1974) Diffusion of ions in sea water and in deep-sea sediments. *Geochim. Cosmochim. Acta* **38**, 703-714.

Ling M.-X., Sedaghatpour F., Teng F.-Z., Hays P. D., Strauss J. and Sun W. (2011) Homogeneous magnesium isotopic composition of seawater: an excellent geostandard for Mg isotope analysis. *Rapid Communications in Mass Spectrometry* **25**, 2828-2836.

Liu P.-P., Teng F.-Z., Dick H. J. B., Zhou M.-F. and Chung S.-L. (2017) Magnesium isotopic composition of the oceanic mantle and oceanic Mg cycling. *Geochim. Cosmochim. Acta* **206**, 151-165.

Locarnini R. A., Mishonov A. V., Antonov J. I., Boyer T. P., Garcia H. E., Baranova O. K., Zweng M. M., Paver C. R., Reagan J. R., Johnson D. R., Hamilton M. and Seidov D. (2013) World Ocean Atlas, Volume 2, Temperature, World Ocean Atlas.

Löffler F. E., Tiedje J. M. and Sanford R. A. (1999) Fraction of Electrons Consumed in Electron Acceptor Reduction and Hydrogen Thresholds as Indicators of Halorespiratory Physiology. *Appl. Environ. Microbiol.* **65**, 4049-4056.

Loyd S. J. and Berelson W. M. (2016) The modern record of “concretionary” carbonate: Reassessing a discrepancy between modern sediments and the geologic record. *Chem. Geol.* **420**, 77-87.

Luijten M. L. G. C., Roelofsen W., Langenhoff A. A. M., Schraa G. and Stams A. J. M. (2004) Hydrogen threshold concentrations in pure cultures of halorespiring bacteria and at a site polluted with chlorinated ethenes. *Environmental Microbiology* **6**, 646-650.

Lyle M., Koizumi I. and Richter C. (1997) Proc. ODP, Init. Repts., 167. Ocean Drilling Program, College Station, TX.

Mackenzie F. T. and Garrels R. M. (1966) Chemical mass balance between rivers and oceans. *Am. J. Sci.* **264**, 507-525.

Mackin J. E. and Aller R. C. (1984) Ammonium adsorption in marine sediments. *Limnol. Oceanogr.* **29**, 250-257.

Mahn C. L. and Gieskes J. M. (2001) Halide systematics in comparison with nutrient distributions in sites 1033B and 1034B, Saanich Inlet: ODP Leg 169S. *Mar. Geol.* **174**, 323-339.

Manheim F. T. and Sayles F. L. (1974) Composition and origin of interstitial waters of marine sediments, based on deep sea drill cores. In: *The Sea, Vol 5: Marine Chemistry* (Eds. E. D. Goldberg). Wiley, New York. pp. 527-568.

Martin J. B., Gieskes J. M., Torres M. and Kastner M. (1993) Bromine and iodine in Peru margin sediments and pore fluids: Implications for fluid origins. *Geochim. Cosmochim. Acta* **57**, 4377-4389.

Martin K. M., Wood W. T. and Becker J. J. (2015) A global prediction of seafloor sediment porosity using machine learning. *Geophys. Res. Lett.* **42**, 10,640-610,646.

Martino A. J., Biddle J. F. and House C. H. (2013) Microbial communities of the Costa Rica Margin: contamination controls and community analysis, AGU Fall Meeting Abstracts.

Matter A., Douglas R. G. and Perch-Nielsen K. (1975) Fossil preservation, geochemistry, and diagenesis of pelagic carbonates from Shatsky Rise, Northwest Pacific. *DSDP* **32**.

Mavromatis V., Meister P. and Oelkers E. H. (2014) Using stable Mg isotopes to distinguish dolomite formation mechanisms: A case study from the Peru Margin. *Chem. Geol.* **385**, 84-91.

Mayer L. M., Macko S. A., Mook W. H. and Murray S. (1981) The distribution of bromine in coastal sediments and its use as a source indicator for organic matter. *Org. Geochem.* **3**, 37-42.

Mayer L. M., Schick L. L., Allison M. A., Ruttenberg K. C. and Bentley S. J. (2007) Marine vs. terrigenous organic matter in Louisiana coastal sediments: The uses of bromine:organic carbon ratios. *Mar. Chem.* **107**, 244-254.

Mazumdar A., Dewangan P., Joäo H. M., Peketi A., Khosla V. R., Kocherla M., Badesab F. K., Joshi R. K., Roxanne P., Ramamurty P. B., Karisiddaiah S. M., Patil D. J., Dayal A. M., Ramprasad T., Hawkesworth C. J. and Avanzinelli R. (2009) Evidence of paleo-cold seep activity from the Bay of Bengal, offshore India. *G-cubed* **10**, Q06005.

Mazumdar A., João H. M., Peketi A., Dewangan P., Kocherla M., Joshi R. K. and Ramprasad T. (2012) Geochemical and geological constraints on the composition of marine sediment pore fluid: Possible link to gas hydrate deposits. *Mar. Pet. Geol.* **38**, 35-52.

Mazumdar A., Paropkari A. L., Borole D. V., Rao B. R., Khadge N. H., Karisiddaiah S. M., Kocherla M. and Joao H. M. (2007) Pore-water sulfate concentration profiles of sediment cores from Krishna-Godavari and Goa basins, India. *Geochem. J.* **41**, 259.

Michalopoulos P. and Aller R. C. (1995) Rapid clay mineral formation in Amazon Delta sediments: reverse weathering and oceanic elemental cycles. *Science* **270**, 614-617.

Miller R. S., Lawrence J. R. and Gieskes J. M. (1979) Interstitial water studies, Sites 386 and 387, Leg 43. *Proceedings of the Deep Sea Drilling Project* **43**.

Millero F. J., Feistel R., Wright D. G. and McDougall T. J. (2008) The composition of standard seawater and the definition of the reference-composition Salinity Scale. *Deep Sea Res. Part I* **55**, 50-72.

Milliman J. D. (1974) Marine carbonates. Recent sedimentary carbonates part 1. *Limnol. Oceanogr.* **19**, 876-876.

Milliman J. D. (1993) Production and accumulation of calcium carbonate in the ocean: budget of a nonsteady state. *Global Biogeochem. Cycles* **7**, 927-957.

Misra S. and Froelich P. N. (2012) Lithium isotope history of cenozoic seawater: Changes in silicate weathering and reverse weathering. *Science* **335**, 818-823.

Mitnick E. H., Lammers L. N., Zhang S., Zaretskiy Y. and DePaolo D. J. (2018) Authigenic carbonate formation rates in marine sediments and implications for the marine δ13C record. *Earth Planet. Sci. Lett.* **495**, 135-145.

Mohn W. W. and Tiedje J. M. (1992) Microbial reductive dehalogenation. *Microbiol. Rev.* **56**, 482-507.

Moore J. C. and Saffer D. (2001) Updip limit of the seismogenic zone beneath the accretionary prism of southwest Japan: An effect of diagenetic to low-grade metamorphic processes and increasing effective stress. *Geology* **29**, 183-186.

Moore J. C. and Vrolijk P. (1992) Fluids in accretionary prisms. *Rev. Geophys.* **30**, 113-135.

Morse J. W. and Mackenzie F. T. (1990) *Geochemistry of sedimentary carbonates*. Elsevier.

Mottl M. J. and Wheat C. G. (1994) Hydrothermal circulation through mid-ocean ridge flanks: fluxes of heat and magnesium. *Geochim. Cosmochim. Acta* **58**, 2225-2237.

Müller R. D., Sdrolias M., Gaina C. and Roest W. R. (2008) Age, spreading rates, and spreading asymmetry of the world's ocean crust. *Geochem. Geophys. Geosyst.* **9**.

Mun A. and Bazilevich Z. (1962) Distribution of bromine in lacustrine bottom muds. *Geochemistry* **2**, 199-205.

Naehr T. H., Eichhubl P., Orphan V. J., Hovland M., Paull C. K., Ussler W., Lorenson T. D. and Greene H. G. (2007) Authigenic carbonate formation at hydrocarbon seeps in continental margin sediments: A comparative study. *Deep Sea Res. Part II* **54**, 1268-1291.

Nealson K. H. (1997) Sediment bacteria: who's there, what are they doing, and what's new? *Annual Review of Earth and Planetary Sciences* **25**, 403-434.

Okumura M., Kitano Y. and Idogaki M. (1986) Behavior of bromide ions during the formation of calcium carbonate. *Mar. Chem.* **19**, 109-120.

Orcutt B. N., Sylvan J. B., Knab N. J. and Edwards K. J. (2011) Microbial ecology of the dark ocean above, at, and below the seafloor. *Microbiol. Mol. Biol. Rev.* **75**, 361-422.

Pandiyan T., Martínez Rivas O., Orozco Martínez J., Burillo Amezcua G. and Martínez-Carrillo M. A. (2002) Comparison of methods for the photochemical degradation of chlorophenols. *J. Photochem. Photobiol. A: Chemistry* **146**, 149-155.

Parkes R. J., Webster G., Cragg B. A., Weightman A. J., Newberry C. J., Ferdelman T. G., Kallmeyer J., Jørgensen B. B., Aiello I. W. and Fry J. C. (2005) Deep sub-seafloor prokaryotes stimulated at interfaces over geological time. *Nature* **436**, 390-394.

Peacock S. M. (1990) Fluid Processes in Subduction Zones. *Science* **248**, 329-337.

Pedersen T. F. and Price N. B. (1980) The geochemistry of iodine and bromine in sediments of the Panama Basin. *J. Mar. Res.* **38**, 397-411.

Pedregosa F., Varoquaux G., Gramfort A., Michel V., Thirion B., Grisel O., Blondel M., Prettenhofer P., Weiss R. and Dubourg V. (2011) Scikit-learn: machine learning in Python. *Journal of machine learning research* **12**, 2825-2830.

Plank T. and Langmuir C. H. (1998) The chemical composition of subducting sediment and its consequences for the crust and mantle. *Chem. Geol.* **145**, 325-394.

Pogge von Strandmann P. A. E. (2008) Precise magnesium isotope measurements in core top planktic and benthic foraminifera. *Geochem. Geophys. Geosyst.* **9**.

Pogge von Strandmann P. A. E., Forshaw J. and Schmidt D. N. (2014) Modern and Cenozoic records of seawater magnesium from foraminiferal Mg isotopes. *Biogeosciences* **11**, 5155-5168.

Price N. B. and Calvert S. E. (1977) The contrasting geochemical behaviours of iodine and bromine in recent sediments from the Namibian shelf. *Geochim. Cosmochim. Acta* **41**, 1769-1775.

Price N. B., Calvert S. E. and Jones P. G. W. (1970) The distribution of iodine and bromine in the sediments of the southwestern Barents Sea. *J. Mar. Res.* **28**, 22-34.

Ramprasad T., Dewangan P., Ramana M. V., Mazumdar A., Karisiddaiah S. M., Ramya E. R. and Sriram G. (2011) Evidence of slumping/sliding in Krishna–Godavari offshore basin due to gas/fluid movements. *Mar. Pet. Geol.* **28**, 1806-1816.

Saffer D. M. and Bekins B. A. (1998) Episodic fluid flow in the Nankai accretionary complex: Timescale, geochemistry, flow rates, and fluid budget. *Journal of Geophysical Research: Solid Earth* **103**, 30351-30370.

Saffer D. M. and Tobin H. J. (2011) Hydrogeology and mechanics of subduction zone forearcs: fluid flow and pore pressure. *Annual Review of Earth and Planetary Sciences* **39**, 157-186.

Sayles F. L. (1979) The composition and diagenesis of interstitial solutions—I. Fluxes across the seawater-sediment interface in the Atlantic Ocean. *Geochim. Cosmochim. Acta* **43**, 527-545.

Sayles F. L. and Mangelsdorf Jr P. C. (1977) The equilibration of clay minerals with sea water: exchange reactions. *Geochim. Cosmochim. Acta* **41**, 951-960.

Schrag D. P., Higgins J. A., Macdonald F. A. and Johnston D. T. (2013) Authigenic Carbonate and the History of the Global Carbon Cycle. *Science* **339**, 540-543.

Schrum H. N., Spivack A. J., Kastner M. and D'Hondt S. (2009) Sulfate-reducing ammonium oxidation: A thermodynamically feasible metabolic pathway in subseafloor sediment. *Geology* **37**, 939-942.

Seyfried W. E. and Bischoff J. L. (1979) Low temperature basalt alteration by sea water: an experimental study at 70°C and 150°C. *Geochim. Cosmochim. Acta* **43**, 1937-1947.

Snow J. E. and Dick H. J. B. (1995) Pervasive magnesium loss by marine weathering of peridotite. *Geochim. Cosmochim. Acta* **59**, 4219-4235.

Snyder G. T., Hiruta A., Matsumoto R., Dickens G. R., Tomaru H., Takeuchi R., Komatsubara J., Ishida Y. and Yu H. (2007) Pore water profiles and authigenic mineralization in shallow marine sediments above the methane-charged system on Umitaka Spur, Japan Sea. *Deep Sea Res. Part II* **54**, 1216-1239.

Solomon E., Torres M., Harris R., Formolo M. and Nuzzo M. (2011) Geochemical constraints on fluid-rock reactions, fluid sources, and flow pathways along the CRISP transect; IODP Expedition 334, AGU Fall Meeting Abstracts.

Solomon E. A., Kastner M., Wheat C. G., Jannasch H., Robertson G., Davis E. E. and Morris J. D. (2009) Long-term hydrogeochemical records in the oceanic basement and forearc prism at the Costa Rica subduction zone. *Earth Planet. Sci. Lett.* **282**, 240-251.

Solomon E. A., Spivack A. J., Kastner M., Torres M. E. and Robertson G. (2014) Gas hydrate distribution and carbon sequestration through coupled microbial methanogenesis and silicate weathering in the Krishna–Godavari basin, offshore India. *Mar. Pet. Geol.* **58**, 233-253.

Stumm W. and Morgan J. J. (2012) *Aquatic chemistry: chemical equilibria and rates in natural waters*. John Wiley & Sons.

Suess E. and von Huene R. (1988) Initial Reports, Volume 112, Proceedings of the Ocean Drilling Program. Ocean Drilling Program, College Station, TX.

Sun X., Higgins J. and Turchyn A. V. (2016) Diffusive cation fluxes in deep-sea sediments and insight into the global geochemical cycles of calcium, magnesium, sodium and potassium. *Mar. Geol.* **373**, 64-77.

Sun X. and Turchyn A. V. (2014) Significant contribution of authigenic carbonate to marine carbon burial. *Nature Geosci* **7**, 201-204.

Teichert B., Johnson J., Solomon E., Giosan L., Rose K., Kocherla M., Connolly E. and Torres M. (2014) Composition and origin of authigenic carbonates in the Krishna–Godavari and Mahanadi Basins, eastern continental margin of India. *Mar. Pet. Geol.* **58**, 438-460.

Teng F.-Z., Li W.-Y., Ke S., Yang W., Liu S.-A., Sedaghatpour F., Wang S.-J., Huang K.-J., Hu Y., Ling M.-X., Xiao Y., Liu X.-M., Li X.-W., Gu H.-O., Sio C. K., Wallace D. A., Su B.-X., Zhao L., Chamberlin J., Harrington M. and Brewer A. (2015) Magnesium isotopic compositions of international geological reference materials. *Geostand. Geoanal. Res.* **39**, 329-339.

Teng F.-Z. and Yang W. (2014) Comparison of factors affecting the accuracy of high-precision magnesium isotope analysis by multi-collector inductively coupled plasma mass spectrometry. *Rapid Communications in Mass Spectrometry* **28**, 19-24.

Tipper E. T., Galy A., Gaillardet J., Bickle M. J., Elderfield H. and Carder E. A. (2006) The magnesium isotope budget of the modern ocean: constraints from riverine magnesium isotope ratios. *Earth Planet. Sci. Lett.* **250**, 241-253.

Tokarz J. A., Ahn M.-Y., Leng J., Filley T. R. and Nies L. (2008) Reductive Debromination of Polybrominated Diphenyl Ethers in Anaerobic Sediment and a Biomimetic System. *Environmental Science & Technology* **42**, 1157-1164.

Torres M. and Kastner M. (2008) Data report: Clues about carbon cycling in methane-bearing sediments using stable isotopes of the dissolved inorganic carbon, IODP Expedition 311, Proc. IODP| Volume, p. 2.

Torres M. E., Solomon E. A., Kastner M., Harris R. N., Formolo M., Choi J., Berg R. D. and Nuzzo M. (2013) Geochemical evidence for fluid flow in the upper and subducting plates of the Costa Rica margin: Results from CRISP drilling during Exp. 334 and 344 (invited) Abstract T34C-02, AGU Fall Meeting, San Francisco, CA.

Townsend G. T. and Suflita J. M. (1997) Influence of sulfur oxyanions on reductive dehalogenation activities in Desulfomonile tiedjei. *Appl. Environ. Microbiol.* **63**, 3594-3599.

Upstill-Goddard R. C. and Elderfield H. (1988) The role of diagenesis in the estuarine budgets of iodine and bromine. *Cont. Shelf Res.* **8**, 405-430.

Valentine D. L. (2011) Emerging Topics in Marine Methane Biogeochemistry. *Annu. Rev. Mar. Sci.* **3**, 147-171.

Vannucchi P., Ujiie K. and Gamage K. (2010) Costa Rica Seismogenesis Project (CRISP): sampling and quantifying input to the seismogenic zone and fluid output. *IODP Scientific Prospectus* **334**.

Vannucchi P., Ujiie K. and Stroncik N. (2012a) Proc. IODP, 334. Integrated Ocean Drilling Program Management International, Inc., Tokyo.

Vannucchi P., Ujiie K., Stroncik N. and Scientists E. (2012b) Costa Rica Seismogenesis Project, Program A Stage 1 (CRISP-A1). *Proc. IODP* **334**.

von Breymann M. T., Collier R. and Suess E. (1990a) Magnesium adsorption and ion exchange in marine sediments: A multi-component model. *Geochim. Cosmochim. Acta* **54**, 3295-3313.

von Breymann M. T., Emeis K.-C. and Camerlenghi A. (1990b) Geochemistry of sediments from the Peru upwelling area: results from Sites 680, 682, 685, and 688. *Proceedings of the Ocean Drilling Program* **112**, 491–503.

Von Breymann M. T. and Suess E. (1988) Magnesium in the marine sedimentary environment: Mg□NH4 ion exchange. *Chem. Geol.* **70**, 359-371.

Wallmann K. (2001) The geological water cycle and the evolution of marine δ18O values. *Geochim. Cosmochim. Acta* **65**, 2469-2485.

Wallmann K., Aloisi G., Haeckel M., Tishchenko P., Pavlova G., Greinert J., Kutterolf S. and Eisenhauer A. (2008) Silicate weathering in anoxic marine sediments. *Geochim. Cosmochim. Acta* **72**, 2895-2918.

Walter L. M., Bischof S. A., Patterson W. P. and Lyons T. W. (1993) Dissolution and recrystallization in modern shelf carbonates: evidence from pore water and solid phase chemistry. *Philosophical Transactions of the Royal Society of London. Series A: Physical and Engineering Sciences* **344**, 27.

Wang G., Spivack A. J., Rutherford S., Manor U. and D'Hondt S. (2008) Quantification of co-occurring reaction rates in deep subseafloor sediments. *Geochim. Cosmochim. Acta* **72**, 3479-3488.

Warren J. K. (2010) Evaporites through time: Tectonic, climatic and eustatic controls in marine and nonmarine deposits. *Earth-Science Reviews* **98**, 217-268.

Wasmund K., Schreiber L., Lloyd K. G., Petersen D. G., Schramm A., Stepanauskas R., Jørgensen B. B. and Adrian L. (2013) Genome sequencing of a single cell of the widely distributed marine subsurface Dehalococcoidia, phylum Chloroflexi. *The ISME Journal* **8**, 383-397.

Weaver C. E. and Pollard L. D. (2011) *The chemistry of clay minerals*. Elsevier.

Wedepohl K. H. (1995) The composition of the continental crust. *Geochim. Cosmochim. Acta* **59**, 1217-1232.

Wefer G., Berger W. H. and Richter C. (1998) Proc. ODP, Init. Repts., 175. Ocean Drilling Program, College Station, TX.

Whittaker J. M., Goncharov A., Williams S. E., Müller R. D. and Leitchenkov G. (2013) Global sediment thickness data set updated for the Australian-Antarctic Southern Ocean. *Geochem. Geophys. Geosyst.* **14**, 3297-3305.

Wilkinson B. H. and Algeo T. J. (1989) Sedimentary carbonate record of calcium-magnesium cycling. *Am. J. Sci.* **289**, 1158-1194.

Wimpenny J., Colla C. A., Yin Q.-Z., Rustad J. R. and Casey W. H. (2014) Investigating the behaviour of Mg isotopes during the formation of clay minerals. *Geochim. Cosmochim. Acta* **128**, 178-194.

Wombacher F., Eisenhauer A., Böhm F., Gussone N., Regenberg M., Dullo W. C. and Rüggeberg A. (2011) Magnesium stable isotope fractionation in marine biogenic calcite and aragonite. *Geochim. Cosmochim. Acta* **75**, 5797-5818.

Wood W., Becker J., Martin K. and Jung W. (2014) Global marine gas hydrate occurrence using random decision forest prediction, AGU Fall Meeting Abstracts, pp. OS24A-04.

Yang C., Kublik A., Weidauer C., Seiwert B. and Adrian L. (2015) Reductive Dehalogenation of Oligocyclic Phenolic Bromoaromatics by Dehalococcoides mccartyi Strain CBDB1. *Environmental Science & Technology* **49**, 8497-8505.

You C.-F., Gieskes J. M., Chen R. F., Spivack A. and Gamo T. (1993) Iodide, bromide, manganese, boron, and dissolved organic carbon in interstitial waters of the organic carbon–rich marine sediments: observations in the Nankai accretionary prism. *Proceedings of the Ocean Drilling Program, Scientific Results* **131**, 165–174.

Young E. D. and Galy A. (2004) The isotope geochemistry and cosmochemistry of magnesium. *Rev. Mineral. Geochem.* **55**, 197-230.

Zhu H., Wang Y., Wang X., Luan T. and Tam N. F. Y. (2014) Intrinsic Debromination Potential of Polybrominated Diphenyl Ethers in Different Sediment Slurries. *Environmental Science & Technology* **48**, 4724-4731.

Ziegler M., Jilbert T., de Lange G. J., Lourens L. J. and Reichart G.-J. (2008) Bromine counts from XRF scanning as an estimate of the marine organic carbon content of sediment cores. *G-cubed* **9**, Q05009.

Zweng M. M., Reagan J. R., Antonov J. I., Locarnini R. A., Mishonov A. V., Boyer T. P., Garcia H. E., Baranova O. K., Johnson D. R. and Seidov D. (2013) World Ocean Atlas 2013. Volume 2, Salinity.

APPENDIX A

Table A1. Solid-phase bromine concentrations from K-G basin Site 14.

Site	Hole	Core	Type	Section	Top (cm)	Bottom (cm)	Depth (mbsf)	Bromine (ppm)	1σ standard deviation	Notes
14	A	1	H	3	128	138	4.3	16.66	0.66	
14	A	2	H	2	140	150	7.4	20.69	0.77	
14	A	2	H	4	140	150	10.4	39.82	1.25	
14	A	2	H	6	90	100	12.9	33.20	1.07	
14	A	3	H	1	140	150	15.4	13.52	0.61	
14	A	3	H	3	140	150	18.4	37.60	1.22	
14	A	3	H	5	140	150	21.4	22.84	0.78	
14	A	3	H	6	90	100	22.4	9.41	0.54	
14	A	3	H	7	90	100	23.4	5.56	0.62	
14	A	4	H	5	140	150	30.9	2.67	0.33	
14	A	5	H	3	140	150	37.4	5.75	0.45	
14	A	5	H	5	140	150	40.4	4.53	0.48	
14	A	6	H	3	130	150	46.8	4.85	0.50	
14	A	6	H	5	118	138	49.7	4.64	0.33	
14	A	6	H	6	106	132	50.9	8.30	0.40	
14	A	7	H	5	130	150	59.2	4.73	0.31	duplicate
14	A	7	H	5	130	150	59.2	4.61	0.36	duplicate
14	A	8	H	3	127	147	65.0	3.55	0.32	
14	A	8	H	5	130	150	67.6	19.74	0.67	
14	A	11	X	2	113	136	75.6	11.95	0.46	
14	A	11	X	3	130	150	77.2	6.21	0.39	
14	A	12	X	5	130	150	89.1	15.31	0.53	
14	A	13	X	5	130	150	99.5	4.20	0.29	
14	A	16	X	2	60	90	104.1	3.61	0.37	w/ hydrate
14	A	16	X	2	60	90	104.1	4.69	0.35	background
14	A	18	X	1	75	100	121.9	2.85	0.40	
14	A	18	X	2	86	116	123.1	2.61	0.36	
14	A	20	X	4	82	112	144.7	2.36	0.27	
14	A	22	X	2	120	150	162.3	2.03	0.31	

Table A2. Solid-phase bromine concentrations from K-G basin Sites 20.

Site	Hole	Core	Type	Section	Top (cm)	Bottom (cm)	Depth (mbsf)	Bromine (ppm)	1σ standard deviation	Notes
20	A	1	H	1	140	150	1.4	20.52	0.75	
20	A	1	H	3	140	150	4.4	14.83	0.65	
20	A	2	H	1	135	150	7.0	24.23	0.84	
20	A	2	H	3	135	150	10.0	10.06	0.56	
20	A	2	H	5	135	150	13.0	8.04	0.49	
20	A	3	H	1	135	150	16.5	11.78	0.60	
20	A	3	H	2	135	150	18.0	10.41	0.54	
20	A	3	H	3	135	150	19.5	9.11	0.46	
20	A	3	H	4	135	150	21.0	11.06	0.60	
20	A	3	H	5	115	130	22.3	7.09	0.38	
20	A	4	X	1	130	150	24.2	13.76	0.54	
20	A	5	X	1	130	150	33.8	6.77	0.38	
20	A	6	X	1	135	150	43.4	4.95	0.31	duplicate
20	A	6	X	1	135	150	43.4	3.82	0.30	duplicate
20	A	6	X	3	36	56	45.0	5.12	0.51	
20	A	9	X	1	130	150	72.2	2.46	0.30	
20	A	11	X	1	125	150	91.5	5.05	0.37	
20	A	13	X	1	97	122	98.8	6.96	0.48	
20	A	15	X	1	95	120	108.4	5.45	0.39	
20	A	16	X	6	21	51	119.6	9.75	0.46	w/ hydrate
20	A	16	X	6	21	51	119.6	9.89	0.56	background
20	A	18	X	1	75	100	132.4	5.79	0.54	

Table A3. Solid-phase bromine concentrations from IODP Expedition 344 Site U1412.

Site	Hole	Core	Type	Section	Top (cm)	Bottom (cm)	Depth (mbsf)	Bromine (ppm)	1σ standard deviation	Notes
U1412	A	1	H	1	138	150	1.4	52.62	1.57	
U1412	A	1	H	2	138	150	2.9	56.31	1.67	
U1412	A	1	H	4	98	110	5.5	41.15	1.25	
U1412	A	2	H	2	138	150	8.8	21.75	0.72	
U1412	A	2	H	6	72	84	14.2	20.75	0.73	
U1412	A	2	H	7	106	118	15.4	23.95	0.78	
U1412	A	3	H	1	138	150	16.8	21.96	0.75	
U1412	A	3	H	3	138	150	19.8	18.52	0.66	
U1412	A	3	H	5	138	150	22.8	12.52	0.52	
U1412	A	4	H	2	138	150	27.8	15.04	0.58	
U1412	A	4	H	4	138	150	30.9	22.64	0.78	
U1412	A	5	H	3	118	135	36.2	26.11	0.87	
U1412	A	5	H	7	118	135	36.2	25.38	0.86	duplicate
U1412	A	5	H	7	133	150	40.5	25.46	0.88	duplicate
U1412	A	6	H	2	132	149	44.9	33.14	1.06	
U1412	A	6	H	4	134	151	47.9	23.06	0.80	
U1412	A	7	H	2	128	145	51.9	23.49	0.81	
U1412	A	7	H	5	103	120	55.9	24.02	0.86	
U1412	A	8	H	1	129	151	58.9	28.22	0.97	
U1412	A	8	H	3	100	122	61.6	19.93	0.79	
U1412	A	9	H	2	128	150	65.8	28.55	0.97	
U1412	A	9	H	6	135	157	70.5	12.75	0.65	
U1412	A	10	H	1	128	150	73.6	29.72	1.02	
U1412	A	10	H	5	134	156	79.6	22.97	0.91	
U1412	A	11	H	2	130	152	83.9	25.81	0.91	
U1412	A	12	H	1	115	137	87.6	23.28	0.79	
U1412	A	12	H	3	94	116	90.1	18.67	0.67	
U1412	A	13	H	2	124	146	93.6	22.03	0.78	
U1412	A	14	H	2	80	102	98.2	15.79	0.59	replicate
U1412	A	14	H	2	80	102	98.2	15.56	0.58	replicate
U1412	A	15	H	2	93	115	106.8	19.90	0.68	
U1412	A	16	X	2	126	148	111.0	17.82	0.65	
U1412	A	20	X	4	131	151	148.0	27.31	0.90	
U1412	A	22	X	1	131	151	162.9	14.80	0.60	
U1412	A	22	X	3	68	88	165.0	15.15	0.61	
U1412	A	23	X	3	100	120	175.3	13.65	0.61	
U1412	A	24	X	2	56	81	182.4	14.68	0.61	

Table A4. Solid-phase bromine concentrations in quality control samples.

Standard	Bromine (ppm)	1σ standard deviation
NIST1570-1	49.90	1.87
NIST1570-2	50.38	1.88
NIST1570A-1	37.12	1.25
NIST1570A-1	32.68	1.08
NIST1570A-1	34.60	1.15
NIST1570A-1	33.17	1.06
NIST1570A-2	34.99	1.23
NIST1570A-2	34.93	1.16
NIST1570A-2	34.02	1.12
NIST1570A-2	34.15	1.14

Table A5. Pore water bromide concentrations at IODP Expedition 334 Site U1378.

Site	Hole	Core	Coring Type	Section	Interval (cm)	Depth (mbsf)	Bromide (mM)	Notes
U1378	B	1	H	1	138-168	1.44	0.816	
U1378	B	1	H	2	138-168	2.94	0.845	
U1378	B	1	H	3	138-168	4.44	0.859	
U1378	B	1	H	4	46-58	5.02	0.850	
U1378	B	2	H	1	138-168	6.74	0.866	duplicate
U1378	B	2	H	1	138-168	6.74	0.866	duplicate
U1378	B	2	H	2	138-150	8.24	0.873	triplicate
U1378	B	2	H	2	138-150	8.24	0.883	triplicate
U1378	B	2	H	2	138-150	8.24	0.878	triplicate
U1378	B	2	H	3	138-168	9.74	0.911	
U1378	B	2	H	4	138-168	11.24	0.883	
U1378	B	2	H	5	138-150	12.74	0.896	
U1378	B	2	H	6	138-150	14.24	0.894	
U1378	B	2	H	7	54-66	14.9	0.887	
U1378	B	3	H	1	138-150	16.24	0.883	
U1378	B	3	H	2	138-150	17.74	0.917	
U1378	B	3	H	3	138-148	19.24	0.910	
U1378	B	3	H	4	138-148	20.74	0.927	
U1378	B	3	H	5	138-148	22.24	0.939	
U1378	B	3	H	6	133-143	23.69	0.939	
U1378	B	3	H	7	58-68	24.44	0.935	
U1378	B	4	H	3	138-148	27.85	0.976	
U1378	B	4	H	6	138-148	32.35	0.983	
U1378	B	5	H	2	138-148	36.74	1.011	
U1378	B	5	H	6	138-148	42.74	1.024	
U1378	B	6	H	2	138-148	46.24	1.025	
U1378	B	6	H	5	138-148	50.74	1.052	
U1378	B	7	H	2	138-148	55.74	1.065	
U1378	B	7	H	5	138-148	60.045	1.070	
U1378	B	8	H	2	138-148	63.88	1.084	triplicate
U1378	B	8	H	2	138-148	63.88	1.086	triplicate
U1378	B	8	H	2	138-148	63.88	1.074	triplicate
U1378	B	8	H	5	138-153	68.38	1.121	
U1378	B	9	H	2	138-153	74.655	1.123	
U1378	B	9	H	5	130-145	79.16	1.123	
U1378	B	10	H	2	130-145	84.16	1.159	
U1378	B	10	H	4	138-153	87.16	1.155	
U1378	B	11	H	3	138-153	94.04	1.143	triplicate
U1378	B	11	H	3	138-153	94.04	1.166	triplicate
U1378	B	11	H	3	138-153	94.04	1.164	triplicate
U1378	B	13	H	4	138-153	107.94	1.257	
U1378	B	14	H	3	138-153	114.15	1.227	duplicate
U1378	B	14	H	3	138-153	114.15	1.277	duplicate
U1378	B	15	H	2	118-133	118.54	1.327	
U1378	B	16	H	3	133-148	124.84	1.341	
U1378	B	18	X	3	113-128	136.415	1.319	
U1378	B	19	X	5	71-86	148.675	1.341	
U1378	B	20	X	5	130-145	158.355	1.332	
U1378	B	21	X	7	68-83	169.765	1.355	
U1378	B	23	X	6	109-124	188.875	1.420	
U1378	B	24	X	4	122-137	195.05	1.448	
U1378	B	25	X	3	74-89	202.77	1.429	
U1378	B	26	X	4	98-113	214.765	1.385	duplicate
U1378	B	26	X	4	98-113	214.765	1.400	duplicate
U1378	B	27	X	2	100-115	220.135	1.412	
U1378	B	28	X	7	33-63	236.59	1.479	
U1378	B	29	X	3	45-80	236.94	1.442	
U1378	B	30	X	2	110-145	241.075	1.477	
U1378	B	31	X	4	118-148	252.64	1.498	
U1378	B	32	X	3	73-103	259.99	1.483	
U1378	B	33	X	5	58-93	272.07	1.463	
U1378	B	34	X	2	86-121	278.14	1.498	
U1378	B	35	X	5	98-133	292.24	1.435	

U1378	B	36	X	2	93-128	297.79	1.459	
U1378	B	37	X	2	91-126	307.37	1.520	
U1378	B	38	X	1	118-153	315.235	1.456	duplicate
U1378	B	38	X	1	118-153	315.235	1.496	duplicate
U1378	B	39	X	5	118-153	321.84	1.572	
U1378	B	40	X	4	80-115	329.16	1.488	
U1378	B	41	X	5	104-139	340.9	1.550	triplicate
U1378	B	41	X	5	104-139	340.9	1.545	triplicate
U1378	B	41	X	5	104-139	340.9	1.547	triplicate
U1378	B	42	X	3	64-94	347.2	1.480	
U1378	B	43	X	5	55-85	358.87	1.494	
U1378	B	45	X	3	55-85	369.815	1.469	
U1378	B	46	X	2	115-145	374.425	1.493	
U1378	B	47	X	2	95-125	379.525	1.462	
U1378	B	48	X	1	96-121	382.99	1.470	
U1378	B	49	X	3	106-136	394.52	1.486	
U1378	B	50	X	2	97-127	402.245	1.464	
U1378	B	51	X	5	85-115	416.12	1.441	
U1378	B	52	X	5	70-100	425.16	1.428	
U1378	B	53	X	3	53-83	430.86	1.419	
U1378	B	54	X	5	104-139	444.42	1.449	
U1378	B	55	X	2	81-116	448.99	1.485	duplicate
U1378	B	55	X	2	81-116	448.99	1.502	duplicate
U1378	B	56	X	2	64-99	458.3	1.386	
U1378	B	57	X	3	63-98	469.51	1.322	duplicate
U1378	B	57	X	3	63-98	469.51	1.400	duplicate
U1378	B	59	X	4	93-128	489.82	1.319	duplicate
U1378	B	59	X	4	93-128	489.82	1.327	duplicate
U1378	B	60	X	4	60-95	499.88	1.385	
U1378	B	61	X	4	102-137	510.3	1.349	
U1378	B	62	X	1	54-79	510.375	1.279	
U1378	B	63	X	4	84-119	518.93	1.287	

Table A6. Pore water bromide concentrations at IODP Expedition 334 Site U1379.

Site	Hole	Core	Coring Type	Section	Interval (cm)	Depth (mbsf)	Bromide (mM)	Notes
U1379	C	1	H	1	140-150	1.4	0.784	
U1379	C	1	H	2	140-150	2.9	0.792	
U1379	C	1	H	3	140-150	4.4	0.846	
U1379	C	1	H	4	140-150	5.9	0.841	
U1379	C	1	H	5	50-63	6.5	0.866	
U1379	C	2	H	1	140-150	8.1	0.838	
U1379	C	2	H	2	140-150	9.6	0.875	
U1379	C	2	H	3	140-150	11.1	0.853	
U1379	C	2	H	4	140-150	12.6	0.876	
U1379	C	2	H	6	36-46	14.56	0.859	
U1379	C	3	H	1	138-150	17.58	0.871	duplicate
U1379	C	3	H	1	138-150	17.58	0.879	duplicate
U1379	C	3	H	2	138-150	19.08	0.891	duplicate
U1379	C	3	H	2	138-150	19.08	0.889	duplicate
U1379	C	3	H	3	138-150	20.58	0.880	
U1379	C	3	H	4	138-150	22.08	0.873	
U1379	C	3	H	5	138-150	23.58	0.916	
U1379	C	3	H	6	39-50	24.09	0.887	
U1379	C	4	H	2	138-150	27.08	0.899	
U1379	C	4	H	4	92-104	29.62	0.881	
U1379	C	5	H	2	138-150	33.08	0.925	
U1379	C	5	H	4	149-161	36.19	0.885	
U1379	C	6	H	2	138-150	39.38	0.932	
U1379	C	6	H	4	138-150	42.38	0.894	
U1379	C	7	H	2	138-150	45.38	0.899	
U1379	C	7	H	4	136-148	48.36	0.948	
U1379	C	8	H	2	138-150	51.98	0.921	
U1379	C	8	H	4	130-142	54.9	0.937	
U1379	C	9	H	2	138-150	58.38	0.945	
U1379	C	9	H	4	128-150	61.28	1.015	
U1379	C	11	H	1	138-150	64.88	1.037	
U1379	C	11	H	3	78-90	67.28	1.053	
U1379	C	12	H	2	138-150	70.58	1.013	duplicate
U1379	C	12	H	2	138-150	70.58	1.036	duplicate
U1379	C	12	H	4	103-115	73.23	1.058	
U1379	C	13	H	2	138-150	76.58	1.115	
U1379	C	14	H	2	138-150	81.58	1.144	duplicate
U1379	C	14	H	2	138-150	81.58	1.159	duplicate
U1379	C	15	H	3	100-112	86.15	1.218	
U1379	C	16	H	2	138-150	89.38	1.195	
U1379	C	17	H	1	76-89	90.96	1.198	
U1379	C	20	X	1	137-150	112.07	1.289	
U1379	C	20	X	3	137-150	115.07	1.225	
U1379	C	21	X	3	133-145	124.83	1.407	
U1379	C	22	X	3	137-150	133.52	1.378	
U1379	C	22	X	6	138-150	138.03	1.394	duplicate
U1379	C	22	X	6	138-150	138.03	1.395	duplicate
U1379	C	23	X	1	138-150	141.48	1.410	
U1379	C	23	X	6	113-130	148.73	1.417	
U1379	C	24	X	3	133-150	154.23	1.424	
U1379	C	24	X	6	124-141	158.64	1.484	
U1379	C	25	X	3	133-150	164.03	1.465	
U1379	C	25	X	5	128-150	166.98	1.449	
U1379	C	26	X	3	133-150	173.83	1.421	
U1379	C	26	X	6	113-130	178.13	1.529	
U1379	C	27	X	3	133-150	183.63	1.494	
U1379	C	27	X	6	113-130	187.93	1.521	
U1379	C	28	X	3	133-150	192.32	1.555	
U1379	C	28	X	6	133-150	196.74	1.530	
U1379	C	30	X	2	133-150	211.53	1.583	
U1379	C	31	X	2	133-150	219.33	1.553	duplicate
U1379	C	31	X	2	133-150	219.33	1.551	duplicate
U1379	C	31	X	5	133-150	223.83	1.582	

U1379	C	32	X	2	133-150	229.13	1.520	
U1379	C	32	X	6	133-150	235.13	1.564	
U1379	C	33	X	5	122-144	243.32	1.539	
U1379	C	34	X	3	128-150	250.18	1.541	
U1379	C	35	X	5	78-100	262.48	1.550	
U1379	C	36	X	5	128-150	271.74	1.530	
U1379	C	37	X	5	128-150	282.58	1.488	
U1379	C	38	X	5	128-150	292.38	1.558	duplicate
U1379	C	38	X	5	128-150	292.38	1.552	duplicate
U1379	C	39	X	3	129-150	299.19	1.483	
U1379	C	40	X	4	100-122	310.2	1.509	
U1379	C	41	X	4	128-150	320.28	1.503	
U1379	C	42	X	3	123-145	328.43	1.567	
U1379	C	43	X	6	81-107	341.41	1.566	
U1379	C	44	X	6	78-107	350.88	1.563	
U1379	C	46	X	5	75-100	368.45	1.555	
U1379	C	47	X	5	133-150	378.03	1.582	
U1379	C	48	X	6	63-100	386.36	1.520	
U1379	C	49	X	6	75-100	395.85	1.543	
U1379	C	51	X	4	104-129	412.54	1.517	
U1379	C	52	X	2	118-150	420.08	1.508	duplicate
U1379	C	52	X	2	118-150	420.08	1.549	duplicate
U1379	C	54	X	4	75-107	439.62	1.475	duplicate
U1379	C	54	X	4	75-107	439.62	1.475	duplicate
U1379	C	55	X	3	87-119	448.07	1.528	
U1379	C	56	X	4	100-132	458.7	1.562	
U1379	C	57	X	3	118-150	467.58	1.550	
U1379	C	58	X	4	90-129	477.5	1.492	
U1379	C	59	X	4	106-138	486.66	1.544	
U1379	C	60	X	4	118-150	496.38	1.566	
U1379	C	61	X	5	118-150	507.58	1.612	
U1379	C	63	X	5	118-150	524.88	1.533	
U1379	C	64	X	5	125-150	534.35	1.575	
U1379	C	67	X	6	70-100	563.8	1.552	
U1379	C	68	X	4	88-120	570.38	1.506	
U1379	C	69	X	3	93-125	578.33	1.557	
U1379	C	70	X	4	92-124	589.72	1.483	
U1379	C	71	X	4	64-96	598.54	1.423	
U1379	C	73	X	5	116-150	619.56	1.561	duplicate
U1379	C	73	X	5	116-150	619.56	1.544	duplicate
U1379	C	74	X	4	74-107	626.34	1.473	
U1379	C	75	X	4	86-120	636.37	1.478	
U1379	C	76	X	3	118-150	645.21	1.454	
U1379	C	77	X	2	118-150	648.48	1.437	duplicate
U1379	C	77	X	2	118-150	648.48	1.484	duplicate
U1379	C	78	X	4	110-150	656.6	1.419	
U1379	C	80	X	4	93-125	674.74	1.344	
U1379	C	81	X	2	100-132	682	1.376	
U1379	C	82	X	3	70-102	692.6	1.302	
U1379	C	84	X	3	56-88	712.41	1.373	
U1379	C	85	X	1	77-112	717.17	1.305	
U1379	C	98	X	4	79-115	837.26	1.248	
U1379	C	99	X	2	118-150	844.18	1.288	
U1379	C	102	X	5	110-140	877.4	1.224	
U1379	C	103	X	2	34-60	881.24	1.251	

APPENDIX B

Table B1. Pore water magnesium isotope data

Leg/Expedition	Site	Hole	Core	Type	Section	Depth (mbsf)	δ^{26}Mg (‰)	δ^{26}Mg 2σ (‰)	δ^{25}Mg (‰)	δ^{25}Mg 2σ (‰)
170	1039	B	1	H	1	1.45	-0.86	0.04	-0.40	0.04
170	1039	B	4	H	5	28.40	-0.93	0.04	-0.45	0.04
170	1039	B	8	H	4	64.90	-1.00	0.04	-0.50	0.04
170	1039	B	12	X	3	101.35	-1.07	0.04	-0.55	0.04
170	1039	B	16	X	3	136.55	-1.00	0.04	-0.51	0.04
170	1039	B	21	X	5	187.55	-0.92	0.04	-0.46	0.04
170	1039	B	29	X	3	261.75	-0.94	0.04	-0.48	0.04
170	1039	B	37	X	5	341.70	-0.88	0.04	-0.47	0.04
170	1039	C	7	R	1	421.65	-0.77	0.04	-0.38	0.04
334	U1378	B	1	H	1	1.51	-0.81	0.06	-0.41	0.04
334	U1378	B	3	H	5	22.15	-0.68	0.06	-0.33	0.04
334	U1378	B	5	H	2	36.66	0.05	0.06	0.04	0.04
334	U1378	B	10	H	2	84.18	-0.38	0.06	-0.18	0.04
334	U1378	B	19	X	5	148.62	-0.23	0.06	-0.11	0.04
334	U1378	B	29	X	3	236.65	-0.39	0.06	-0.20	0.04
334	U1378	B	41	X	5	340.88	-0.99	0.06	-0.52	0.04
334	U1378	B	56	X	2	458.40	-1.12	0.06	-0.55	0.04
334	U1378	B	60	X	4	499.90	-0.96	0.06	-0.51	0.04
334	U1378	B	62	X	1	510.37	-1.05	0.05	-0.56	0.05
344	U1380	C	13	R	6	551.75	-1.29	0.05	-0.72	0.05
344	U1414	A	1	H	1	0.56	-0.92	0.05	-0.50	0.05
344	U1414	A	3	H	2	14.01	-0.78	0.05	-0.41	0.05
344	U1414	A	5	H	5	37.12	-0.83	0.05	-0.42	0.05
344	U1414	A	12	H	5	104.06	-0.82	0.05	-0.44	0.05
344	U1414	A	22	H	6	198.88	-0.55	0.05	-0.28	0.05
344	U1414	A	28	X	4	252.93	-0.09	0.05	-0.05	0.05
344	U1414	A	32	X	2	288.82	0.08	0.05	0.03	0.05
344	U1414	A	36	R	2	314.01	-0.07	0.05	-0.04	0.05
344	U1414	A	38	R	2	328.39	-0.14	0.05	-0.06	0.05
344	U1414	A	39	R	1	336.67	0.38	0.05	0.19	0.05
315	C0002	B	1	R	2	476.58	-0.75	0.05	-0.40	0.03
315	C0002	B	11	R	3	564.47	-0.92	0.05	-0.48	0.03
315	C0002	B	19	R	3	640.52	-0.92	0.05	-0.49	0.03
315	C0002	B	27	R	2	714.27	-1.27	0.05	-0.65	0.03
315	C0002	B	37	R	2	807.12	-1.21	0.05	-0.64	0.03
315	C0002	B	48	R	5	915.45	-1.36	0.05	-0.72	0.03
315	C0002	D	1	H	2	1.52	-0.78	0.05	-0.38	0.03
315	C0002	D	2	H	3	8.64	-0.65	0.05	-0.35	0.03
315	C0002	D	3	H	4	19.28	-0.41	0.05	-0.23	0.03
315	C0002	D	5	H	4	38.33	-0.35	0.05	-0.18	0.03
315	C0002	D	10	H	4	85.87	-0.21	0.05	-0.10	0.03
315	C0002	D	16	H	6	157.09	0.05	0.05	0.01	0.03
NGHP01	NGHP18	A	1	H	1	1.40	-0.83	0.05	-0.45	0.05
NGHP01	NGHP18	A	2	H	3	11.80	-0.84	0.05	-0.45	0.05
NGHP01	NGHP18	A	2	H	6	16.30	-0.83	0.05	-0.45	0.05
NGHP01	NGHP18	A	4	H	3	30.80	-0.75	0.05	-0.40	0.05
NGHP01	NGHP18	A	6	H	2	48.17	-0.53	0.05	-0.28	0.05
NGHP01	NGHP18	A	7	H	5	61.56	-0.44	0.05	-0.22	0.05
NGHP01	NGHP18	A	9	H	2	80.75	-0.48	0.05	-0.26	0.05
NGHP01	NGHP18	A	11	H	3	101.20	-0.50	0.05	-0.28	0.04
NGHP01	NGHP18	A	16	X	6	152.65	-0.60	0.05	-0.28	0.05

All δ^{26}Mg and δ^{25}Mg data are relative to the DSM3 standard. NGHP01 refers to the Indian National Gas Hydrate Program Expedition 01.

Table B2. Magnesium flux model results and site metadata

Leg/ Expedition	Site	Holes	Lat.	Lon.	Water Depth (m)	Mg flux (mmol m^{-2} y^{-1})	Mg flux 1σ	Concentration gradient (mM m^{-1})	# of concentration points used for gradient	R^2 of concentration gradient fit	Surface porosity	Bottom water [Mg] (mM)	Calculated sedimentation rate (m My^{-1})
4	27	A	15.857	-56.879	5251	1.40	0.32	-0.28	10	0.954	0.68	54.1	10.8
5	34		39.470	-127.276	4322	1.22	0.16	-0.10	7	0.982	0.78	53.9	20.5
7	62	A	1.870	141.938	2605	4.18	0.82	-0.81	4	0.997	0.69	53.8	22.7
11	102		30.732	-74.452	3426	2.11	0.22	-0.20	8	0.959	0.79	54.2	114.3
12	116	A	57.496	-15.924	1151	1.04	0.10	-0.07	7	0.894	0.71	54.5	27.7
14	137		25.926	-27.061	5361	0.92	0.29	-0.19	4	0.998	0.69	54.2	2.4
14	144	AB	9.454	-54.342	2957	0.44	0.18	-0.10	7	0.675	0.63	54.3	5.2
18	174	A	44.890	-126.352	2807	5.88	0.20	-0.14	8	0.888	0.88	53.8	179.5
18	178		56.956	-147.131	4218	3.83	0.23	-0.15	7	0.990	0.74	53.9	174.0
18	180		57.363	-147.856	4923	14.13	0.48	0.15	4	0.355	0.58	53.9	672.1
22	217		8.926	90.539	3010	1.11	0.15	-0.11	5	0.999	0.90	53.9	9.8
22	218		8.007	86.283	3749	2.24	0.28	-0.30	8	0.966	0.65	53.9	58.8
25	241		-2.371	44.680	4054	1.24	0.13	-0.12	7	0.955	0.81	53.9	27.4
25	242		-15.844	41.821	2275	1.16	0.07	-0.10	7	0.994	0.68	54.0	26.3
25	245	A	-31.534	52.302	4857	0.50	0.66	-0.08	6	0.414	0.81	53.9	1.8
25	248		-29.530	37.475	4994	0.68	0.04	-0.04	6	0.951	0.75	53.9	17.4
25	249		-29.950	36.077	2098	0.21	0.03	-0.03	10	0.988	0.63	54.0	5.3
31	296		29.340	133.525	2920	1.31	0.19	-0.13	6	0.839	0.73	53.8	26.3
31	297		30.873	134.165	4458	3.50	0.30	-0.29	7	0.993	0.76	53.9	58.6
33	315	A	4.171	-158.526	4152	1.41	6.63	-0.06	6	0.972	0.89	53.9	22.4
33	317	AB	-11.002	-162.263	2598	0.35	0.05	-0.02	6	0.874	0.71	53.8	9.9
35	322		-60.024	-79.425	5026	2.38	0.20	-0.14	7	0.919	0.73	53.9	43.8
35	323		-63.681	-97.995	5004	1.37	0.13	-0.06	6	0.934	0.78	53.9	24.5
36	328	B	-49.811	-36.659	5095	0.60	0.07	-0.10	8	0.967	0.79	53.8	1.4
38	336		63.351	-7.788	811	0.74	0.14	-0.15	9	0.991	0.63	54.2	7.9
38	345		69.837	-1.238	3195	0.61	0.08	-0.11	8	0.996	0.72	54.2	5.9
39	355		-15.710	-30.601	4901	0.72	0.09	-0.07	4	0.982	0.80	53.9	10.8
39	356		-28.287	-41.088	3175	0.40	0.07	-0.09	4	1.000	0.67	54.2	0.9
39	357		-30.004	-35.560	2086	0.33	0.04	-0.07	6	0.996	0.58	53.9	3.7
40	361		-35.066	15.449	4549	1.01	0.21	-0.17	5	0.990	0.78	53.9	4.4
40	362	A	-19.758	10.533	1325	1.49	0.13	-0.12	5	0.506	0.81	54.0	34.3
40	363		-19.646	9.047	2248	0.26	0.05	-0.06	8	0.811	0.58	54.2	5.4
43	386		31.187	-64.249	4782	1.19	0.33	-0.24	7	0.965	0.69	54.2	9.2
43	387		32.320	-67.667	5117	0.67	0.26	-0.14	5	0.994	0.70	54.2	3.5
44	391	ABC	28.227	-75.616	4974	1.25	0.15	-0.10	10	0.969	0.94	54.2	23.0
47	397		26.845	-15.180	2900	9.65	1.76	-1.79	7	0.915	0.70	54.3	55.4
48	403		56.139	-23.294	2301	0.59	0.10	-0.13	6	0.999	0.48	54.3	10.7
48	404		56.052	-23.249	2306	0.71	0.15	-0.09	6	0.930	0.66	54.3	29.3
48	405		55.336	-22.058	2958	0.47	0.08	-0.04	6	0.967	0.71	54.3	13.6
48	406		55.258	-22.090	2907	1.54	0.08	-0.11	7	0.998	0.77	54.3	40.3

Leg/ Expedition	Site	Holes	Lat.	Lon.	Water Depth (m)	Mg flux (mmol m^{-2} y^{-1})	Mg flux 1σ	Concentration gradient (mM m^{-1})	# of concentration points used for gradient	R^2 of concentration gradient fit	Surface porosity	Bottom water [Mg] (mM)	Calculated sedimentation rate (m My^{-1})
53	418	B	25.035	-68.057	5513	0.35	0.05	-0.04	6	0.804	0.86	54.1	2.7
56	436		39.933	145.558	5240	1.89	0.35	-0.20	6	0.943	0.77	53.9	31.8
57	440	AB	39.737	143.929	4509	4.25	0.11	0.06	7	0.653	0.69	53.9	148.4
58	443		29.328	137.441	4372	2.56	0.28	-0.16	9	0.958	0.80	53.9	40.2
58	445		25.523	133.208	3377	1.32	0.20	-0.20	5	0.996	0.72	53.8	23.1
58	446	A	24.701	132.775	4952	0.95	0.22	-0.17	10	0.985	0.76	53.9	3.9
60	453		17.907	143.683	4693	3.41	0.63	-0.21	9	0.957	0.87	53.9	75.3
60	459	AB	17.863	147.302	4121	1.97	0.23	-0.22	8	0.982	0.74	53.9	37.2
61	462		7.240	165.031	5178	0.33	0.12	-0.03	9	0.979	0.84	53.9	6.8
63	467		33.850	-120.758	2128	0.34	0.02	-0.14	5	0.980	0.13	53.8	71.4
64	474	A	22.961	-108.979	3023	7.62	1.86	-1.12	5	0.912	0.83	53.8	5.6
64	475	B	23.055	-109.059	2590	1.27	0.19	-0.17	9	0.933	0.79	53.8	7.5
64	476		23.041	-109.089	2403	4.10	0.53	-0.39	5	0.951	0.81	53.8	45.9
64	479		27.846	-111.625	747	2.81	0.84	0.11	4	0.296	0.90	53.6	191.7
64	481	A	27.253	-111.508	1998	6.72	1.11	0.60	6	0.740	0.86	53.8	438.9
65	483	B	22.883	-108.746	3070	0.19	0.04	-0.24	8	0.986	0.07	53.8	66.8
65	485	A	22.749	-107.904	2981	1.88	0.64	-0.20	8	0.893	0.53	53.8	162.4
67	495		12.496	-91.038	4140	4.36	1.18	-0.62	7	0.985	0.82	53.8	28.9
67	496		13.064	-90.795	2049	2.59	0.30	0.16	6	0.357	0.63	53.7	120.3
67	497		12.987	-90.828	2347	2.95	0.17	-0.12	6	0.866	0.66	53.9	88.3
71	511		-51.005	-46.972	2589	1.18	0.29	-0.18	10	0.962	0.81	53.9	4.2
72	515	B	-26.239	-36.503	4251	1.03	0.23	-0.22	9	0.995	0.61	53.8	18.7
72	516	AF	-30.276	-35.285	1313	0.46	0.05	-0.08	9	0.989	0.66	53.4	7.8
74	525	AB	-29.071	2.985	2467	0.40	0.05	-0.08	18	0.929	0.47	54.2	12.5
74	526	AC	-30.123	3.138	1054	0.20	0.10	-0.04	6	0.937	0.42	53.4	6.3
74	527		-28.042	1.763	4428	0.55	0.03	-0.08	11	0.981	0.51	54.2	13.6
74	528	A	-28.522	2.320	3808	0.34	0.02	-0.06	11	0.985	0.47	54.1	10.6
74	529		-28.931	2.768	3043	0.23	0.04	-0.08	7	0.990	0.47	54.2	4.4
75	530	AB	-19.188	9.386	4629	2.42	0.88	-0.59	13	0.925	0.64	54.2	25.7
76	533	A	31.260	-74.870	3191	7.23	0.69	-1.36	12	0.943	0.60	54.3	82.0
78	541		15.520	-58.728	4940	5.70	0.94	-1.23	7	0.916	0.63	54.1	53.6
79	545		33.664	-9.365	3142	1.05	0.17	-0.08	7	0.982	0.67	54.4	27.5
79	547	AB	33.781	-9.350	3938	0.74	0.14	-0.12	7	0.974	0.66	54.2	20.0
80	548	A	48.916	-12.164	1251	2.27	0.39	-0.42	8	0.971	0.61	54.9	26.6
80	549	A	49.088	-13.098	2514	0.27	0.05	-0.06	8	0.965	0.65	54.3	2.8
81	552	A	56.043	-23.231	2301	0.31	0.10	-0.05	8	0.949	0.56	54.3	17.6
81	555		56.562	-20.782	1659	3.91	5.03	-0.89	5	0.065	0.66	54.2	11.4
85	572	ABCD	1.435	-113.842	3893	-0.03	0.23	0.03	7	-0.114	0.81	53.9	14.4
85	573	AB	0.499	-133.310	4301	0.71	0.11	-0.06	15	0.888	0.79	53.9	14.7
85	574	ABC	4.209	-133.330	4561	0.37	0.05	-0.03	16	0.951	0.89	53.9	10.2
92	598		-19.005	-124.677	3699	0.29	0.28	-0.05	6	0.765	0.76	53.9	1.2
93	603	BC	35.925	-70.026	4636	6.50	0.88	-1.10	10	0.908	0.68	54.2	69.6
95	612		38.820	-72.774	1386	1.26	0.38	-0.29	5	0.963	0.58	54.4	10.2
95	613		38.771	-72.524	2309	1.98	0.25	-0.31	5	0.962	0.49	54.3	69.3

Leg/ Expedition	Site	Holes	Lat.	Lon.	Water Depth (m)	Mg flux (mmol m^{-2} y^{-1})	Mg flux 1σ	Concentration gradient (mM m^{-1})	# of concentration points used for gradient	R^2 of concentration gradient fit	Surface porosity	Bottom water [Mg] (mM)	Calculated sedimentation rate (m My^{-1})
96	615	A	25.222	-85.992	3268	6.40	0.12	0.04	16	0.213	0.75	54.3	289.2
96	617		26.699	-88.528	2467	0.99	0.24	0.25	5	0.806	0.71	54.3	106.3
96	619	A	27.194	-91.409	2259	1.19	0.40	0.23	5	-0.114	0.79	54.3	113.3
96	621		26.731	-88.496	2481	6.73	0.60	-0.56	4	0.748	0.72	54.3	119.3
96	622		26.690	-88.380	2491	7.94	1.93	-1.18	4	0.997	0.66	54.3	107.9
96	623		25.768	-86.231	3177	1.53	0.17	0.15	5	0.768	0.74	54.3	106.2
104	642	ABCD	67.217	2.933	1281	2.79	0.40	-0.30	7	0.991	0.74	54.2	45.9
104	644	A	66.683	4.583	1225	4.25	0.14	-0.17	7	0.655	0.62	54.2	98.9
105	645	BCDE	70.450	-64.650	2008	8.61	1.67	-2.01	11	0.987	0.60	53.6	129.5
105	646	AB	58.217	-48.367	3440	4.14	0.30	-0.30	12	0.986	0.78	54.2	82.2
105	647	A	53.333	-45.267	3864	2.76	0.45	-0.33	7	0.906	0.71	54.2	46.3
111	677	AB	1.200	-83.733	3473	0.59	0.14	0.03	16	0.238	0.91	53.9	45.6
113	689	AB	-64.517	3.100	2080	0.46	0.15	-0.05	6	0.908	0.86	53.8	7.2
113	690	ABC	-65.167	1.200	2914	0.02	0.14	0.01	4	0.730	0.72	53.8	3.2
113	693	AB	-70.833	-14.567	2359	1.06	0.17	-0.18	7	0.972	0.71	53.8	13.8
113	695	A	-62.383	-43.450	1300	0.31	0.10	-0.05	5	0.835	0.78	53.9	4.0
113	696	AB	-61.850	-42.933	650	1.23	0.37	-0.30	9	0.861	0.66	53.9	4.7
113	697	AB	-61.817	-40.292	3480	1.87	1.22	-0.20	7	0.924	0.72	53.8	38.4
114	699	A	-51.550	-30.683	3706	0.93	2.64	-0.10	7	0.945	0.89	53.8	11.0
114	701	ABC	-51.983	-23.217	4637	0.69	2.82	-0.05	6	0.981	0.86	53.8	22.9
114	703	A	-47.050	7.900	1796	0.58	2.18	-0.10	7	0.974	0.74	54.0	5.1
114	704	AB	-46.883	7.417	2532	0.53	2.46	0.04	4	0.571	0.84	54.0	59.8
115	708	A	-5.450	59.950	4107	0.72	1.15	-0.08	7	0.590	0.78	53.9	10.3
115	709	ABC	-3.917	60.550	3045	0.70	1.54	-0.08	6	0.496	0.71	53.9	12.4
115	710	A	-4.317	60.983	3822	1.26	3.19	-0.20	7	0.953	0.74	53.9	9.3
115	711	A	-2.750	61.167	4440	1.98	6.40	-0.32	10	0.700	0.78	53.9	4.1
116	717	AC	-0.933	81.383	4735	7.42	2.16	-0.93	5	0.998	0.76	53.9	189.2
116	718	ACE	-1.017	81.400	4730	17.35	5.14	-4.78	9	0.828	0.61	53.9	91.1
116	719	A	-0.967	81.400	4737	14.59	4.75	-1.93	6	0.967	0.81	53.9	146.5
117	721	AB	16.683	59.867	1937	2.91	0.31	-0.43	7	0.991	0.66	54.0	35.9
117	722	AB	16.617	59.800	2022	2.72	0.25	-0.44	7	0.995	0.65	54.0	33.6
117	723	ABC	18.050	57.611	805	6.08	2.98	-0.23	6	0.257	0.64	55.4	173.7
117	724	ABC	18.467	57.783	591	4.62	0.38	-0.46	10	0.947	0.61	55.0	80.5
117	726	A	17.817	57.367	329	1.65	1.49	-0.21	4	0.972	0.57	55.6	43.2
117	727	A	17.767	57.583	909	5.75	0.48	-0.48	4	0.955	0.67	55.2	97.7
117	728	ABE	17.683	57.833	1423	2.70	0.17	-0.31	14	0.931	0.65	54.5	39.2
117	730	A	17.733	57.700	1060	1.51	4.10	-0.26	4	0.975	0.66	54.8	14.4
117	731	ABC	16.467	59.700	2359	1.70	0.31	-0.28	14	0.995	0.73	54.0	43.7
119	737	AB	-50.233	73.033	564	1.33	0.12	-0.14	14	0.996	0.96	53.6	1.7
119	738	BC	-62.717	82.783	2253	0.25	1.79	-0.04	7	0.902	0.81	53.9	3.1
119	745	AB	-59.600	85.850	4083	2.29	0.26	-0.10	7	0.982	0.84	53.9	49.6
120	747	AC	-54.817	76.800	1696	0.55	1.00	-0.04	7	0.979	0.96	54.0	5.4
120	748	BC	-58.433	79.000	1290	1.88	0.53	-0.29	8	0.997	0.82	53.9	2.7
121	752	AB	-30.883	93.583	1086	0.58	0.20	-0.08	7	0.954	0.76	53.4	3.7

Leg/ Expedition	Site	Holes	Lat.	Lon.	Water Depth (m)	Mg flux (mmol m^{-2} y^{-1})	Mg flux 1σ	Concentration gradient (mM m^{-1})	# of concentration points used for gradient	R^2 of concentration gradient fit	Surface porosity	Bottom water [Mg] (mM)	Calculated sedimentation rate (m My^{-1})
121	756	ABCD	-27.350	87.600	1516	1.43	4.15	-0.38	14	0.449	0.61	53.8	3.4
121	757	ABC	-17.017	88.183	1649	1.11	0.18	-0.20	37	0.985	0.71	53.9	6.6
121	758	AB	5.383	90.367	2924	0.69	0.08	-0.06	18	0.966	0.77	54.0	13.2
124	767	BC	4.789	123.500	4905	6.61	9.02	-0.87	7	0.959	0.83	53.7	73.6
124	768	ABC	8.000	121.217	4384	2.28	0.27	-0.19	15	0.997	0.84	53.5	85.7
124	769	ABC	8.783	121.300	3644	5.15	1.41	-0.33	7	0.990	0.85	53.5	87.5
125	782	A	30.867	141.317	2962	1.03	6.29	-0.06	11	0.733	0.69	53.8	24.7
126	793	AB	31.100	140.883	2965	0.51	3.57	-0.01	6	0.859	0.70	53.8	91.6
127	794	AB	40.183	138.233	2808	4.28	3.33	-0.36	5	0.980	0.84	52.9	31.6
127	795	AB	43.983	138.967	3300	4.26	0.22	-0.20	15	0.966	0.97	52.9	61.0
127	797	ABC	38.617	134.533	2863	4.91	4.56	-0.45	12	0.961	0.82	52.9	47.3
128	798	ABC	37.033	134.800	901	19.04	8.82	-2.19	9	0.858	0.87	52.9	101.1
128	799	AB	39.217	133.867	2076	19.34	6.87	-1.91	7	0.995	0.89	52.9	116.7
131	808	ABC	32.350	134.950	4677	30.28	4.11	-3.25	8	0.990	0.73	53.9	702.4
133	814	A	-17.833	149.517	520	1.66	3.87	-0.24	4	0.110	0.67	53.9	19.2
133	815	A	-19.150	150.000	466	2.72	0.34	-0.43	14	0.992	0.64	54.6	14.4
133	816	A	-19.200	150.017	438	1.10	2.59	-0.19	9	0.961	0.60	54.6	7.1
133	817	AD	-18.150	149.763	1016	0.39	0.91	0.09	5	0.691	0.71	53.5	47.9
133	818	B	-18.067	150.050	747	1.21	1.73	0.04	5	0.794	0.67	53.5	62.6
133	819	A	-16.617	146.317	565	10.21	1.24	-1.22	7	0.988	0.70	53.4	129.7
133	821	A	-16.650	146.283	212	7.30	0.53	-0.60	12	0.973	0.61	53.4	242.9
133	822	A	-16.417	146.217	955	10.33	1.46	-1.93	6	0.998	0.63	54.1	76.3
133	823	ABC	-16.617	146.783	1638	4.77	0.56	-0.55	10	0.960	0.74	53.7	84.1
133	824	AB	-16.450	147.767	1001	1.76	1.88	0.00	9	0.263	0.67	53.5	72.5
134	830	ABC	-15.950	166.783	1015	8.39	2.76	-1.48	5	0.990	0.72	53.5	35.1
134	832	AB	-14.800	167.567	3089	8.62	2.63	-0.24	9	0.887	0.78	53.9	473.4
134	833	AB	-14.883	167.883	2629	7.18	9.16	-0.44	9	0.849	0.75	53.9	294.2
135	841	AB	-23.350	-175.300	4810	1.68	0.29	-0.20	8	0.987	0.80	53.9	33.8
138	846	AB	-3.100	-90.817	3296	1.53	2.68	-0.02	11	0.977	0.84	53.9	39.6
138	847	AB	0.200	-95.317	3335	0.93	3.14	0.02	6	0.614	0.85	53.9	32.2
138	849	AB	0.183	-110.517	3839	1.49	4.47	-0.15	4	0.765	0.83	53.9	27.9
138	850	AB	1.300	-110.517	3786	0.65	4.36	-0.02	11	0.974	0.85	53.9	20.7
138	852	ABC	5.300	-110.083	3860	1.29	5.51	-0.15	5	0.974	0.83	53.9	11.5
144	871	AC	5.550	172.350	1254	0.87	3.75	-0.07	13	-0.072	0.75	53.7	10.2
144	872	A	10.100	162.867	1083	0.12	0.20	0.01	5	0.301	0.78	53.7	5.2
145	881	AC	47.100	161.487	5531	2.78	5.54	-0.08	13	0.801	0.79	53.9	59.1
145	882	B	50.367	167.600	3244	2.23	10.61	-0.08	6	0.521	0.80	53.9	42.5
145	884	AB	51.450	168.333	3825	2.34	0.71	-0.04	14	0.926	0.86	53.9	50.9
145	887	A	54.367	-148.450	3634	2.69	10.41	-0.04	9	0.389	0.83	53.8	58.7
149	897	ACD	40.833	-12.471	5318	2.97	0.54	-0.51	9	0.922	0.61	54.2	73.0
149	898	AB	40.683	-12.117	5278	4.40	0.71	-0.57	9	0.967	0.69	54.2	85.5
149	900	A	40.683	-11.600	5037	0.66	0.05	-0.06	10	0.919	0.66	54.2	26.3
150	902	ACD	38.933	-72.767	812	6.47	1.23	-0.80	14	0.921	0.77	54.4	60.4
150	903	AC	38.933	-72.817	445	17.55	1.33	-1.32	13	0.975	0.54	54.3	566.6

Leg/ Expedition	Site	Holes	Lat.	Lon.	Water Depth (m)	Mg flux (mmol m^{-2} y^{-1})	Mg flux 1σ	Concentration gradient (mM m^{-1})	# of concentration points used for gradient	R^2 of concentration gradient fit	Surface porosity	Bottom water [Mg] (mM)	Calculated sedimentation rate (m My^{-1})
150	904	A	38.867	-72.767	1123	11.47	4.37	-1.72	5	0.992	0.71	54.4	96.5
150	905	A	38.617	-72.283	2698	4.13	0.85	-1.13	9	0.982	0.42	54.3	81.5
150	906	A	38.967	-72.767	913	6.70	3.59	-1.08	5	0.995	0.73	54.4	9.2
154	925	ABE	4.200	-43.483	3041	1.52	3.99	-0.23	15	0.904	0.73	54.2	28.9
154	926	AB	3.717	-42.911	3598	5.28	6.25	-0.97	5	0.995	0.73	54.2	27.7
154	927	A	5.467	-44.483	3315	3.41	3.63	-0.70	5	0.976	0.61	54.2	31.8
154	928	AB	5.450	-43.750	4012	1.31	2.01	-0.16	9	0.934	0.77	54.2	29.9
154	929	AE	5.983	-43.733	4356	1.33	3.02	-0.20	15	0.890	0.72	54.1	25.8
157	952	A	30.783	-24.517	5432	2.04	0.17	-0.17	15	0.971	0.84	54.2	31.1
157	953	AC	28.650	-15.150	3578	2.52	0.22	-0.26	19	0.968	0.62	54.2	64.9
157	954	AB	28.433	-15.533	3485	2.93	0.33	-0.11	8	0.930	0.75	54.2	73.5
159	959	ABD	3.633	-2.733	2091	1.01	0.13	-0.10	15	0.983	0.83	54.3	15.0
159	960	AC	3.583	-2.733	2039	2.32	0.43	-0.28	12	0.947	0.86	54.3	7.1
160	963	AD	37.033	13.183	470	15.23	2.92	-1.34	8	0.996	0.77	60.3	147.8
160	966	ABCDEF	33.800	32.700	926	6.45	13.99	-0.76	8	0.865	0.76	60.2	13.0
160	968	ABCDE	34.333	32.750	1963	0.11	0.24	0.11	9	0.963	0.64	60.2	36.6
161	974	AB	40.350	12.150	3455	5.69	4.38	-0.79	9	0.981	0.66	59.7	43.8
161	975	BC	38.900	4.517	2416	4.35	7.42	-0.59	11	0.909	0.62	59.8	71.0
161	976	BCD	36.200	-4.317	1108	14.10	2.43	-0.96	11	0.731	0.78	59.8	225.9
161	977	A	36.033	-1.950	1984	7.19	0.75	-0.61	10	0.998	0.73	59.8	152.3
161	979	A	35.717	-3.200	1062	9.40	1.41	-0.77	6	0.867	0.78	59.8	209.2
162	981	ABC	55.483	-14.650	2173	3.05	0.75	-0.38	8	0.982	0.70	54.3	56.8
162	982	AB	57.517	-15.867	1134	5.03	0.86	-0.77	9	0.998	0.74	54.5	20.6
162	983	A	60.400	-23.633	1984	4.43	0.25	-0.22	12	0.999	0.81	54.3	107.3
162	984	ABCD	61.433	-24.083	1648	4.41	1.41	-0.27	8	0.909	0.82	54.4	123.7
162	985	A	66.933	-6.450	2788	1.48	0.29	-0.25	12	0.997	0.70	54.2	26.0
162	987	ABCDE	70.500	-17.933	1672	4.32	1.21	-0.74	9	0.935	0.73	54.2	87.5
165	998	A	19.483	-82.933	3180	1.40	0.17	-0.15	12	0.984	0.76	54.3	19.8
165	999	AB	12.750	-78.733	2828	1.24	0.14	-0.13	21	0.995	0.76	54.3	25.8
165	1000	AB	16.550	-79.867	916	2.18	0.33	-0.33	10	0.986	0.69	54.2	24.3
165	1001	AB	15.750	-74.917	3260	0.85	1.60	-0.11	7	0.971	0.79	54.3	14.2
167	1012	A	32.283	-118.383	1772	4.64	2.40	-0.40	7	0.971	0.79	53.6	64.9
168	1023	A	47.917	-128.800	2593	33.80	11.09	-3.63	7	0.922	0.73	53.8	465.0
168	1024	AB	47.911	-128.750	2613	21.01	9.73	-1.66	12	0.926	0.87	53.8	299.4
168	1025	AB	47.883	-128.650	2609	23.37	6.98	-2.18	8	0.948	0.84	53.8	239.8
168	1026	AC	47.767	-127.761	2658	19.17	6.41	-2.67	7	0.948	0.68	53.8	274.3
168	1027	BC	47.750	-127.733	2657	11.38	0.63	0.14	9	0.525	0.85	53.8	448.0
168	1028	A	47.850	-128.500	2659	11.69	2.23	-0.78	7	0.952	0.76	53.8	223.2
168	1029	A	47.833	-128.383	2653	13.81	2.81	-0.96	7	0.975	0.86	53.8	227.1
168	1032	A	47.783	-128.117	2645	7.53	0.44	-0.18	12	0.987	0.54	53.8	250.1
170	1039	BC	9.633	-86.200	4352	2.68	1.28	-0.11	15	0.838	0.75	53.8	57.4
170	1040	ABC	9.667	-86.183	4178	1.90	0.37	-0.32	17	0.968	0.74	53.8	13.1
170	1041	ABC	9.733	-86.117	3306	8.47	0.74	-1.24	15	0.989	0.78	53.8	36.7

Leg/ Expedition	Site	Holes	Lat.	Lon.	Water Depth (m)	Mg flux (mmol m^{-2} y^{-1})	Mg flux 1σ	Concentration gradient (mM m^{-1})	# of concentration points used for gradient	R^2 of concentration gradient fit	Surface porosity	Bottom water [Mg] (mM)	Calculated sedimentation rate (m My^{-1})
170	1043	A	9.650	-86.183	4311	8.66	1.22	-0.80	8	0.950	0.78	53.8	145.0
171	1049	A	30.150	-76.117	2666	0.46	2.26	-0.03	5	0.757	0.71	54.2	22.1
172	1054	A	33.000	-76.283	1293	2.28	2.51	-0.20	13	0.864	0.76	54.8	36.2
172	1055	B	32.783	-76.283	1798	6.82	9.82	-0.49	8	0.863	0.81	54.4	106.3
172	1056	B	32.483	-76.333	2167	11.29	1.47	-1.62	7	0.988	0.72	54.3	98.9
172	1057	A	32.033	-76.083	2584	10.13	1.45	-1.47	5	0.998	0.72	54.3	104.1
172	1058	A	31.683	-75.433	2984	10.95	1.97	-1.36	5	0.994	0.74	54.3	113.6
172	1059	A	31.667	-75.417	2985	18.25	4.03	-1.99	8	0.974	0.80	54.3	181.4
172	1060	A	30.767	-74.467	3481	11.42	2.10	-0.99	10	0.980	0.80	54.2	249.6
172	1061	AE	29.980	-73.600	4040	9.74	1.44	-0.96	16	0.829	0.74	54.2	163.3
172	1062	AB	28.250	-74.408	4761	5.45	1.73	-0.50	20	0.946	0.81	54.2	98.9
172	1063	A	33.683	-57.617	4584	5.97	0.43	-0.37	23	0.991	0.81	54.2	173.6
175	1082	A	-21.100	11.817	1281	8.06	3.88	-0.42	16	0.822	0.80	53.8	137.9
175	1086	A	-31.550	15.667	783	1.12	0.80	-0.13	9	0.979	0.71	53.5	16.2
182	1127	B	-33.350	128.483	479	9.20	0.76	-0.54	11	0.921	0.64	53.9	269.2
182	1128	B	-34.383	127.583	3875	0.58	2.35	-0.10	12	0.786	0.65	53.9	8.8
182	1131	A	-33.333	128.483	332	4.60	1.46	0.00	4	-0.002	0.59	53.9	284.6
189	1171	ACD	-48.500	149.117	2148	3.08	5.41	-0.58	8	0.951	0.69	53.9	13.7
190	1173	A	32.250	135.022	4791	32.98	9.25	-4.45	6	0.976	0.78	53.9	233.7
190	1174	AB	32.350	134.950	4751	23.82	3.30	-3.46	9	0.980	0.70	53.9	640.6
190	1175	A	32.600	134.650	2998	15.81	2.73	-1.06	9	0.981	0.69	53.8	463.6
190	1176	A	32.583	134.667	3021	14.14	4.50	-2.04	12	0.931	0.74	53.8	250.9
190	1178	AB	32.733	134.483	1742	2.89	0.50	-0.66	8	0.971	0.66	53.7	21.1
199	1219	AB	7.800	-142.017	5063	8.15	1.19	-1.00	7	0.990	0.90	53.9	1.5
317	U1351	AB	-44.884	171.840	126	6.77	1.35	-1.12	8	0.971	0.57	53.4	153.9
320	U1336	B	7.701	-128.254	4292	2.15	1.78	-0.35	13	0.813	0.75	53.9	11.8
323	U1339	B	54.670	-169.982	1873	22.52	2.79	-2.71	40	0.387	0.70	53.7	234.8
323	U1340	AB	53.398	-179.520	1300	4.82	3.76	-0.05	5	0.359	0.84	53.3	143.5
323	U1341	AB	54.033	179.009	2145	7.87	2.30	-0.63	4	0.801	0.81	53.7	106.1
323	U1342	AC	54.828	176.917	824	5.87	7.75	-0.98	5	0.961	0.74	53.2	39.9
323	U1343	ABE	57.557	-175.817	1958	12.15	1.32	-0.87	32	0.596	0.73	53.7	274.1
323	U1344	AD	59.050	-179.203	3179	19.00	7.04	-1.36	5	0.982	0.80	53.8	366.4
323	U1345	A	60.153	-179.470	1014	21.18	7.76	-2.60	4	0.967	0.70	53.4	403.2
334	U1378	B	8.592	-84.077	524	13.95	2.85	-0.75	22	0.732	0.73	53.6	521.9
339	U1386	AB	36.828	-7.755	561	21.14	3.47	-2.91	6	0.982	0.62	55.9	276.7
339	U1387	A	36.805	-7.719	558	14.29	1.94	-1.74	6	0.969	0.64	55.5	235.3
339	U1390	A	36.319	-7.718	992	19.41	2.48	-1.38	4	1.000	0.69	55.7	458.8
339	U1391	AC	37.359	-9.411	1073	16.51	1.90	-1.54	7	0.992	0.70	56.4	311.5
340	U1394	B	16.641	-62.038	1114	7.31	2.18	-0.18	5	0.981	0.58	54.2	218.8
340	U1395	AB	16.493	-61.951	1201	7.06	1.50	-0.09	9	0.914	0.69	54.3	206.4
340	U1400	BC	14.539	-61.458	2743	7.02	4.60	-0.12	5	0.978	0.70	54.3	200.2
342	U1404	ABC	40.013	-51.810	4746	0.83	0.30	-0.13	13	0.968	0.74	54.2	5.2
342	U1408	A	41.438	-49.786	3022	0.60	3.87	-0.10	4	0.984	0.76	54.2	1.3
344	U1412	ABCD	8.487	-84.129	1956	11.74	4.97	-2.09	7	0.921	0.75	53.8	13.2

Leg/ Expedition	Site	Holes	Lat.	Lon.	Water Depth (m)	Mg flux (mmol m^{-2} y^{-1})	Mg flux 1σ	Concentration gradient (mM m^{-1})	# of concentration points used for gradient	R^2 of concentration gradient fit	Surface porosity	Bottom water [Mg] (mM)	Calculated sedimentation rate (m My^{-1})
344	U1414	A	8.504	-84.225	2459	5.52	10.25	-0.55	12	0.831	0.83	53.7	50.5
346	U1423	AB	41.699	139.083	1785	8.52	1.49	-0.92	8	0.993	0.82	52.9	76.6
346	U1426	AB	37.033	134.800	903	14.02	5.81	-1.80	17	0.459	0.83	52.9	84.3
346	U1428	AB	31.677	129.033	724	13.04	3.09	-0.16	17	0.753	0.78	53.3	409.6
346	U1429	A	31.617	128.998	732	12.71	0.74	-0.23	6	0.946	0.77	53.3	395.1
315	C0002	BD	33.332	136.667	1940	11.10	1.92	-1.73	11	0.989	0.77	53.7	107.0
316	C0004	CD	33.255	136.773	2632	6.92	1.30	-1.21	11	0.957	0.76	53.8	22.8
316	C0008	A	33.327	136.824	2782	12.94	2.18	-2.25	11	0.988	0.77	53.8	20.3
315	C0001	EFH	33.285	136.812	2197	4.21	0.49	-0.92	13	0.992	0.65	53.8	27.1
NGHP01	18	A	19.152	85.773	1374	5.92	2.45	-0.66	13	0.901	0.78	54.1	80.0

APPENDIX C

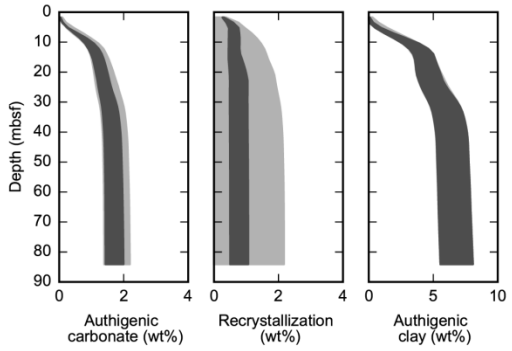

a) Site C0002

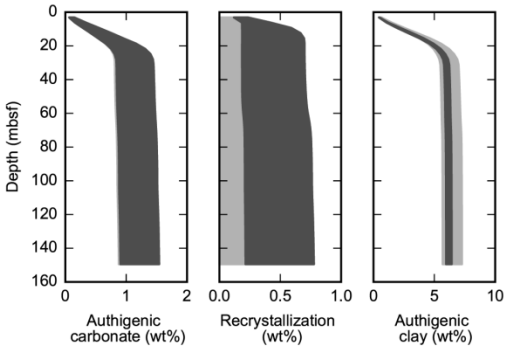

b) Site NGHP18

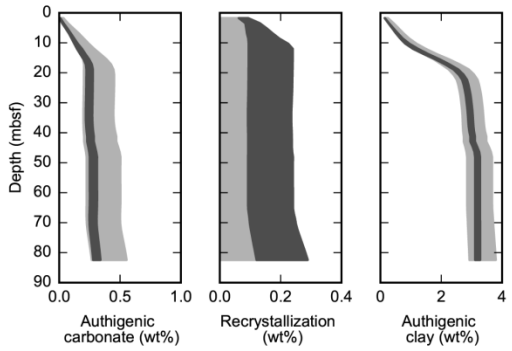

c) Site U1378

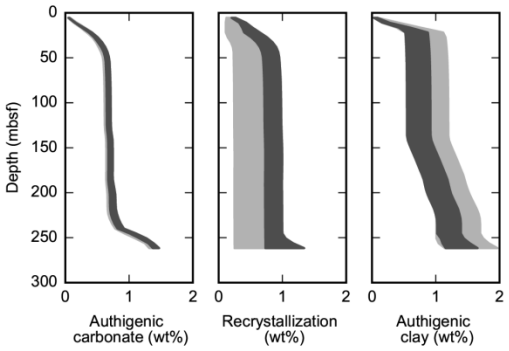

d) Site 1012

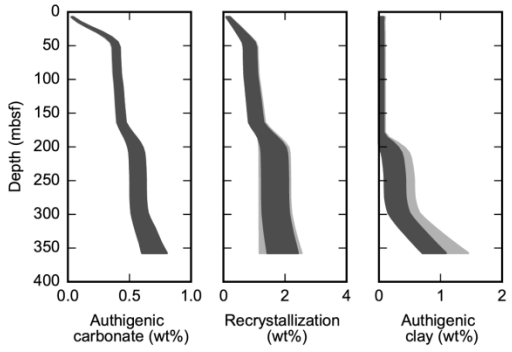

e) Site 1082

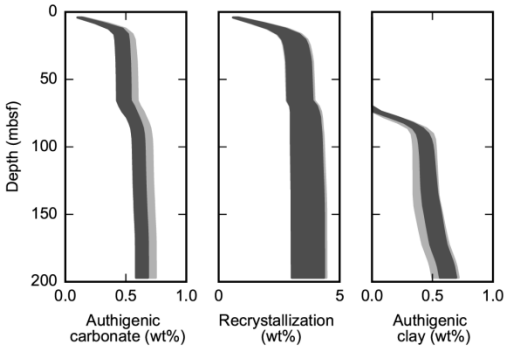

f) Site 1086

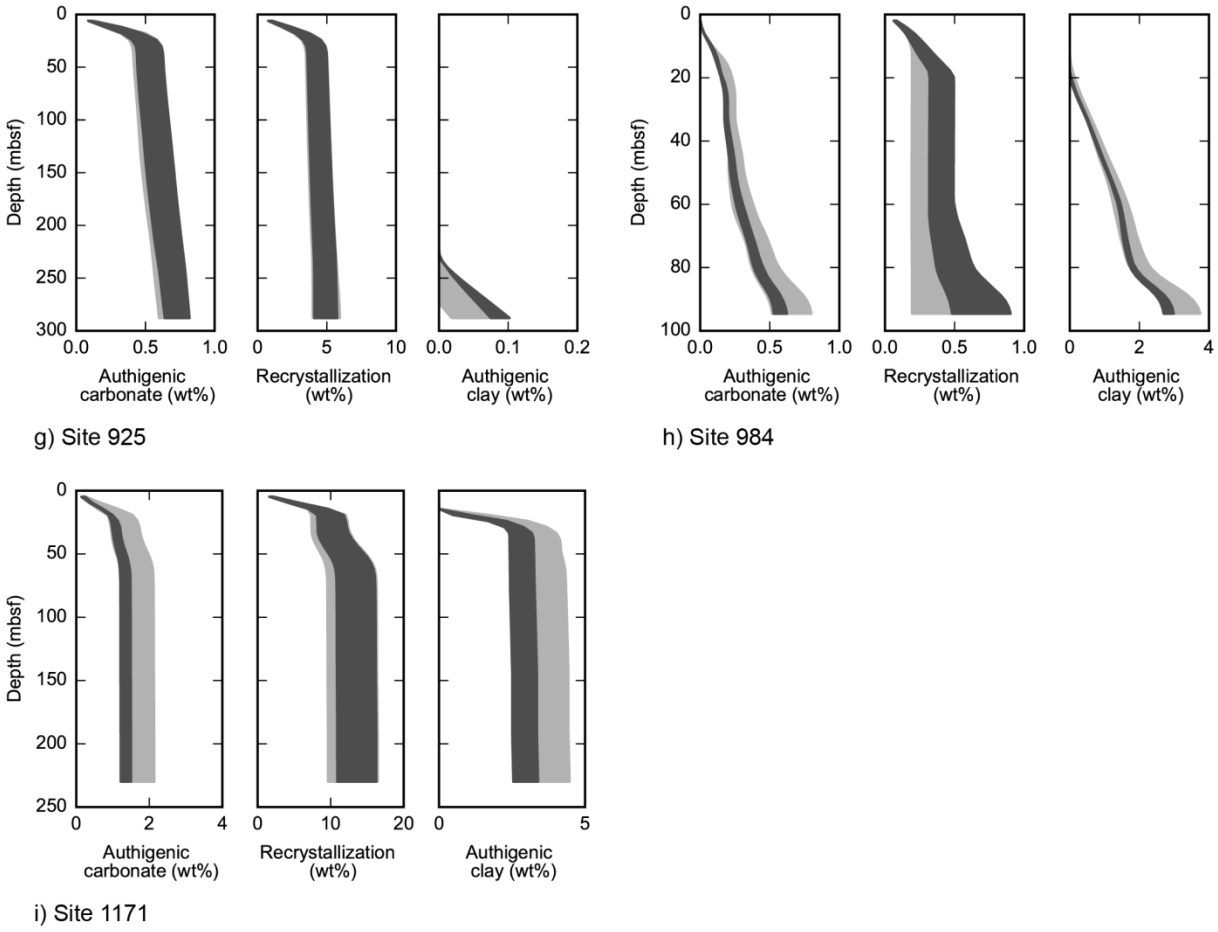

Figure C1. Total amounts of primary carbonate, recrystallized carbonate, and authigenic clay at all sites (subfigures a-i). The dark shaded region represents the range corresponding to the four best-fitting combinations of reaction stoichiometries and fractionation factors, and light gray region represents the full range of all 16 possible combinations. Units are in weight percent of dry bulk sediment.

Table C1. Model parameters

Parameter	Value
Reaction stoichiometries (Mg:Ca)	
Authigenic carbonate precipitation distribution coefficient $(Mg:Ca)_{solid}/(Mg^{2+}/Ca^{2+})_{porewater}$	0.015 to 0.020
Clay formation	-0.5 to -2
Reaction Mg isotope fractionation factors	
Authigenic carbonate precipitation	0.9972 to 0.9976
Clay formation	1.0005 to 1.0015
Cation exchange capacities (meq/kg)	
Smectite	840
Illite	160
Chlorite	50
Kaolinite	50
Opal	160
Cation exchange parameters	
α_{Mg} (mM)	54
β_{Mg}	1.5
$K_{Mg:NH4}$ smectite	0.31
$K_{Mg:NH4}$ illite	0.14
$K_{Mg:NH4}$ chlorite	0.14
$K_{Mg:NH4}$ kaolinite	0.14
$K_{Mg:NH4}$ opal	0.15
α_{Ca} (mM)	42
β_{Ca}	1.0
$K_{Ca:NH4}$ smectite	0.47
$K_{Ca:NH4}$ illite	0.21
$K_{Ca:NH4}$ chlorite	0.23
$K_{Ca:NH4}$ kaolinite	0.23
$K_{Ca:NH4}$ opal	0.24

Table C2. Site parameters

Site	925	984	1012	1082	1086	1171	U1378	C0002	NGHP18
Clay wt%	40	90	55	60	20	10	80	80	95
Opal wt%	0	0	0	0	0	0	0	0	5
Smectite (wt% of clay fraction)	40	30	35	15	15	80	50	25	20
Illite (wt% of clay fraction)	45	50	30	65	65	15	20	40	55
Chlorite (wt% of clay fraction)	5	15	30	5	5	0	20	25	15
Kaolinite (wt% of clay fraction)	30	5	5	15	15	5	10	10	10
Bottom water temperature (°C)	2.5	2.7	3.0	3.5	3.4	3.1	12.3	2.0	5.4
Geothermal gradient (°C/km)	50	105	82	51	52	62	51	40	50
Porosity cutoff depth (mbsf)	425	None	240	300	100	250	None	945	95
Sulfate-methane transition depth (mbsf)	N/A	120	19	25	180	320	13	9	21

VITA

Richard David Berg

EDUCATION

Ph.D. Oceanography, December 2018
University of Washington, Seattle, WA
Advised by Dr. Evan A. Solomon
Dissertation title: Quantifying the deep: The importance of diagenetic reactions to marine geochemical cycle

M.S. Oceanography, December, 2013
University of Washington, Seattle, WA
Advised by Dr. Evan A. Solomon

B.S./M.S. in Earth Sciences (Contiguous), March 2008
University of California - San Diego, La Jolla, CA
Advised by Dr. Miriam Kastner
Thesis title: Diffusional Methane Consumption in Continental Margin Sediments and Depositional Constraints on Formation Factor Estimates.

EMPLOYMENT

Environmental Geologist, Windward Environmental LLC, Seattle, WA, 2008 – 2011

Research Assistant, Dr. Miriam Kastner, Scripps Institution of Oceanography, La Jolla, CA, 2005 – 2007

FELLOWSHIPS AND AWARDS

Schlanger Ocean Drilling Fellowship, USSSP/IODP, 2016 – 2017

Campbell Donaldson Scholarship, University of Washington, 2013

IODP Post-Expedition Award, Integrated Ocean Drilling Program, 2013

Claire L. and Evelyn S. Egtvedt Fellowship, University of Washington, 2011

GSFEI Top Scholar Award, University of Washington, 2011

PEER REVIEWED PUBLICATIONS

R.D. Berg and E.A. Solomon, 2016. Geochemical constraints on the distribution and rates of debromination in the deep subseafloor biosphere. Geochimica et Cosmochimica Acta, doi:10.1016/j.gca.2015.11.003.

MANUSCRIPTS IN PREPARATION

R.D. Berg, E.A. Solomon, and F.Z.Teng, 2018. The role of marine sediments in the modern oceanic magnesium cycle.

R.D. Berg, E.A. Solomon, 2018. Formation rates of magnesium-bearing carbonates and clays in marine sediments.

PRESENTATIONS

CONFERENCE/MEETING PARTICIPATION

IODP Ocean Drilling Advisory Committee Meeting, American Museum of Natural History, NYC, August, 2017 (Talk).

Goldschmidt Conference, Paris, France, August, 2017 (Poster).

American Geophysical Union Fall Meeting, San Francisco, California, USA, December, 2016 (Poster).

IODP Expedition 344 post-cruise meeting, Shanghai, China, June, 2015 (Talk).

IODP Expedition 344 post-cruise meeting, Shanghai, China, June, 2015 (Poster).

American Geophysical Union Fall Meeting, San Francisco, California, USA, December, 2014 (Poster).

American Geophysical Union Fall Meeting, San Francisco, California, USA, December, 2013 (Talk).

Gordon Research Conference on Natural Gas Hydrate Systems, Galveston , TX, USA, March, 2013 (Poster).

Scripps Institution of Oceanography Public Open House, La Jolla, California, USA, October, 2007 (Poster).

Departmental Talks

University of Washington Marine Geology and Geophysics Seminar, University of Washington, Seattle, WA, April, 2017 (Talk).

University of Washington Marine Geology and Geophysics Seminar, University of Washington, Seattle, WA, December, 2013 (Talk).

University of Washington Marine Geology and Geophysics Seminar, University of Washington, Seattle, WA, October, 2012 (Talk).

TEACHING

Teaching Assistantships

OCEAN 102e – The Changing Oceans, Dr. M. Nuwer, Winter, 2018

OCEAN 310 – Marine Geology and Geochemistry, Prof. E. Solomon, Fall 2016, 2017

OCEAN 540 – Marine Geology and Geophysics, Prof. E. Solomon, Winter, 2016

OCEAN 201 – Intro. to Oceanography Lab, Profs. E. Solomon, A. Gagnon, Spring, 2015

OCEAN 200 – Intro. to Oceanography, Prof. P. Quay, Spring, 2014

OCEAN 121 – Deep Sea Exploration, Prof. D. Kelley, Winter, 2013

Guest Lectures

OCEAN 310 – Marine Geology and Geochemistry, Prof. E. Solomon
- Marine geochemical cycles, Oct. 25, 2017
- Hydrothermal circulation, Oct.23, 2017
- Ocean floor morphology, Sept. 30, 2016

OCEAN 411 – Seagoing Research & Discovery, Profs. D. Kelley & J. Delaney
- Gas hydrates and fluids in continental margins, Sept. 9, 2014 and Jul. 17, 2015

OCEAN 201 – Intro. to Oceanography Lab, Profs. E. Solomon & A. Gagnon
- Waves and beaches, May 29, 2015

OCEAN 540 – Marine Geology and Geophysics, Prof. E. Solomon
- Long-term climate, March 12, 2013

SIGNIFICANT OCEANOGRAPHIC EXPEDITIONS

R/V Thomas G. Thompson, July 4 – 20, 2015
VISIONS'15, Leg 1, OOI Cabled Array, Hydrate Ridge and Axial Seamount

R/V Thomas G. Thompson, October 10 – 19, 2014
Hydrate dissociation and methane plumes along the Cascadia margin

R/V Thomas G. Thompson, August 25 – September 11, 2014
VISIONS '14, Leg 4, OOI Regional Scale Nodes, Hydrate Ridge

R/V Atlantis II, July 29 – August 26, 2013
Fluid and heat flow survey of the Cascadia Subduction Zone on the WA Margin

R/V Thomas G. Thompson, July 8 – 18, 2013
VISIONS '13, Leg 2, OOI Regional Scale Nodes, Hydrate Ridge and Axial Seamount

JOIDES Resolution, October 23 – December 11, 2012
IODP Expedition 344, Costa Rica Seismogenesis Project, Program A Stage 2

PROFESSIONAL AND COMMUNITY SERVICE

Graduate Program Committee Member, UW School of Oceanography. Committee to reevaluate and redesign UW Oceanography graduate curriculum, 2017 – 2018.

Instructor for the Ocean Inquiry Project, hands-on oceanography and environmental education for public groups of all ages and undergraduate REU students aboard small vessels on Puget Sound, 2014 – 2017.

Data archivist for DataRescue program at UW Libraries as part of the national DataRefuge effort, 2017.

Reviewer for Proceedings of the IODP, 2016.

Event Supervisor for Dynamic Planet events of Washington State Science Olympiads for middle school and high school students, 2015 – 2016.

Remote guest speaker for Warm Springs Elementary School 6th grade science classes in preparation for students' upcoming science camp participation, 2015.